2021

The Characterization Of Visual Evoked Feedforward-Feedback Travelling Waves In Mice During Waking And Anesthetized States

Adeeti Aggarwal
University of Pennsylvania

The Characterization Of Visual Evoked Feedforward-Feedback Travelling Waves In Mice During Waking And Anesthetized States

Abstract

A cardinal feature of consciousness is the maintenance of a stable perceptual world. To accomplish this, sensory information must be faithfully relayed and integrated within the brain. General anesthetic agents reliably and reversibly produce states of unconsciousness. However, despite their ubiquitous use in medicine and science, the mechanisms by which anesthetics induce loss of consciousness remains unknown. Over the past 170 years, researchers have searched for the universal targets that anesthetic agents use to ablate perception (Alkire et al., 2008; Kelz and Mashour, 2019). However, there is not yet a common structural motif, receptor target, or sleep/arousal circuit that all known anesthetics interact with (Alkire et al., 2008; Kelz and Mashour, 2019). It was once postulated that anesthetics may ablate perception by disconnecting the cortex from incoming thalamic signals (Alkire et al., 2000; Alkire and Miller, 2005; White and Alkire, 2003); yet under anesthesia, neurons within primary cortical areas are still able to encode features of sensory stimuli, thereby suggesting sensory information is effectively relayed to the cortex (Hubel and Wiesel, 1962). Thus, it has been recently theorized that anesthetics may hinder the ability for sensory responses to faithfully participate in hierarchal, feedback and integrative circuits at a network level (Lee et al., 2009; Mashour, 2006, 2014). In this dissertation, I investigate this theory by analyzing the spatiotemporal features of visual evoked oscillations over multiple hierarchical cortical areas in awake and anesthetized mice presented with simple visual stimuli and answering a series of motivating questions. Are there consistent neurophysiological substrates to coordinate visual evoked activity across the many cortical regions involved in visual processing in awake mice, who have the ability to perceive stimuli? If so, what is the spatiotemporal structure of this activity pattern, and does it coordinate neural firing in disparate cortical areas? Can we identify patterns that may be related to hierarchical visual processing vs feedback signaling? How do mechanistically distinct anesthetic agents disrupt visual evoked patterns seen in the awake brain? Are there agent specific effects? And finally, can we identify a common mechanism by which all tested anesthetic agents breakdown visual evoked activity? While my research does not test perception per se, findings herein will provide the neurophysiological basis for the integration of visual-evoked activity across cortices during wakefulness, and the breakdown of this coordinated pattern of activity during anesthetic induced states of unconsciousness.

Degree Type

Dissertation

Degree Name

Doctor of Philosophy (PhD)

Graduate Group

Neuroscience

First Advisor

Max B. Kelz

Second Advisor

Alexander Proekt

Subject Categories

Neuroscience and Neurobiology

THE CHARACTERIZATION OF VISUAL EVOKED FEEDFORWARD-FEEDBACK TRAVELLING

WAVES IN MICE DURING WAKING AND ANESTHETIZED STATES

Adeeti Aggarwal

A DISSERTATION

in

Neuroscience

Presented to the Faculties of the University of Pennsylvania

in

Partial Fulfillment of the Requirements for the

Degree of Doctor of Philosophy

2021

Supervisor of Dissertation   Co-Supervisor of Dissertation

_____   _____

Max B. Kelz, MD. PhD.   Alex Proekt MD. PhD

Professor of Anesthesiology & Critical Care   Professor of Anesthesiology & Critical Care

Graduate Group Chairperson

_____

Joshua I. Gold, PhD

Professor of Neuroscience

Dissertation Committee

Yale Cohen, PhD, Professor of Neuroscience

Maria Geffen, PhD, Professor of Neuroscience

Joshua I. Gold, PhD, Professor of Neuroscience

George Mashour, MD, PhD, Professor of Anesthesiology, University of Michigan

THE CHARACTERIZATION OF VISUAL EVOKED FEEDFORWARD-FEEDBACK TRAVELLING

WAVES IN MICE DURING WAKING AND ANESTHETIZED STATES

COPYRIGHT

2021

Adeeti Aggarwal

To my family, Amol, Sangeeta, and Alok Aggarwal for teaching me how to value grit and creativity

ACKNOWLEDGMENT

To my friends that became my Philly family – Sydney, Jeni, Ursula, Ruthie, Lyles, Brenna, Alice, Michelle, Serena, Nirali, and Rahul, thank you for your friendship and support. Celebrating and commiserating with you got me through the good times and bad.

To my brother, Amol, thank you for spending hours teaching me mathematical concepts, many of which I have used throughout my PhD in analyzing my data. Thank you also for listening to my frustrations and providing sympathy.

To my parents, thank you for nurturing my love of science as a kid and continuing to support and encourage me to pursue it to this day.

ABSTRACT

THE CHARACTERIZATION OF VISUAL EVOKED FEEDFORWARD-FEEDBACK TRAVELLING

WAVES IN MICE DURING WAKING AND ANESTHETIZED STATES

Adeeti Aggarwal

Max B. Kelz

Alex Proekt

A cardinal feature of consciousness is the maintenance of a stable perceptual world. To accomplish this, sensory information must be faithfully relayed and integrated within the brain. General anesthetic agents reliably and reversibly produce states of unconsciousness. However, despite their ubiquitous use in medicine and science, the mechanisms by which anesthetics induce loss of consciousness remains unknown. Over the past 170 years, researchers have searched for the universal targets that anesthetic agents use to ablate perception (Alkire et al., 2008; Kelz and Mashour, 2019). However, there is not yet a common structural motif, receptor target, or sleep/arousal circuit that all known anesthetics interact with (Alkire et al., 2008; Kelz and Mashour, 2019). It was once postulated that anesthetics may ablate perception by disconnecting the cortex from incoming thalamic signals (Alkire et al., 2000; Alkire and Miller, 2005; White and Alkire, 2003); yet under anesthesia, neurons within primary cortical areas are still able to encode features of sensory stimuli, thereby suggesting sensory information is effectively relayed to the cortex (Hubel and Wiesel, 1962). Thus, it has been recently theorized that anesthetics may hinder the ability for sensory responses to faithfully participate in hierarchal, feedback and integrative circuits at a network level (Lee et al., 2009; Mashour, 2006, 2014).

In this dissertation, I investigate this theory by analyzing the spatiotemporal features of visual evoked oscillations over multiple hierarchical cortical areas in awake and anesthetized mice presented with simple visual stimuli and answering a series of motivating questions. Are there consistent neurophysiological substrates to coordinate visual evoked activity across the many cortical regions involved in visual processing in awake mice, who have the ability to

perceive stimuli? If so, what is the spatiotemporal structure of this activity pattern, and does it coordinate neural firing in disparate cortical areas? Can we identify patterns that may be related to hierarchical visual processing vs feedback signaling? How do mechanistically distinct anesthetic agents disrupt visual evoked patterns seen in the awake brain? Are there agent specific effects? And finally, can we identify a common mechanism by which all tested anesthetic agents breakdown visual evoked activity?

While my research does not test perception per se, findings herein will provide the neurophysiological basis for the integration of visual-evoked activity across cortices during wakefulness, and the breakdown of this coordinated pattern of activity during anesthetic induced states of unconsciousness.

TABLE OF CONTENTS

LIST OF TABLES

LIST OF ILLUSTRATIONS

CHAPTER 1 - General Introduction

Since its discovery in 1846, anesthesia has monumentally changed medical practice by rendering patients unconscious during lifesaving surgical procedures (Robinson and Toledo, 2012). Anesthetic agents have also been indispensable for basic research in neuroscience. Much of what is known about the basic physiology of sensory systems has been learned from work on anesthetized animals (Hubel and Wiesel, 1962). The universal principles that underlie suppression of sensory perception by mechanistically distinct anesthetics remain largely unknown. The major motivation of the work presented in this thesis is to identify universal features of brain dynamics that are reliably associated with and perhaps responsible for disruption of sensory perception.

General anesthetics heterogeneity

Molecular targets

Anesthetic agents comprise of family of compounds that are structurally heterogeneous, yet all produce a dose dependent loss of consciousness. Each class of anesthetics interacts with a preferred set of receptors, but tend to bind with low affinities (Alkire and Miller, 2005; Eckenhoff, 2002a; Hemmings et al., 2019; Kelz and Mashour, 2019) (Figure 1.1). For example, most volatile and intravenous anesthetics, including isoflurane and propofol, potentiate GABAA receptor binding, thereby hyperpolarizing the cell membrane and inhibiting neuronal excitation (Garcia et al., 2010; Hemmings et al., 2019; Jurd et al., 2003; Kelz and Mashour, 2019; Tang and Eckenhoff, 2018; Wang, 2009; Yip et al., 2013). Volatile anesthetics have also been shown to agonize glycine receptors as well as and inhibit SNARE complex formation necessary for

neurotransmitter release (Hao et al., 2020; Herring et al., 2009; Kelz and Mashour, 2019; Lobo and Harris, 2005; Nagele et al., 2005). Dissociative anesthetics, such as ketamine, on the other hand, antagonize NMDA receptors and stabilize the open conformation of HCN channels (Chen et al., 2009; Yamamura et al., 1990; Zhou et al., 2018). While the majority of these effects decrease excitation, identifying a unifying circuit mechanism based on molecular binding has been difficult given that these receptors are differentially distributed within the nervous system (Garcia et al., 2010; Hemmings et al., 2019; Jurd et al., 2003; Kelz and Mashour, 2019; Tang and Eckenhoff, 2018; Wang, 2009; Yip et al., 2013).

Anesthetics activity within sleep wake centers

An attractive circuit mechanism explaining anesthetic induced loss of conscious is through hijacking endogenous sleep-wake circuitry (Kelz and Mashour, 2019; Lu et al., 2008a; Mashour, 2014; Mashour and Hudetz, 2017; Scharf and Kelz, 2013). Many of the GABA-ergic anesthetic agents, including isoflurane and propofol, depress activity of arousal centers such as the locus coeruleus (Aston-Jones and Cohen, 2005; Leung et al., 2014; Vazey and Aston-Jones, 2014) and activate sleep promoting centers including the ventrolateral preoptic (VLPO) (Li et al., 2009; Moore et al., 2012; Nelson et al., 2002), thereby tilting the biological scale into a lower level of arousal. However, ketamine does not tend to activate VLPO neurons, and instead tends to active arousal centers (Lu et al., 2008b).

Anesthetics induced EEG states

While significant strides have been made in understanding the molecular and circuit mechanisms underlying general anesthesia, comprehending the network effects of anesthesia has proven to be more difficult. Anesthetic agents alter the spectral state of the brain by distorting

thalamo-cortical networks and altering excitation-inhibition balances within neural networks (Brown et al., 2012; Douglas and Martin, 2004; Scharf and Kelz, 2013; Steriade and Timofeev, 2003). However, the induced spontaneous brain state is similarly heterogeneous. For instance, including propofol induce a predominant slow wave, large amplitude EEG profile with sleep spindles, thereby mirroring slow-wave sleep (Ching et al., 2010; Purdon et al., 2013). Isoflurane produces distinct UP-states and DOWN-states in the EEG that also resembles slow waves, and promotes quick transitions in and out of burst suppression (Ferron et al., 2009a; Hudson et al., 2014; Sonner et al., 2007). However, not all anesthetics produce canonical sleep-like electrophysiological patterns. Ketamine, an NMDA antagonist, induces an "awake-like" EEG with pronounced gamma oscillations (Blain-Moraes et al., 2014; Maksimow et al., 2006).

Moreover, high doses of isoflurane and propofol reliably elicit burst suppression, a pattern in which the EEG oscillates between long (>500ms) of quiescent activity and large bursts of higher frequency activity (Ferron et al., 2009a; Kroeger and Amzica, 2007).

Thalamic switch hypothesis

Some hypothesized that anesthetics disrupt perception through the "thalamic switch". The major thrust of this hypothesis is that anesthetics inhibit the thalamic relay of sensory information to primary sensory cortices (Alkire et al., 2000; Alkire and Miller, 2005). In support of this theory, nearly all anesthetics metabolically depress the thalamus (Alkire et al., 2000; Alkire and Miller, 2005). However, even under anesthesia, sensory evoked potentials can be readily recorded from primary cortical areas, and in some cases, can even be enhanced (Ferezou et al., 2006; Hubel and Wiesel, 1962; Hudetz and Imas, 2007; Imas et al., 2005b; Raz et al., 2014). Furthermore, classic work on physiology of the primary visual cortex (V1) showed that under anesthesia individual neurons reliably fire in response to sensory stimuli and that this firing encodes features of the visual stimuli (Hubel and Wiesel, 1962). These observations are difficult to reconcile with the major tenets of the "thalamic switch" hypothesis.

Focus has thus turned towards understanding the mechanisms underlying anesthetics effects on the hierarchical processing and integration of evoked activity after sensory information reaches primary cortical areas (Mashour, 2006, 2014). To explore the potential mechanisms by which anesthetics might impair perception through their actions on higher order signaling events, we generated an experimental set up in which we can record high density neurophysiological data from almost an entire cortical hemisphere of awake and anesthetized mice receiving simple visual stimuli. Thus, we can probe how visual evoked potentials are processed in a coherent fashion across many hierarchical cortical areas during the waking state. Moreover, with this design, we can localize points at which distinct anesthetics critically disrupt sensory processing.

<u>Hierarchal visual processing in mice</u>

In the retino-geniculo-cortical pathway, visual information enters through photoreceptors with the retina, synapse with retinal ganglion cells, then relays within the dorsal lateral geniculate nucleus of the thalamus before reaching layer 4 of the primary visual cortex (V1) (Busse, 2018; Douglas and Martin, 2004, 2007; The Thalamus, 1985). Within each cortical column, signals from layer 4 are relayed to layers 2/3 and then to layers 5 and 6 (Douglas and Martin, 2004, 2007; Jones, 1985) (Figure 1.2). From here, signals can spread to different cortical areas via a variety of circuits. Lateral projections in layers 2/3 and layer 5 allow for horizontal propagation via cortico-cortical signaling (Douglas and Martin, 2004; Wester and Contreras, 2012). Layer 6 neurons project to higher order cortices and matrix thalamic nuclei (Douglas and Martin, 2004; Jones, 1985). Higher order and matrix thalamic nuclei in turn, send projections preferentially to layers 1 and 6, thereby forming cortico-thalamo-cortical loops (Douglas and Martin, 2004; Jones, 1985). Moreover, cells in layer 5 also project to subcortical structures such as the superior colliculus and the brain stem, thus forming the basis for cortico-tectal or cortico-bulblar circuitry (Brumberg et al., 2003; Douglas and Martin, 2004; Jones, 1985).

Within V1, neurons are organized retinotopically and generally tuned to a broad range of spatiotemporal frequencies present in visual stimuli (Busse, 2018; Niell and Stryker, 2008). Visual information is then processed in a hierarchal, feedforward fashion in the secondary visual areas, comprised of a set extrastriate regions that surround V1. These areas are also retinotopically organized but are more sensitive to specific stimulus parameters and tend to display more selective connectivity to higher order areas (Andermann et al., 2011a; Busse, 2018; Garrett et al., 2014; Marshel et al., 2011a; Wang et al., 2011). For example, neurons in area Anterolateral (AL) prefer stimuli with higher temporal and lower spatial frequencies, and is part of the presumed dorsal-stream pathway due to its connectivity with the dorsal cortex, including the Posterior Parietal Area (PPA) (Andermann et al., 2011b; Busse, 2018; Garrett et al., 2014; Marshel et al., 2011b; Wang et al., 2011).

Feedforward Feedback processing of sensory stimuli

Feedforward signaling is thought to mediate the hierarchical processing of sensory features that are extracted in primary areas into abstract representations that are synthesized in higher order cortical areas (Felleman and Van Essen, 1991; Markov et al., 2014). Conversely, feedback processing relays attention, prediction, and context from higher order cortical areas back to primary sensory areas (Felleman and Van Essen, 1991; Markov et al., 2014). Thus, at each level of the cortical hierarchy, feedforward and feedback streams interact with one another in an organized manner to coordinate neural activity involved in processing stimuli.

The Posterior Parietal Area (PPA) is a hub for feedforward-feedback interactions in mice

The Posterior Parietal Area (PPA) sends and receives projections from primary and secondary sensory areas from many modalities, as well as higher order areas, and therefore is an important structure in relaying feedforward-feedback signals (Hovde et al., 2019; Zingg et al.,

2014). In mice, the PPA is located between the visual and somatosensory cortices (Franklin, Keith, B. and Paxinos, 2007; Hovde et al., 2019; Reference Atlas :: Allen Brain Atlas: Mouse Brain). Specifically in visual processing, the PPA is hypothesized to be a member of the dorsal stream network, in which visual information relays from V1 to secondary visual areas, to PPA in a feedforward fashion to form visuo-spatial perception (Hovde et al., 2019; Lyamzin and Benucci, 2019; Wang et al., 2011). The PPA also receives feedback self-motion cues from the medial entorhinal cortex, which can be integrated to picture the "self" in relation to the environment and thus may be related to how the PPA is important for visual goal directed behavior (Hovde et al., 2019; Wang et al., 2011). While much work had been conducted in characterizing the structural connectivity of PPA, and recently, correlating PPA activity with task behavior, a rigorous neurophysiological mapping of visual responses within the PPA has not been conducted.

Visual feedforward and feedback signals are conveyed through neural oscillations in primates

In the primate visual system, ample evidence suggests that oscillations of subthreshold neural activity relay feedforward and feedback signaling between cortical regions (Bastos et al., 2015; Bosman et al., 2012; Engel et al., 2001; Michalareas et al., 2016; Van Kerkoerle et al., 2014). There is converging evidence that activity in the gamma band (30-90Hz oscillations) is involved in feedforward processing. For example, microstimulation of monkey V1 induces gamma power in V4 (Van Kerkoerle et al., 2014). When monkeys are attending to one of two retinotopically distinct stimuli, gamma activity in V4 is coherent with gamma activity in the attended retinotopic region in V1 (Bosman et al., 2012). Moreover, the Granger-causal directionality of gamma coherence is stronger in the bottom-up direction (V1 to higher order visual areas) compared to the top-down direction (higher order visual areas to V1), in both primate ECoG and human MEG studies (Bastos et al., 2015; Bosman et al., 2012; Michalareas et al., 2016). Feedback signaling, on the other hand, is thought to involve slower oscillations in the alpha (8-12Hz) band in primates. For instance, microstimulation in V4 induces increase in alpha

power in V1 (Van Kerkoerle et al., 2014). Likewise, alpha oscillations in higher order visual areas modulate activity in the alpha band in V1 (Bastos et al., 2015; Michalareas et al., 2016). The temporal characteristics of these oscillations match the presumed functions of feedforward-feedback activity in predictive coding. In this model, feedback oscillations convey predictions about future stimuli and feedforward signals contain prediction errors. Updating predictions would then require faster integration of prediction errors, thereby necessitating feedback activity to evolve at a slower time scale as compared to feedforward activity (Michalareas et al., 2016).

The laminar organization feedforward and feedback oscillations is also similarly segregated in primate visual areas. In V1, V2, and V4, gamma power is the strongest in the superficial layers, whereas alpha power is strongest in the infragranular layers (Bastos et al., 2015; Buffalo et al., 2011). The vertical propagation pattern of feedforward and feedback oscillations matches their presumed roles within V1. Gamma oscillations initiates in the granular layer and then propagates to the supra- and infra-granular layers, whereas alpha activity begins in superficial and infragranular layers and then spreads towards the granular layers (Van Kerkoerle et al., 2014).

It is important to note that much of the previous work investigating feedforward and feedback oscillations was performed by analyzing pairwise interactions between neural activity at different cortical sites. While these discoveries have undoubtably laid the foundation of our understanding of the mechanisms that might confer feedforward and feedback signaling, processing of visual stimuli into a unified percept would require these pairwise interactions to be coordinated beyond the visual cortex and across widely distributed brain networks. An attractive neurophysiological candidate for the scaffold underlying large-scale organization of feedforward or feedback signals is a traveling wave.

Traveling waves

Spontaneous and stimulus evoked traveling waves, arising from successive depolarizations of neural populations, have been observed in a variety of experimental conditions and species and across vastly different spatial and temporal scales for almost a century (Adrian and Matthews, 1934; Ermentrout and Kleinfeld, 2001; Hughes, 1995; Muller et al., 2018; Sato et al., 2012; Wu et al., 2008). Stimulus evoked traveling waves have been demonstrated during wakefulness under conditions when presentation of the sensory stimuli is reliably accompanied by perception, but also in states like sleep and anesthesia when sensory perception does not occur (Adrian and Matthews, 1934; Ermentrout and Kleinfeld, 2001; Hughes, 1995; Muller et al., 2018; Sato et al., 2012; Wu et al., 2008). Thus, it remains unclear what role, if any, stimulus-elicited traveling waves play in processing sensory stimuli to ultimately enable perception.

Visual evoked traveling waves

It is well known that simple visual stimuli evoke complex spatiotemporal responses that spread over large cortical areas and long outlast stimulus presentation (Arieli et al., 1996). In human EEG recordings, macroscopic visual evoked traveling waves have been observed to spread across multiple cortical areas (Burkitt et al., 2000; King and Wyart, 2021). However, due to the distortions from volume conduction and cranial soft tissue and bone, the interpretation of the macroscopic waves in the EEG is unclear (Buzsáki et al., 2012; Muller et al., 2018).

On the mesoscopic scale—that of a single cortical region—visual evoked travelling waves have been observed in recordings of local field potentials (LFPs) and voltage sensitive dyes (VSDs). In the primary visual cortex (V1) simple visual stimuli reliably elicit travelling waves (Benucci et al., 2007; Muller et al., 2014; Nauhaus et al., 2012). Waves in the gamma band (30-80Hz) exhibit consistent phase propagation patterns after simple (Gabriel and Eckhorn, 2003; Vinck et al., 2010), as well as naturalistic visual stimuli (Besserve et al., 2015). Visual evoked

waves have also been observed in higher order visual areas, including V2 (Muller et al., 2014; Polack and Contreras, 2012; Xu et al., 2007b), V4 (Zanos et al., 2015), and the middle temporal (MT) cortex (Townsend et al., 2015b, 2017a). Yet, it is unclear whether travelling waves in the primary and higher order visual areas are interrelated.

Several studies examined the relationship between travelling waves in V1 and V2 (Muller et al., 2014; Polack and Contreras, 2012; Xu et al., 2007b), but reached conflicting results. Some studies concluded that visual evoked waves independently arose in V1 and V2 (Muller et al., 2014; Polack and Contreras, 2012), while others observed a complex interference pattern at the V1 - V2 border (Xu et al., 2007b). Thus, while visual stimuli elicit travelling waves in both primary and higher order cortical areas, the existence of macroscopic travelling waves spanning distinct cortical areas across the visual hierarchy first postulated on the basis of EEG has not been demonstrated with direct recordings of brain activity.

Mechanism of propagation

The circuit mechanism by which traveling waves propagate through the cortex is still under investigation. Many have inferred the propagation mechanism of observed traveling waves by comparing wave velocities to known axonal conduction speeds and transmission delays in cortico-cortical, cortico-thalamic or cortico-bulbar circuitry (Douglas and Martin, 2004, 2007; Jones, 1985; Prasad et al., 2020). Using a mesoscopic recording approach, traveling waves in V1 are often assumed to be mediated through horizontal fibers in cortical layers 2/3 (Bringuier et al., 1999; Girard et al., 2001; Muller et al., 2014, 2018). Macroscopic waves, on the other hand, tend to be mediated through myelinated association fibers (Muller et al., 2018; Waxman and Bennett, 1972)

However, neurophysiological evidence of wave propagation is currently scarce. A pivotal discovery comes from Wester and Contreras, who illustrate that layer 5 neurons are necessary

for the horizontal propagation of cortical signals, rather than layer 2/3 neurons in the barrel cortex in slice (Wester and Contreras, 2012). Therefore, layer 5 neurons may have an important role to play in the spatial propagation, velocity, and dampening time of traveling waves in the cortex.

Function of traveling waves in visual processing

A confluence of modeling and experimental findings suggests that stimulus-evoked spatiotemporal standing, travelling and rotating waves may coordinate cortical activity (Ermentrout and Kleinfeld, 2001; Muller et al., 2018; Wu et al., 2008). Propagating waves of subthreshold activity are proposed to affect cortical function by providing background depolarization to populations of neurons, thereby modulating the probability of synaptic transmission, and promoting local firing synchrony (Wu et al., 2008). Moreover, the phase of cortical waves fluctuates dynamically in a spatially coherent fashion. This can lead to phasic changes in neuronal excitability, thereby making neuronal firing context-dependent (Carandini et al., 2015; Ermentrout and Kleinfeld, 2001; Muller et al., 2018; Wu et al., 2008).

Recently, some have begun empirically demonstrating the functional role of cortical waves in the processing of visual stimuli and perception (Davis et al., 2020; Zanos et al., 2015). For example, saccadic eye movements initiate 20-40Hz travelling waves in V4. By modulating neuronal firing, these saccade-triggered waves may prioritize neural responsiveness to stimuli in the new spatial location (Zanos et al., 2015). Moreover, the phase of spontaneous waves in marmoset MT visual area, modulates the firing rates of MT neurons, and the probability of perceiving of peri-threshold visual stimuli (Davis et al., 2020). Such findings argue that travelling waves do indeed play a role in shaping sensory perception.

Thus, these observations beg the question, do the oscillations that confer feedforward and feedback signaling between pairs of cortical sites organize into coherent traveling waves? If so, we would expect that visual stimuli would evoke two traveling waves, the first carrying feedforward signals, and second conveying feedback activity, that would each span over multiple hierarchical areas involved in visual processing (Chapter 2). Moreover, if these waves exist, would they organize neural firing across cortical regions, much like how saccade evoked waves modulate neural firing rates across retinotopic space in V4 (Zanos et al., 2015) (Chapter 2). Finally, if these waves are found during wakefulness, would they be disrupted by hypnotic doses of general anesthetics, as some recent theories of the mechanism of anesthetics induced unconsciousness would suggest (Chapter 3 and 4)?

Anesthetic mediated breakdown of feedback connectivity and integration

An emerging explanation of anesthetic induce loss of consciousness is that sedative-hypnotic drugs disrupt the hierarchical processing and integration of sensory information (Mashour, 2006).

The literature regarding the effects of anesthetics on feedforward signaling yields somewhat contradictory results. For example, using the same spontaneous human EEG dataset, Ku et al found that sevoflurane and propofol decrease effective feedforward connectivity between frontal and parietal areas by analyzing data using symbolic transfer entropy, but feedforward connectivity is preserved when analyzing data through an evolution map approach (Ku et al., 2011). Likewise, in rodent LFP studies, halogenated anesthetics produce an increase in feedforward transfer entropy at 30Hz, but a decrease in feedforward entropy at 50Hz between frontal and parietal areas (Imas et al., 2005b).

Nevertheless, converging evidence points to the notion that multiple anesthetic agents disrupt feedback connectivity (Mashour, 2014; Mashour and Hudetz, 2017). For instance, feedback effective connectivity between frontal and parietal cortices decrease in rats under isoflurane

(Hudetz and Imas, 2007), and human subjects under propofol, sevoflurane, and ketamine, compared to during wakefulness (Jordan et al., 2013; Ku et al., 2011). The pattern of loss of feedback connectivity during states of unconsciousness has also been noted at the level of evoked potentials. Specifically, loss of consciousness is associated with the disappearance of the late phase of evoked potentials, which are thought to reflect sensory processing from higher order areas (Del Cul et al., 2007; Ferrarelli et al., 2010; Hudetz et al., 2009; Mashour, 2014; Massimini et al., 2005). However, the early phase of evoked potentials, which correlate with primary sensory processing, are preserved during states of unconsciousness (Del Cul et al., 2007; Ferrarelli et al., 2010; Hudetz et al., 2009; Massimini et al., 2005).

Finally, anesthetics have been shown to disrupt the integration of cortical activity both neurophysiologically and with network connectivity. For example, isoflurane preferentially decreases the amplitude of visual evoked responses measured in the auditory cortex of rats, and also decreases the amount of auditory evoked firing in primary visual cortex in ferrets (Raz et al., 2014; Sellers et al., 2015). Similarly, human fMRI functional connectivity studies have shown that integration decreases and modularity increases during sleep, anesthesia and vegetative states (Achard et al., 2012; Boly et al., 2012; Monti et al., 2013; Rosanova et al., 2012; Tagliazucchi and Laufs, 2014).

Conclusion

Many of the studies describing the effects of anesthesia on feedforward and feedback connectivity have been done using spontaneous human data (Jordan et al., 2013; Ku et al., 2011) or in sensory evoked animal studies with low spatial resolution (Hudetz and Imas, 2007). Here, by recording high density ECoG in mice presented with simple visual stimuli, and analyzing the data with singular value decomposition (described in detail in Chapter 2), a dimensionality reduction tool well suited for spatiotemporal data, we investigate the propagation patterns of visual evoked

oscillations over almost an entire cortical hemisphere in awake mice (Chapter 2). We also

investigate how three mechanistically distinct anesthetic agents disrupt the spatiotemporal

properties of single trial VEPs (Chapter 3 and 4). We hypothesize that all three anesthetics will

disrupt the spatial spread and curtail the temporal signature of slower frequency components of

VEPs, thereby suggesting that a shared feature of the drugs tested is the disruption of feedback

signaling.
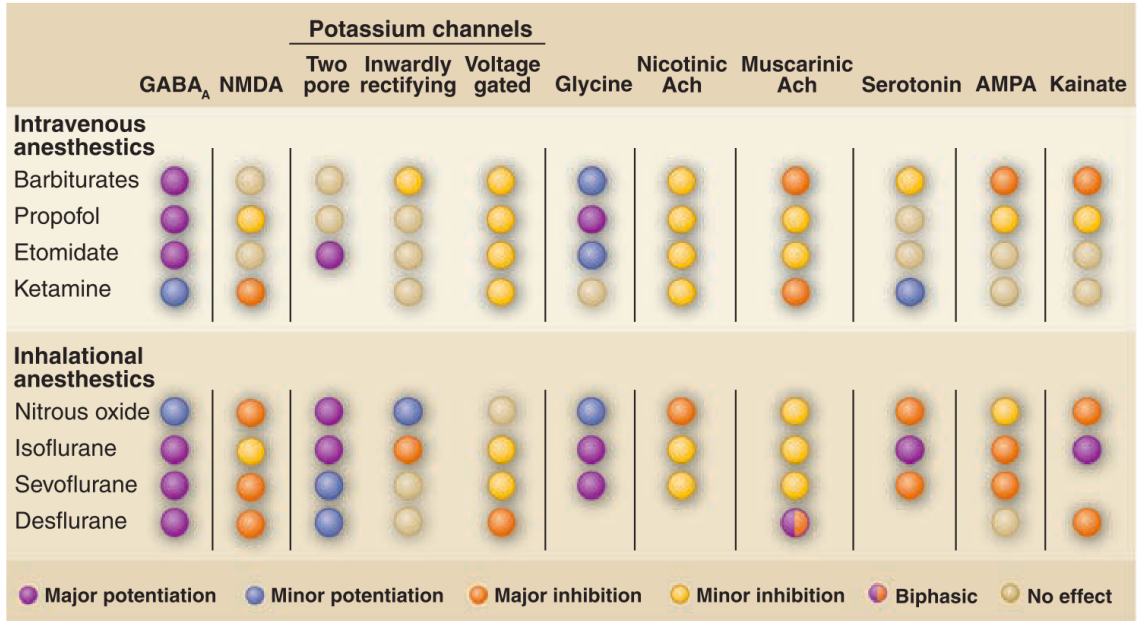
Figure 1.1: Heterogeneity and promiscuity of anesthetic binding to reception targets

Interactions of some commonly used intravenous and inhaled anesthetics with their interactions at receptor targets. Abbreviations: Ach, acetylcholine; AMPA, a-amino-3-hydroxy-5-methyl-4-isoxazolepropionic acid; GABAA, g-aminobutyric acid, type A; NMDA, N-methyl-D-aspartate.

*Adapted from Alkire, Hudetz, and Tononi, *Science*, 2008, (Alkire et al., 2008)
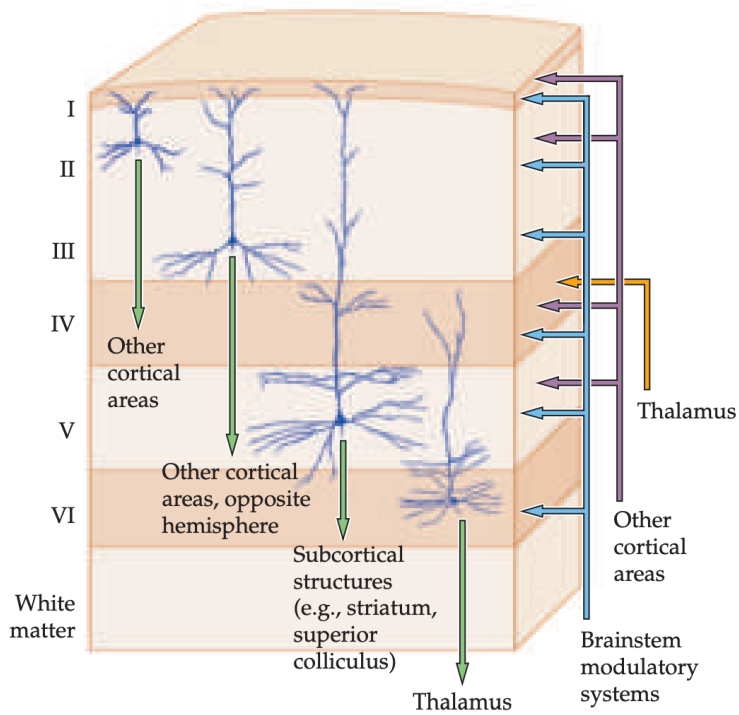
Figure 1.2: Laminar Cortical Circuitry

Neocortical circuits present in most primary sensory areas. The orange arrow indicates the input of relay thalamic signals to mainly layer 4 of the cortex. The purple arrow avenues of cortico-cortical input, which occur predominantly through horizontal connections in layers 2/3 and layer 5. The green arrows denote laminar output including cortico-cortical fibers in layers 2/3 and layer 5, as well as cortico -bulbar pathways in layer 5 and cortico-thalamic fibers from layer 6. The blue arrow denotes neuromodulatory input from brain stem nuclei.

*Adapted from *Neuroscience*, Purves et.al 2004, (Purves et al., 2004)
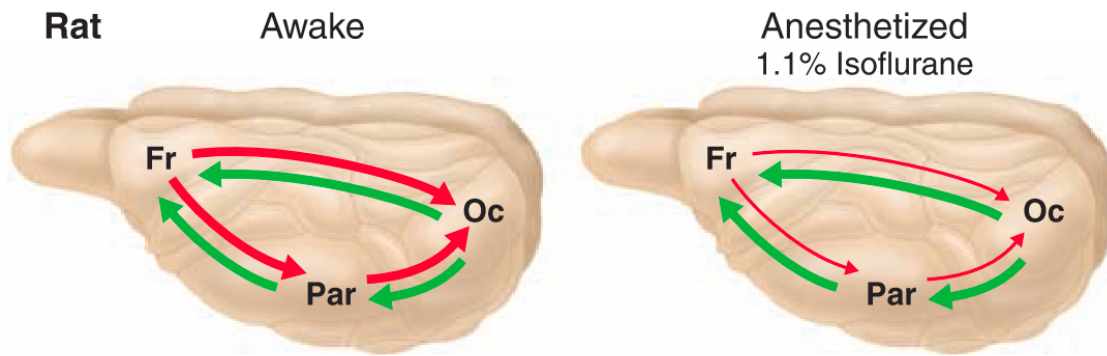
Figure 1.3: Anesthetics agents may ablate perception by disrupting feedback circuitry

Right: Feedforward (green) and feedback (red) interactions within the gamma band (as measured by transfer entropy) is balanced between primary, association, and frontal areas in awake rats. Left: Feedback interactions are preferentially reduced, but feedforward connectivity remains when rats are under 1.1% isoflurane

*Adapted from Alkire, Hudetz, and Tononi, *Science*, 2008, (Alkire et al., 2008)

CHAPTER 2 - Visual evoked feedforward-feedback travelling waves organize neural activity across the cortical hierarchy in mice

Abstract

Sensory processing is distributed among many brain regions that interact via feedforward and feedback signaling. It has been hypothesized that neuronal oscillations mediating feedforward and feedback interactions organize into travelling waves. However, stimulus evoked travelling waves of sufficient spatial scale have never been demonstrated directly. Here, we show that simple visual stimuli reliably evoke two traveling waves with spatial wavelengths that cover much of the cerebral hemisphere in awake mice. 30-50Hz feedforward waves arise in primary visual cortex (V1) and propagate rostrally, while 3-6Hz feedback waves originate in the association cortex and flow caudally. The phase of the feedback wave modulates the amplitude of the feedforward wave and synchronizes firing between V1 and parietal cortex. Altogether, these results provide direct experimental evidence that visual evoked travelling waves percolate through the cerebral cortex and coordinate neuronal activity across broadly distributed networks mediating visual processing.

Introduction

Feedforward and feedback signaling contribute to the hierarchical processing of sensory stimuli, creating predictions and attaching behavioral context to the sensory world (Bastos et al., 2015; Bosman et al., 2012; Felleman and Van Essen, 1991; Mejias et al., 2016; Michalareas et al., 2016; van Ede et al., 2015; Vecchia et al., 2020). Feedforward processing involves bottom-up assembly of abstract stimulus representations in higher-order areas from simple receptive fields in the primary cortex (Felleman and Van Essen, 1991; Markov et al., 2014). Feedback processing, in contrast, involves top-down influences such as attention, prediction, and context (Felleman and Van Essen, 1991; Markov et al., 2014). Formulating predictions about the next

sensory stimulus or deciding which stimulus to pay attention to requires temporal integration (Bastos et al., 2015; Friston, 2008; Friston and Buzsáki, 2016; Posner et al., 2018). Thus, it is thought that feedback modulation evolves on a slower time scale relative to feedforward processing (Alamia and VanRullen, 2018; Bastos et al., 2015; Bosman et al., 2012).

Feedforward – feedback interactions between the different cortical regions involved in sensory processing must be coordinated to give rise to integrated percepts situated in the behavioral context. The role of neuronal oscillations in coordinating neuronal activity has been a subject of intense investigation, especially in primate vision. By analyzing individual pairwise interactions between neural oscillations present at different areas of the primate cortex, many prominent studies have shown that feedforward processing involves gamma oscillations, whereas feedback signaling uses alpha (8-12Hz) oscillations (Bastos et al., 2015; Bosman et al., 2012; Engel et al., 2001; Michalareas et al., 2016; Van Kerkoerle et al., 2014). Thus, consistent with their presumed behavioral roles, feedback signalling utilized slower temporal oscillations compared to feedforward channels.

Pairwise interactions between oscillations in different cortical sites during processing of sensory stimuli raise several fundamental questions. Do pairwise feedforward and feedback interactions give rise to a single coherent assembly that coordinates activity among the different cortical regions involved in processing sensory stimuli? How does the brain coordinate the feedforward and feedback processing given the significant differences in timescales? One possibility for a neurophysiological process that could coordinate activity amongst multiple regions in the processing hierarchy is a spatiotemporal travelling wave. Early EEG work identified travelling waves in the feedforward and feedback directions (Adrian and Matthews, 1934; Adrian and Yamagiwa, 1960; Darrow and Hicks, 1965; Goldman et al., 1948; Hughes, 1995). However, due to the low spatial resolution of the EEG, the interpretation of these findings is unclear. Indeed, travelling waves recorded directly from the cortical surface have different speeds and propagation patterns compared to their EEG counterparts (Bahramisharif et al., 2013; Hangya et

18

al., 2011; Mak-McCully et al., 2015; Muller et al., 2018). Both spontaneous and stimulus evoked travelling wave-like phenomena have been identified using voltage sensitive dyes and neurophysiological recordings from brain parenchyma in the primary and higher order visual areas (Benucci et al., 2007; Besserve et al., 2015; Bringuier et al., 1999; Davis et al., 2020; Gabriel and Eckhorn, 2003; Muller et al., 2014; Nauhaus et al., 2009; Polack and Contreras, 2012; Sato et al., 2012; Townsend et al., 2015a; Xu et al., 2007a). Most of this work however, focused on a single cortical area rather than inter-area communication. Some studies attempted to identify spatiotemporal waves that span multiple cortical sites and concluded that sensory stimuli trigger two independent cortical waves, which travel along the horizontal fiber network in each site (Muller et al., 2014; Polack and Contreras, 2012). Other studies identified a reflective boundary between the primary and the secondary visual cortex (Xu et al., 2007a). Thus, while a single spatiotemporal wave of activity offers an attractive possibility for coordinating cortical activity, the existence of stimulus-evoked travelling waves with sufficient spatial scale to span the cortical hierarchy has never been directly demonstrated. Furthermore, the relationship between feedforward-feedback processing of sensory stimuli and the travelling waves evoked by them in the cortex has not been clarified.

We deploy a combination of high-density neurophysiological recordings and analytic techniques to identify large scale spatiotemporal patterns of neuronal activity evoked by a single presentation of a simple, supra-threshold visual stimulus. By focusing our analyses on global activity patterns, rather than pairwise interactions, we show that both the feedforward and feedback aspects of visual evoked activity form travelling waves that percolate through much of the cortex in awake mice. Feedforward waves have a fast (30-50Hz) temporal frequency and propagate from V1 rostrally. Feedback waves are characterized by a slow (3-6Hz) oscillation, thought to be a rodent analogue of the primate alpha oscillation. These feedback waves propagate caudally from association cortices towards V1. The phase of the feedback wave modulates the amplitude of the feedforward wave, thereby forming a single multiplexed visual evoked spatiotemporal response. Finally, we demonstrate that the feedback wave entrains firing

of individual neurons in both V1 and in parietal association cortex. As a consequence, following stimulus presentation, previously uncorrelated firing in V1 and parietal cortex phase lock their firing in relation to the stimulus to form a transient neuronal assembly. Thus, we provide direct evidence that feedforward-feedback interactions organize into large scale traveling waves evoked by simple visual stimuli. These waves serve as a scaffold that coordinates neural firing across distant cortical areas.

Results

Our primary goal is to experimentally define salient spatiotemporal signatures of responses to simple visual stimuli. To accomplish this, we performed high density *in vivo* electrophysiological recordings in awake head fixed mice (n = 13) (Methods for verification of wakeful states, Figure 2.1, Video 2.1). Local field potentials (LFPs) were recorded from the dural surface using a 64 channel electrocorticography (ECoG) grid placed over the left hemisphere (Figure 2.2a). Two 32 channel laminar probes were also inserted perpendicular to the cortical surface targeting the primary visual cortex (V1) and the posterior parietal area (PPA). Histological and neurophysiological (Methods) localizations of the laminar probes were used to triangulate the stereotaxic locations of the individual ECoG electrodes. The ECoG grid covered a significant fraction of the cerebral hemisphere including visual, association, retrosplenial, somatosensory, and motor/frontal areas (Figure 2.2b).

Simple, brief visual stimuli evoke widespread time-locked coherent oscillations at both high (30-50Hz) and low (3-6Hz) frequencies

As in previous work (Aggarwal et al., 2019; Childers et al., 1987; Churchland et al., 2010; Liberati et al., 1991), the visual-evoked potential (VEP) in V1 (Methods) varies from trial-to-trial. Nevertheless, early fast oscillations (30-50Hz) followed by longer lasting slow oscillations (3-6Hz) are reliably identified from trial to trial (Figure 2.2c). Analysis of the inter-trial phase coherence

(ITPC) confirms that these two oscillations are consistently phase locked to the stimulus (Stouffer's *p-values*<0.00001 compared to time shuffled data) (Figure 2.2d). ITPC computed over the first 100 ms after the stimulus reveals two peaks centered at 3-6Hz and 30-50Hz. The 3-6Hz oscillation remains coherent for 500ms after the stimulus (Figure 2.2e). Because these two oscillations (fast, 30-50Hz and slow, 3-6Hz) are reliably phase locked to the stimulus in all mice, we focus our subsequent analyses on these oscillations.

Phase locking of fast and slow oscillations to the stimulus is not limited to V1. Both fast and slow oscillations are phase locked to the stimulus across much of the cortical surface (Figure 2.2f and 2.2g, respectively). Phase locking to the stimulus over large areas of the cortical surface strongly suggests that oscillations recorded at different sites are interdependent. Consistent with this suggestion, LFPs filtered at fast and slow frequencies in V1 and PPA exhibit phase coupling (Figure 2.2h and 2.2i). Interestingly, oscillations at both temporal frequencies have a non-zero phase lag between V1 and PPA (Figure 2.2h, and Figure 2.21). This raises the possibility that the stimulus evokes spatiotemporal waves that percolate across the cortex. The spatial characteristics of this wave, however, are not readily apparent from just observing pairwise phase relationships. Thus, we examined the spatial characteristics of the visual evoked oscillations that are simultaneously recorded across multiple locations on the cortical surface. Trial average LFP filtered at fast and slow frequencies along the anterior-posterior (AP) axis recorded in a single representative mouse are shown in Figure 2.3a and 2.3b respectively, (see Video 2.2, and Video 2.3 for propagation of visual evoked fast and slow waves, respectively, over the cortical surface). Oscillations observed at each electrode are consistently phase shifted in relation to oscillations at neighboring electrodes. Thus, the overall ensemble activity profile resembles traveling waves at both frequency bands. Remarkably, the fast wave is initiated in the visual cortex and propagates anteriorly, while the slow oscillation initiates rostral to V1 and spreads in the opposite direction (Figure 2.3C, Video 2.4). Note that travelling waves that propagate through uniform media have a uniform spatial phase gradient at all locations. Consequently, the phase offset ought to grow linearly with distance. This is approximately true of signals over short distances in Figure 2.3. In

21

contrast, over long distances a clear nonlinear relationship between phase offset and distance is seen. This nonlinear relationship implies that the propagation of these wave-like patterns is likely to depend on the specifics of network architecture in different cortical regions.

Coherent spatiotemporal waves are detected using complex SVD

While data in Figure 2.3 strongly suggest a propagating wave-like phenomenon, the interpretation of these data is somewhat limited. First, the LFP is a complex mixture of spontaneous and evoked activity (Arieli et al., 1996; Kisley and Gerstein, 1999). Second, trial averaging may obscure single trial behavior. Thus, to provide additional evidence that simple visual stimuli elicit travelling wave-like phenomena, we applied a methodology to separate spontaneous from evoked activity and to characterize spatiotemporal features of evoked activity on a single trial level. For this purpose, we utilized Singular value decomposition (SVD) of the complex-valued analytical signals derived from bandpass filtered LFPs.

Singular value decomposition (SVD) factorizes a spatiotemporal matrix into mutually orthogonal spatiotemporal modes:

$$\mathbf{A} = \mathbf{USV^T}$$

where *A* is an *n* by *t* matrix that contains *n* channels of analytical signals sampled at *t* time points, *U* is an *n* by *n* complex valued spatial matrix in which each column encodes the phase and amplitude of a single mode at each channel, *V* is a *t* by *t* complex valued temporal matrix in which each row encodes the instantaneous phase and amplitude of each mode at each time point. Finally, *S* is an *n* by *t* diagonal real valued matrix which encodes the fraction of the total signal contained in each mode.

The advantage of performing SVD on the complex-valued analytical signal is that projecting the data onto the complex plane linearizes phase relationships between channels. In

contrast, phase-shifted real-valued oscillations across channels would exhibit correlations at different time lags and are therefore not easily factorizable using SVD or similar dimensionality reduction techniques. We highlight the utility of complex SVD with synthetic data in Figure 2.4.

Here, we performed SVD on the analytical signal of single trials filtered at fast and slow frequencies. 72% of variance of single trial VEPs was captured by the first ten singular modes (*95% Confidence Interval* = 62%-81%). We then defined the most visually responsive mode for each trial as the mode in which the post-stimulus temporal amplitude increases the most compared to pre-stimulus amplitude (Figure 2.5). The most visually responsive mode was most often associated with the largest singular value and thus contained the highest amount of signal variance. The results of the analysis are robust to the changes in the total number of modes considered for the analysis.

Visual evoked waves have a consistent phase relationship from trial to trial and across animals.

The spatial phases of the most visually responsive mode from each single trial were aggregated across trials and mice (Methods). The phase difference between visual evoked fast waves in two locations in V1 (black and red diamonds in Figure 2.6c and d) reveals a consistent phase offset across trials and mice (Figure 2.6a). As the distance from the V1 electrode is increased, the phase difference between the oscillations grows concomitantly (Figure 2.6b). Consistent with the average LFP data (Figure 2.3), a progressive increase in phase offset with distance suggests that the activity evoked by the visual stimulus on a single trial level has characteristics resembling a travelling wave. Furthermore, the tight phase offset distribution implies that the spatial properties of these evoked waves are highly consistent from trial to trial and between animals.

The spatial phase of the most visually responsive mode averaged across trials and animals is shown in Figure 2.6c and 2.6d for the fast and slow oscillations, respectively. This confirmed that throughout most of the cortical surface, the phase relationship between evoked fast and slow oscillations is consistently observed from trial to trial and among animals. Consistent with the example observed in the average filtered signal (Figure 2.3), the phase gradient for fast and slow oscillations evolves in approximately opposite directions. Thus, a brief visual stimulus elicits both fast and slow spatiotemporal activity patterns that resemble travelling waves and percolate over the cortical surface for hundreds of milliseconds. The fast wave propagates in the feedforward direction from the visual cortex towards higher order cortical areas. The slow wave propagates in the feedback direction from the higher order cortices back towards the primary visual cortex. Given the initiation zones and directions of propagation, we will refer to the fast visual evoked wave as "feedforward" and the slow visual evoked wave as "feedback."

Similar feedforward and feedback propagating waves were observed for weaker visual stimuli (Methods). For weaker stimuli, the propagation of the fast visual evoked waves was predominantly limited to V1 and was not affected by the stimulus intensity. In contrast, the spatial extent of the feedback slow visual-evoked wave strongly depended on stimulus intensity. For lowest luminance stimulus, the feedback slow wave was principally observed in V1. However, for higher luminance stimuli, the feedback travelling slow wave involved much of the cortex (Figure 2.7). Thus, the spatial extent of the feedback wave tracks stimulus intensity, in a manner that mirrors psychophysics (Denman et al., 2018; Wysocki and Stiles, 1982).

High and low frequency waves are present throughout the cortical layers in V1 but are constrained to the superficial layers of the posterior parietal cortex.

To identify the circuits mediating the visual evoked waves, we computed current source density (CSD) from the two laminar probes targeting V1 and PPA (Figure 2.8a, 2.8b, 2.8f). In V1,

we identified a canonical CSD pattern. The first sink occurs in the granular layer. Subsequently, alternating sink and source patterns occur throughout the cortical column, revealing communication among the cortical layers (Figure 2.8c). Less is known about the neurophysiological responses of the PPA to visual stimuli. We find the first sink at 0.15 mm below the cortical surface, which appears at a longer latency than in V1. Moreover, the majority of the CSD signal in PPA is confined to the superficial layers (Figure 2.8g).

Frequency domain analysis reveals strong ITPC for the fast frequency at all cortical layers in the first 100 ms following the stimulus in V1. A similar pattern is observed for the slow oscillation for ~ 500 ms after the stimulus (Figure 2.9a, 2.9c). Within the PPA, in contrast, most of the ITPC at both high and low frequencies is concentrated in the superficial cortical layers (Figure 2.9b, 2.9d).

To determine the laminar organization of fast and slow waves, we averaged the filtered CSD data at each depth within each mouse. Consistent with other work on visual evoked gamma oscillations in V1, the fast waves originate in layer 4 in V1 and propagate to supra- and infra-granular layers (Figure 2.8d), indicating a critical role of thalamocortical circuitry in the initiation of the visual evoked gamma oscillations (Reinhold et al., 2015c; Saleem et al., 2017). In contrast, in the PPA, visual evoked fast oscillations are predominantly seen in the superficial layers (Figure 2.8h). The visual evoked slow oscillations originate in the superficial layers in both V1 and PPA (Figure 2.8e, 2.8i). These observations imply that the fast visual evoked waves are initiated through the interactions between the thalamus and the input layer 4 of V1 and subsequently propagate through the corticocortical circuitry involving supra- and infra- granular layers in the feedforward direction towards higher order cortices (Douglas and Martin, 2004, 2007; Feldmeyer et al., 2002, 2006; Krieger et al., 2007; Wester and Contreras, 2012). In contrast, the slow visual evoked wave predominantly propagates in the ventral direction through the cortical column, supporting the conclusion that it is primarily mediated by the feedback cortico-cortical interactions.

25

Both fast and slow visual evoked waves have large spatial frequencies

It is commonly thought that waves with higher frequency tend to be localized in space, whereas slow temporal frequency waves involve large areas of the cortex (Kopell et al., 2000). In contrast to these observations, we show that both the fast and the slow oscillations involve much of the cerebral hemisphere for supra-threshold stimuli. Further, examination of the recordings in Figure 2.3a and 2.3b suggests that despite their difference in temporal frequency, the spatial wavelengths of both waves are similar. We confirm this observation and estimate the most common spatial wavelengths of the fast and slow waves to be 12.7 mm/cycle and 12.5 mm/cycle, respectively (Figure 2.10a). These spatial wavelengths are on or above the scale of a mouse cerebral hemisphere (Ermentrout and Kleinfeld, 2001). Because of the nonlinear dependence of phase offset on distance (Figure 2.3) each travelling wave does not have a well-defined single spatial wavelength. Nevertheless, local estimates of spatial wavelengths can be obtained from the spatial phase gradient (Figure 2.6c, 2.6d) at each cortical site (Figure 2.11a, 2.11b). Thus, while visual evoked fast and slow waves are distinct from canonical travelling waves in uniform medium and do not have a single spatial wavelength, the spectra of spatial wavelengths for the fast and slow oscillations are comparable. The propagation velocity of the fast oscillations, consequently, is approximately an order of magnitude faster than the slow oscillation ($median_{fast}$= 0.8 m/s, IQR_{fast}= 0.5-1.58 m/s, and $median_{slow}$= 0.11 m/s, IQR_{slow}= 0.07-0.20 m/s, for the slow and the fast waves respectively). This, again is consistent with data in Figure 2.3. The differences in the propagation velocities suggest that the fast and slow visual evoked waves are mediated by different circuit mechanisms.

Fast and slow oscillations comprise a single multiplexed visual evoked spatiotemporal response

Until this point, we have treated the high and low frequency visual evoked waves as independent entities. Furthermore, we only considered the waves observed in the immediate aftermath of the stimulus. However, analysis of single trials in V1 reveals rhythmic waxing and waning of the amplitude of fast oscillations aligned to the phase of the slow oscillation (Figure 2.12a). Similar phase amplitude coupling is also observed in the PPA (Figure 2.12b); although the amplitude of fast oscillations peaks at different phases of the slow oscillation. Indeed, significant phase amplitude modulation is present throughout the cortical surface (Figure 2.12c). Moreover, the phase relationship varies systematically with cortical location (Figure 2.12d). Thus, the fast and slow waves are not independent phenomena, but instead are different aspects of the same integrated spatiotemporal activity pattern, which is reliably evoked by the visual stimulus.

The phase of slow visual evoked waves modulates the firing rates of neurons both in V1 and PPA

Fast oscillations in the gamma range are thought to coincide with neuronal firing. In contrast slower oscillations are dominated by synaptic potentials (Buzsáki et al., 2012). The phase amplitude coupling between the fast and slow visual evoked oscillations may therefore suggest that the slow feedback oscillation modulates neuronal firing. To determine whether this is indeed the case, we tested whether the slow visual evoked waves entrain firing of single units in V1 and PPA. We first isolated single units throughout the cortical lamina in V1 and PPA (155 in PPA and 186 in V1, Figure 2.13a and 2.13b for representative neurons in each area, respectively). Raster plots of these neurons (Figure 2.13c and 2.13d) show that after the stimulus the firing of the neurons in both areas is entrained by the slow visual evoked oscillation. To quantify this observation, we computed spike field coherence for each single unit and the CSD filtered at the slow frequency band from the same lamina. 32 out of 155 units in PPA and 98 out of 186 units in V1 exhibited significant spike field coherence after the stimulus (Figure 2.13e and 2.13f). Spike field coherence for the same units was significantly smaller before the stimulus

($p<10^{-5}$ *Mann-Whitney U-test*). Thus, visual evoked slow oscillations entrain a significant fraction of neurons both in the primary visual cortex and the association cortex. While many single units were entrained in both cortical areas, the phase of maximum firing was not the same across different units (Figure 2.13e and 2.13f). Indeed, the phase of maximum firing in each area swept through an entire cycle of the slow wave. Thus, each visual stimulus evokes a sequence of neuronal activation in both areas that is orchestrated by the slow oscillation.

If the visual evoked waves were responsible for coordinating neuronal activity across disparate regions in the cortical hierarchy, one would expect that neuronal firing would become transiently correlated after stimulus presentation. Consequently, we hypothesized that V1 and PPA neurons that are entrained by the slow wave would become transiently correlated after the stimulus. As expected, prior to the stimulus, firing in V1 and PPA was largely uncorrelated (Figure 2.13g). However, after the stimulus, many of these previously independent neurons became correlated over half of the wave cycle length of the slow wave (~100ms) (Figure 2.13h). Thus, as the feedback slow visual evoked wave propagates from the higher order cortical areas towards the primary sensory cortex, it entrains a sequence of neuronal activation in the PPA and V1. This provides a neurophysiological insight into how simple sensory stimuli produce coordinated patterns of neuronal activity that span multiple cortical areas.

Discussion

Here, we show that in awake mice, a brief presentation of a simple visual stimulus reliably evokes two traveling waves. The spatiotemporal characteristics of these waves are highly stereotyped across individual trials and across animals. Fast (30-50Hz) waves begin in layer 4 of V1 and travel anteriorly in a feedforward manner. Slow (3-6Hz) waves are initiated in the superficial layers of the higher order areas and travel posteriorly in a feedback fashion. These waves are tightly coupled forming a single multiplexed spatiotemporal wave-like activity pattern observed throughout the cortex. The phase of the feedback wave modulates the firing of individual neurons both in the association cortex and in V1. A consequence of this entrainment is

28

that previously independent neurons in V1 and PPA form a transient coordinated assembly after stimulus presentation. In this way, the feedback and the feedforward aspects of the multiplexed visual evoked waves coordinate neuronal activity across distant cortical regions involved in the processing of visual stimuli.

The role of neuronal oscillations in mediating feedforward and feedback sensory processing has been predominantly studied by analyzing pairwise signal covariation. Our chief contribution is that a set of such pairwise coupled neuronal oscillations together form a single coherent spatiotemporal pattern that consists of two interacting waves. Spontaneous and stimulus evoked travelling waves have been observed in the EEG (Adrian and Matthews, 1934; Adrian and Yamagiwa, 1960; Darrow and Hicks, 1965; Goldman et al., 1948; Hughes, 1995). However, the interpretation of the EEG is hindered by low spatial resolution and volume conduction. Further, intracranial recordings (ECoG) did not corroborate the EEG findings (Bahramisharif et al., 2013; Hangya et al., 2011; Mak-McCully et al., 2015; Muller et al., 2018), leaving the existence and functional role of macroscopic traveling waves in question. Novel experimental imaging techniques using voltage sensitive dyes (VSDs) reveal mesoscopic travelling waves that are confined by anatomical boundaries between cortical regions (Muller et al., 2014; Polack and Contreras, 2012) or produce complex interference patterns at the inter-region boundaries (Xu et al., 2007a). However, most mesoscopic waves recorded with VSDs do not take into consideration the temporal frequency of travelling waves and focus primarily on their spatial propagation properties (Benucci et al., 2007; Davis et al., 2020; Muller et al., 2014, 2018; Polack and Contreras, 2012; Sato et al., 2012; Townsend et al., 2015a; Xu et al., 2007a). Here, by identifying two temporal frequencies that are reliably phase locked to the stimulus, we deconstruct the overall spatiotemporal response pattern into two distinct travelling waves that percolate through the brain in opposite directions. This, in turn, allows us to experimentally marry pairwise feedforward-feedback interactions involving different temporal frequencies and travelling cortical waves into a single, unified framework.

Feedforward and feedback aspects of sensory processing serve fundamentally different roles. Feedforward processing assembles increasingly abstract representations of sensory stimuli. Feedback processing, in contrast, situates sensory stimuli within a behavioral context. Based on these functional differences, one expects that the neurophysiological processes that mediate feedback signaling must occur on a slower time scale than those involved in feedforward interactions. This assertion is consistent with experimental work in primates (Bastos et al., 2015; Bosman et al., 2012; Engel et al., 2001; Michalareas et al., 2016; Van Kerkoerle et al., 2014; Womelsdorf et al., 2012). Many studies demonstrate that the faster gamma oscillations underlie feedforward processing while the slower, alpha oscillations, relay feedback processing. This difference in time scales is confirmed by our experimental observations – the temporal frequency of the feedback wave is approximately ten times slower than the feedforward wave. While there is a numerical discrepancy between the temporal frequency of alpha oscillations in primates and the 3-6Hz feedback wave in our work, multiple lines of evidence strongly suggest that the 3-6Hz wave in mice is analogous to the primate alpha oscillations (Bollimunta et al., 2008, 2011; Dougherty et al., 2017; Einstein et al., 2017; Nestvogel and Mccormick, 2021; Senzai et al., 2019; Speed et al., 2019). Our identification of feedforward and feedback processes as interacting travelling waves permits an extension of this postulate. We find that the propagation velocity of the feedforward wave is also roughly an order of magnitude faster than that of the feedback wave. This difference in propagation velocities potentially allows the feedback modulation to integrate across recent sensory stimuli, thereby situating them in behavioral context.

We refer to the activity patterns evoked by visual stimuli as "traveling waves". However, it is important to note that these large-scale spatiotemporal responses differ from simple waves in uniform medium. Imagine that a response to a visual stimulus is akin to a raindrop falling into a still pond. In this highly idealized case, the raindrop would create a wave radiating outward at uniform speed and spatial wavelength. This simple scenario is indeed similar to travelling waves

30

within a single cortical area. Much like waves on the pond, travelling cortical waves typically have tight distributions of propagation speeds and spatial wavelength (Besserve et al., 2015; Muller et al., 2014; Xu et al., 2007a). Our results are in agreement with these findings over relatively short spatial scales (Figure 2.12). However, over larger scales, the apparent "viscosity" of the medium changes. There is a clear departure from the linear dependence of the spatial phase gradient on distance. This gives rise to a broad spectrum of spatial wavelengths and propagation velocities. The "viscosity" of the brain is thought to arise from conduction delays between different neuronal oscillators (Ermentrout and Kleinfeld, 2001). The observation that speed of wave propagation deviates from a pure travelling wave on large spatial scales in a systematic fashion suggests therefore that different conduction delays are involved on small and large scales.

It has been hypothesized that the interactions between distinct neuronal oscillators are mediated by horizontal fibers in superficial cortical layers. The spatial properties of traveling waves within a single cortical region are consistent with this hypothesis (Bringuier et al., 1999; Grinvald et al., 1994; Muller et al., 2014). The propagation speeds of the visual evoked travelling waves observed herein are also in the range of conduction delays of cortico-cortical fibers. Direct laminar recordings showing preferential involvement of superficial cortical layers provide additional evidence for this hypothesis. While on the scale of a single cortical region, wave propagation is likely predominantly mediated by horizontal cortico-cortical fibers, additional mechanisms likely contribute to propagation over large spatial scales. For instance cortico-thalamic and corticobulbar loops contribute significantly to processing of visual stimuli and involve superficial cortical layers (Brumberg et al., 2003; Burkhalter, 1989; Douglas and Martin, 2004, 2007; Feldmeyer et al., 2002, 2006; Glickfeld et al., 2013; Townsend et al., 2017b; Wester and Contreras, 2012). The contribution of multiple anatomical pathways with distinct conduction velocities together with anisotropic connectivity likely distort the speed and direction of propagation of travelling waves on large spatial scales. This conjecture is supported by models of coupled oscillators which suggest that specific patterns of conduction delays strongly influence the spatial features of the wave-like phenomena (Jeong et al., 2002). These results suggest a

31

refinement to the current mechanistic models of travelling wave phenomena. Investigation of the relationship between the underlying anatomy and propagation properties of visual evoked waves on macroscopic scale may enrich our understanding of the relationship between neural architecture and the coordination of neuronal activity across the hierarchy of the visual system.

Our results demonstrate that the visual evoked waves are attractive candidates for organizing the feedforward-feedback computations necessary for sensory processing. Nevertheless, the full contribution of evoked waves to the processing of visual stimuli is unclear for several reasons. First, while we note the relationship between stimulus intensity and extent of the feedback wave, we do not directly address the behavioral significance of visual evoked travelling waves. Second, it remains unknown whether evoked travelling waves contain information about specific features of sensory stimuli or the animal's behavioral state. Our study specifically focused on simple unstructured stimuli to identify the dominant spatiotemporal patterns evoked by them. The waves that we have identified are likely mediated by volleys of synaptic potentials (Bringuier et al., 1999), which modulate excitability of individual neurons. It is likely that the specific features of the stimulus are encoded by specific subpopulation of neurons that are phase locked to these waves. Processing of visual stimuli is known to involve activity of neurons broadly distributed across the visual system. Thus, while future work should address the relationship between stimulus features and the specific neuronal populations modulated by the travelling wave, our results show how such distributed neuronal assemblies can be coordinated by a wave that percolates across the visual system.

Traditional theories of sensory processing treat cortical neurons as independent feature detectors. This theoretical framework has been tremendously successful in predicting responses of individual neurons to stereotypical visual stimuli presented in isolation. However, models that treat neurons as independent feature detectors account for just a small fraction of activity in naturalistic settings (Olshausen and Field, 2005), indicating that spatiotemporal interactions between neurons are critical for effective visual processing. Recently, features of traveling waves

32

have been associated with prioritization of neuronal responses in the new eye position after a saccade (Zanos et al., 2015), and detecting weak sensory stimuli (Davis et al., 2020). Our results add to this burgeoning evidence by showing that simple unstructured stimuli elicit waves of activity that percolate across space and time in a highly stereotyped fashion and entrain firing of neurons in distant cortical regions. Thus, instead of treating individual neurons as quasi–independent feature detectors, new theories of sensory processing should consider patterns of neuronal activity arising during interactions with a natural world as a superposition of waves.

Methods

Animals: All experiments in this study were approved by Institutional Animal Care and Use Committee at the University of Pennsylvania and were conducted in accordance with the National Institutes of Health guidelines. All experiments were performed using 8 male and 6 female adult (12–32 weeks old, 20–30 g) C57BL/6 mice (Jackson Laboratories). Mice were housed under a reverse 12:12 h, light: dark cycle, and were provided with food and water ad libitum. A total of 20 mice were used in this study. Inclusion criteria for mice included the following: 1) presence of visual-evoked potentials (as defined by the absolute value of the average LFP response exceeding 5 standard deviations of pre-stimulus data within 100 ms after stimulus presentation) 2) histological verification of depth recording sites. With this inclusion criteria, we present data from 13 mice.

Headplate implantation and habituation: At least 2 weeks before recording, mice were chronically implanted with custom designed headpieces for head-fixation during awake recordings using standard methodology. Briefly, mice were anesthetized with 2.5% and maintained at 1.5% isoflurane in oxygen, and secured a stereotaxic frame (Narishige). Local anesthesia (0.25 ml of 0.625 mg bupivacaine) and antiseptic (Betadine) were applied. Periosteum was exposed and additional local anesthetic (0.25 ml of 2% Lidocaine gel) was applied. Bregma and lambda as well as the site of the future craniotomy (+1mm to -5 mm AP, +0.25 mm to +6 mm ML left of bregma)

were marked. The exposed skull was scored and the headpiece was attached using dental cement (Metabond) and 3 skull screws. Cyanoacrylate adhesive (Loctite 495) was applied over any remaining exposed skull. Mice were given 0.5mg cefazolin and 0.125mg meloxicam, and 7 ml of normal saline SQ after surgery. Animals were left to recover for a week before starting the habituation protocol. Mice were habituated to head fixation with body restraint with visual stimuli gradually over the course of 4 days. By the end of day 4, mice tolerated awake head fixation and visual stimuli for 45 minutes uninterrupted without any apparent distress.

Craniotomy: On the day of the experiment, animals were anesthetized with 2.5% isoflurane in oxygen, and maintained at 1.5% isoflurane with closed loop temperature control (37+/- 0.5 degrees C) for the remainder of the surgery. 0.625 mg bupivacaine was injected in the surrounding face and neck muscles in order to provide scalp anesthesia. Mice were also given 0.5mg cefazolin and 0.125mg meloxicam, 0.006 mg dexamethasone and 7 ml of normal saline SQ, before surgery. Craniotomy was drilled through the dental cement over the markings on the left hemisphere (+1mm to -5 mm AP, +0.25 mm to +6 mm ML of bregma). One of the securing screws on the right skull bone was chosen as the reference. A 64-electrode surface grid (E64-500-20-60, Neuronexus) was positioned over the dura (most medial and anterior electrode was positioned ~ 1mm lateral and 1mm posterior to bregma). Two laminar 32 channel probes (H4, Cambridge Neurotech) were coated with DiI (Sigma-Aldrich) for post mortem histological localization. The probes were inserted through the hole in the ECoG grid closest to V1 (-3.25 AP, -2.25 ML) and PPA (-1.5 AP, -1.5 ML) using a motorized micromanipulator (NewScale Technologies). Electrodes were inserted 800 µm into the brain at a rate of 25 µm/min. V1 electrode position was verified with current source density analysis. The grid and exposed dura was then covered with gel foam soaked in mineral oil. Isoflurane was then turned off for at least 20 minutes. At the end of this period and prior to recordings, animals were whisking, moving limbs and blinking in a manner similar to habituation before recordings began, thus suggesting that they were awake. This was corroborated by online analysis of the ECoG. After visual

stimulation and recording, animals were deeply anesthetized (5% isoflurane) and sacrificed. Brains were extracted and fixed in 4% paraformaldehyde (PFA) overnight prior to sectioning and histology.

Histology: Brains was sectioned at 80μm on a vibratome (Leica Microsystems). Sections were mounted with medium containing a DAPI counterstain (Vector Laboratories). Electrodes were localized using epifluorescence microscopy (Olympus BX41) at 4x magnification.

Visual Stimulation: Visual stimuli consisted of a 10 ms flash of a green LED (650 cd/m^2) separated by random intertrial intervals sampled from a uniform distribution between 3 and 4 seconds. The flash covered 100% of the mouse's visual field. In a subset of animals, visual stimulation was performed using a CRT monitor (Dell M770, refresh rate 60Hz, maximum luminance 75 cd/m2, positioned 23 cm away from the mouse's right eye, at an angle of 60% from the mouse's nose, thereby covering 70% of the mouse's right field of view) at varying luminance (2%, 11% 44%, 75%, 100% of maximum screen luminance). Flashes were 100ms long and presented in a random order at a random time interval between 3 and 5 seconds.

Electrode registration: After identifying the histological location of the two depth probes in each mouse, and with prior knowledge of the ECoG grid dimensions (i.e., 6 columns, 11 electrode rows, electrode spacing of 500μm, electrode diameter of 60μm, hole diameter of 200μm,), the position of each ECoG electrode was triangulated in the following fashion. The ECoG grid is a semiflexible plane. The location of the cortical probes in the electrode coordinate system was given by the through holes used for electrode insertion. The stereotaxic coordinates of the electrodes were established using post-mortem histology by comparison to the brain atlas (Paxinos). The cosine of the angle, θ between the laminar probe positions in the electrode and stereotaxic coordinates was computed. Each electrode on the ECoG grid was assigned a location based on the Euclidean distance from the two laminar probe sites. The resultant grid location

matrix was then multiplied to a rotation matrix (R) to obtain the final electrode positions in stereotaxic coordinates.

$$R = \begin{bmatrix} cos\theta & -sin\theta \\ sin\theta & cos\theta \end{bmatrix}$$

These coordinates were then verified by comparison to photographs of grid positions taken during experimental session.

Electrophysiology and preprocessing: Signals were amplified and digitized on an Intan headstage (Intan, RHD2132) connected to an Omniplex acquisition system (Plexon, Omniplex), and streamed to disk at 40KHz/channel.

To extract LFP, data were downsampled to 1KHz and filtered offline using a custom-built FIR filter between 0.1Hz and 325Hz, with the MATLAB functions, *firls.m* and *filtfilt.m* to minimize phase distortion. Noise channels were manually removed and trials with excess motion artifact were rejected. Subsequently, the ECoG signals were mean re-referenced to minimize the effect of volume conduction. All further analysis was performed using custom built Matlab (Mathworks) code unless otherwise stated.

Selection of electrode over Primary Visual Cortex (V1): To average over animals, a single stereotaxic V1 location was selected as the electrode closest to (-3.25 AP, -2.25 ML), and in each animal. To confirm that the chosen electrode neurophysiologically corresponded to V1, the latency of onset of the VEP at each grid electrode was computed. The latency of onset of the visual-evoked potential was calculated as the time point at which if their post-stimulus average exceeds 3 standard deviations above the pre-stimulus baseline for 3 consecutive time points. The stereotaxically labeled V1 electrodes were 1-2 electrodes away from the electrodes with the earliest latency of onset in all mice and had latencies of onset within 2 ms of the electrodes with the earliest latency of onset.

Current Source Density Analysis (CSD): The one-dimensional CSD was computed as the second

spatial derivative of the LFP recorded from the linear probes (Freeman and Nicholson, 1974):

$$\frac{d^2\varphi}{dz^2} = \frac{-[\varphi(z + 2\Delta z) - 2\varphi(z) + \varphi(z - 2\Delta z)]}{(2\Delta z)^2}$$

where φ is the LFP, z is the vertical coordinate depth of the probe, and Δz is the

interelectrode distance (25 µm). CSD at the electrode boundaries were obtained using estimation

procedure in (Vaknin et al., 1988). Cortical layers in the V1 probe were identified by the pattern of

visual evoked current sinks and sources (colored as blue and red, respectively). Channels with

the earliest current sink were assigned as layer 4 (granular layer). Subsequent sinks were found

above and below layer 4 in layers 2/3 and layer 5. Laminar assignment of the channels in the

PPA probe were based on distance from the cortical surface, where the CSD converged to zero.

Channels within the first 350 µm were defined as superficial layers based on the thickness of

layers 1-4 of the PPA (Franklin, Keith, B. and Paxinos, 2007; Lein et al., 2007a; Reference Atlas ::

Allen Brain Atlas: Mouse Brain). The next 400 µm were defined as deep layers. All further

analysis of laminar LFP data was performed on the CSDs. V1 probe data was included only if

there was a clear layer 4 sink and subsequent layer 2/3 and layer 5 sinks. Similarly, PPA probe

data was included in analysis only if the superficial loss of CSD was seen, indicating that the most

superficial electrode was positioned at the cortical surface. 11 mice fulfilled these criteria and

were included in the analysis of laminar recordings.

Spike Sorting

Single unit identification was performed on probe data from the same 11 mice that fulfilled criteria

for laminar analysis. Spike sorting was performed using Kilosort (Pachitariu et al., 2016). The

resulting spikes were then manually inspected for correct waveform clustering using Phy. All units

with a firing rate lower than 0.5 spikes/s were excluded from further analysis.

Wavelet analysis: Power, phase, and frequency information was extracted using a continuous

wavelet transform using Morlet wavelets (0.1Hz to 150Hz, with a step-width 0.25Hz and

normalized amplitude) (available at: http://paos.colorado.edu/research/wavelets/) (Torrence and Compo, 1998).

Inter-trial Phase Coherence (ITPC) Analysis: Inter-trial phase coherence (ITPC) was used to quantify the phase synchrony between trials at each point in the time- frequency plot. ITPC was calculated for each electrode in each mouse. Briefly, angle vectors were extracted from the wavelet coefficients at each time point and each frequency by applying Euler's formula and setting the single trial vector length to 1. ITPC was then calculated by taking the mean length of the angle vector across trials (Cohen, Mike, 2014).

ITPC values over the grid in Figure 2.2 were computed by averaging the ITPC over the first 100ms of the signal and over the frequency bands between 30-50Hz, or over the first 800ms of the signal and over the frequency bands between 3-6Hz

Filtering data: LFP or CSD data was filtered into high (30-50Hz) or low (3-6Hz) frequency bands in order to perform phase based analysis. Data was filtered using the inverse wavelet transform, *invcwt.m*, (available at: http://paos.colorado.edu/research/wavelets/) (Torrence and Compo, 1998), by setting all wavelet coefficients outside the desired frequency range to zero.

Analytical Signal Extraction: Hilbert transform was used to derive the analytical signal of LFPs or CSDs filtered in the gamma (30-50Hz) and low frequency (3-6Hz) data. This produced a time series of complex numbers. The modulus of the analytical signal is the instantaneous amplitude while the instantaneous phase is given by its arctan.

Complex Singular Value Decomposition (SVD): LFP recorded during a single trial and filtered at the appropriate frequency range (see above) using the Hilbert transform to derive an

$n \times t$ analytical signal matrix $\boldsymbol{A}$, where n is the number of electrodes and t is the number of time points. Spatiotemporal modes were extracted from $\boldsymbol{A}$ by performing singular value decomposition which factorizes A into mutually orthogonal modes:

$$\mathbf{A} = \mathbf{USV^T}$$

The columns of complex-valued U and V are the left and right singular vectors, which encode the spatial and temporal components of each mode, respectively. The diagonal real-valued S contains singular values ($\lambda's$). The fraction of the total signal explained by $i - th$ mode is given by

$$\lambda_i / \sum_1^n (\lambda)$$

The spatial distribution of each mode is computed as $w_s = |U_{(*,i)}| * \lambda_i$. Each of the n components of w_s reflects the contribution of each electrode to the mode. The spatial phase is defined by $\theta_s = \arctan U_{(*,i)}$. Similarly, each component of θ_s reflects the spatial phase of each electrode. Temporal phase θ_t and amplitude w_t are defined in a similar fashion from $\mathbf{V}$, $\theta_t = \arctan V_{(i,*)}$ and $w_t = |V_{(i,*)}| * \lambda_i$. The spatial phase gradient of each mode $\frac{d\theta_s}{ds}$ can then be computed locally at each electrode as in (Muller et al., 2014) (see below). The temporal frequency is given by the time derivative of the unwrapped temporal phase $\frac{d\theta_t}{dt}$ normalized by 2π. The analytical signal corresponding to mode i can be reconstructed as $A^i = U_{(*,i)} * \lambda_i * V_{(i,*)}^T$. Finally, the LFP signals corresponding to each mode can be reconstructed as $LFP^i = |A^i| * cos(\arctan(A^i))$. Illustration of this procedure is shown in Figure 2.4.

Defining the most visually responsive mode: The first ten singular modes (accounting for 62.34 % - 81.18% variance, 95% confidence interval) computed for each single trial, as above. w_t is defined as the temporal amplitude for the first ten modes. w_t during the pre-stimulus period (400 ms) and was then used to compute the mean, $\langle w_t \rangle$ and the standard deviation, σ_{w_t}. w_t for the entire trial period (pre- and post-stimulus) was expressed as a z-score $w_z = (w_t - \langle w_t \rangle)/\sigma_{w_t}$. The most visually responsive mode was defined as the mode that exhibited the greatest increase in amplitude during the post-stimulus period (defined as 350ms post-stimulus for fast oscillations and 1000ms post-stimulus for slow oscillations).

Spatial phase offset from V1: To determine the consistency in the phase relationship between spatial modes identified in different trials and across animals, the average difference in phase from each channel to the V1 channel was computed for the most visually responsive spatial mode. The V1 channel in each animal is defined as the channel closest to (-3.25 AP, -2.25 ML). The phase offset from V1 is calculated at each electrode by extracting the spatial phase of the most visually responsive mode θ_s and setting the V1 phase to zero. Circular mean and variance of θ_s referenced to V1 was then computed across trials and across animals (Fisher, N, 1995). The direction of the resultant vector corresponded to the average phase, whereas the magnitude of the vector is 1-circular variance.

Spatial phase gradient: The spatial phase gradient was quantified by multiplying the complex spatial component of the most sensory evoked mode of a single trial at each electrode location to the complex conjugate of the spatial loading of its adjacent electrode, using continuous wavelet transform, *phase_gradient_complex_multiplication.m*, in MATLAB, written by Lyle Muller (available at: https://github.com/mullerlab/wave-matlab)(Muller et al., 2014). This operation was performed iteratively along the AP and ML direction of the grid. The resulting vectors were then converted into polar coordinates. To quantify the average gradient over trials, each trial's gradient vector at each location was projected on a unit circle and the angles were averaged as above. Now, the angle of the resultant average vector is the direction of the average phase progression, whereas magnitude is 1-variance of the gradient over trials.

Spatial Wavelength: The spatial frequency was computed by multiplying the magnitude of the single trial spatial gradient vectors and dividing the result by 2π to convert the units into cycles/mm. Spatial wavelength was calculated as the reciprocal of spatial frequency.

Velocity of visual evoked waves: The instantaneous temporal frequency was computed by measuring the slope of the unwrapped temporal phase of the most visually responsive mode. The

instantaneous frequency was then divided by the magnitude of the phase gradient of the most responsive spatial mode on a single trial basis.

Phase amplitude coupling: Phase-amplitude coupling between oscillations was assessed using the modulation index measure (MI) of single trial filtered LFP data at every grid electrode site. Phase of the 3-6Hz filtered data and the amplitude of the 30-50Hz filtered data were extracted from the analytical signal A as described above. Phase was binned into 20 phase intervals. The mean 30-50Hz amplitude was calculated for each bin for the first 900 ms of post stimulus activity per trial. The mean amplitude per bin was then averaged over trials. The MI was calculated by measuring the divergence of the resulting amplitude distribution from the uniform distribution using a modified Kullback–Leibler (KL) distance metric, with the function, *ModIndex_v2.m*, (available at https://github.com/tortlab/phase-amplitude-coupling) (Tort et al., 2010).

Spike Field Coherence (SFC)

The phase 3-6 Hz filtered CSD was extracted from the analytical signal and segmented into 20 bins. The mean spike count was calculated for each bin for the first 900 ms of post stimulus activity per trial, and then averaged over trials. The MI was calculated by measuring the MI in a similar manner to calculating phase amplitude coupling.

Averaging signals over stereotaxic coordinates: A query grid of stereotaxic locations was defined spanning -3.5 to 0 mm ML and -5 to 0 mm AP with 0.5mm spacing. For each query location, the weight of each electrode was assumed to depend on the distance between the electrode and the query location. The weights were defined to be a Gaussian function of Euclidian distance from the query location as follows:

$$W = \frac{1}{\sigma\sqrt{2\pi}} e^{\frac{||p_q||}{\sigma}}$$

where $\left\|p_q\right\|$ is the Euclidean distance between the electrode p and query location q, $\sigma = 0.15$ is the standard deviation. The weight was computed as in the above equation for all electrodes within 0.3 mm of the query location and was set to zero otherwise. This weighting was used when computing averages and variances across mice as a function of stereotaxic coordinates.

Spike Correlations: For each entrained V1 and PPA neuron in each animal, the delay of the spike times of the V1 cells relative to the spike times of PPA cells was computed during the pre-stimulus timeframe (500 ms before the stimulus onset), and post-stimulus time frame (0-500ms after stimulus onset). The distribution of spike time delays were then displayed in Figure 2.13.

Statistical Analysis: To establish statistically significance of ITPC and phase coupling at each query location, the observed ITPC, MI values, and spike field coherence values were compared to a series of random time shifted surrogates (n = 100 sets, 100 trials per set). To determine the aggregate p-value over mice at each stereotaxic location, a Stouffer's Z-score was calculated.

To determine if the phase relationships between each stereotaxic location and V1 and spatial gradient show a statistically significant deviation from a uniform distribution on a circle, a Rayleigh test was performed on a mouse by mouse basis and for the aggregate data. P-values were Bonferroni corrected for multiple comparisons, unless otherwise stated.

To determine the statistical significance of SFC measures, the MI for SFC was compared to an MI distribution obtained using surrogate spiking data generated by using a Poisson process at each time point, using a student's t-test. The Poisson firing rate was determined by calculating the firing rate of each unit in a 200ms sliding window shifted by 1ms.

a Awake ECoG LFP

b
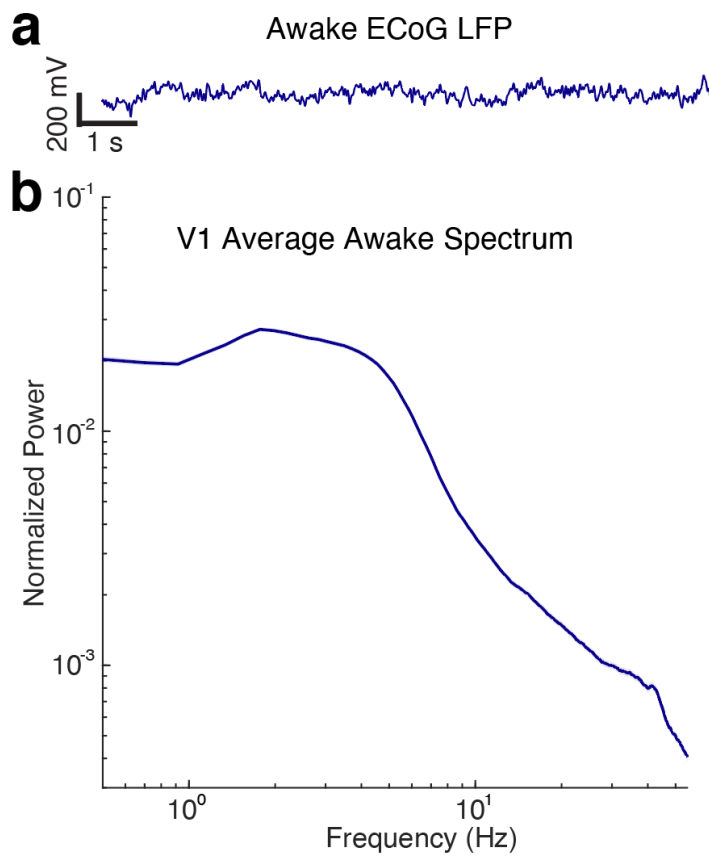
Figure 2.1: Awake LFP and Power spectrum

(A) Spontaneous LFP recorded over V1 in a representative awake mouse. Note the
dominance of high frequency, low amplitude activity

(B) Power spectrum of V1 LFP averaged over animals.
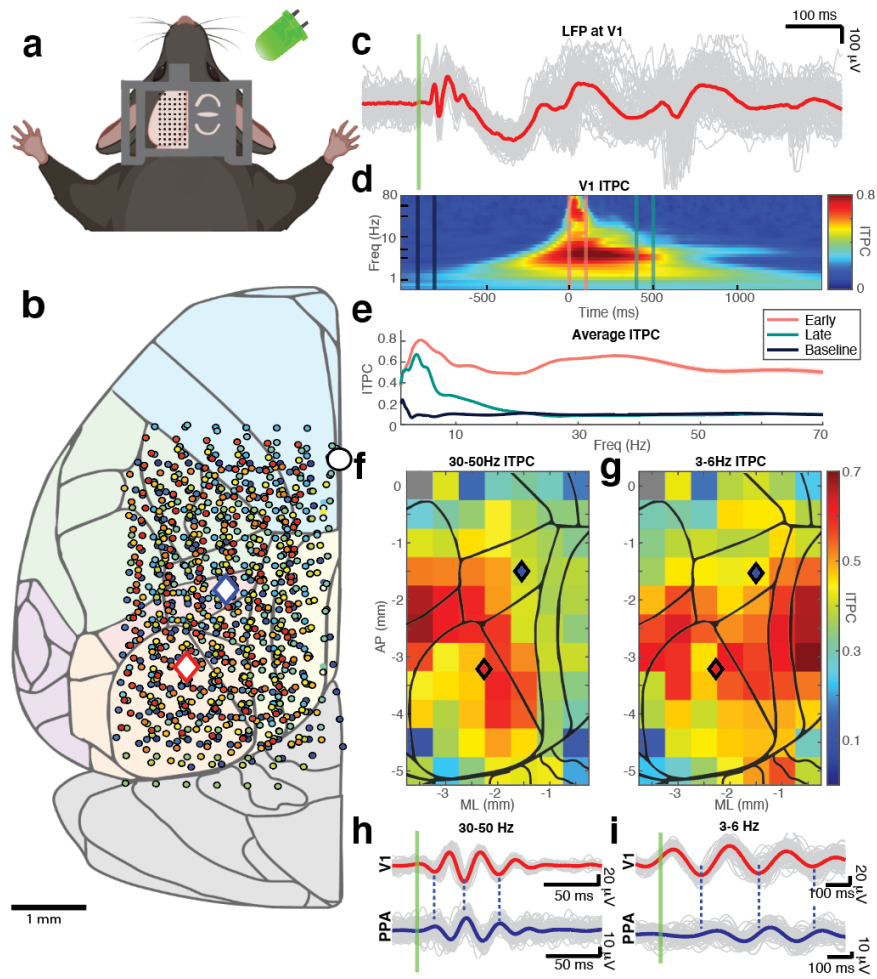
Figure 2.2: Visual stimuli elicit strong intertrial phase coherence over large cortical areas

(A) Schematic showing the 64 channel electrocorticography (ECoG) grid used to record local field potentials (LFPs) from the cortical surface of the left hemisphere of 13 awake mice. Stimuli consisted of 10 ms flashes of a green LED placed in front of the R eye (100 trials, intertrial interval 3-4s).

(B) Stereotaxic coordinates of ECoG electrodes from 13 animals (color coded by animal). V1 and PPA targets for laminar probes are shown by red and blue diamond respectively. The white circle marks bregma. The cortical surface is shaded by area according to the Allen Brain Atlas (Franklin, Keith, B. and Paxinos, 2007; Lein et al., 2007a; Reference

44

Atlas :: Allen Brain Atlas: Mouse Brain): visual (orange), association (red), retrosplenial (yellow), somatosensory (green), motor/frontal (blue), and cerebellum (gray).

(C) Single trial and average visual evoked potentials (VEPs) over V1 are indicated by gray and red lines respectively. Stimulus onset is denoted by the green line.

(D) Inter-trial phase coherence (ITPC) computed at V1 and averaged over single trials and animals (0 ms marks stimulus onset).

(E) Time slices through the coherogram (Figure 1D). Colors of the traces correspond to time segments shown in D. Thick line shows the average. Shaded areas show 95% confidence intervals.

(F) Average ITPC of 30-50Hz oscillations within the first 100 ms of the VEP averaged over animals at each stereotaxic location. Locations in which ITPC does not meet Bonferroni corrected statistical significance compared to time shuffled surrogate data are shaded in gray.

(G) Similar to E for average ITPC of 3-6Hz activity within the first over 800 ms of the VEP.

(H) Top: VEPs recorded over V1 and filtered at fast (30-50 Hz) oscillations (gray and red show single trials and trial average respectively). Bottom: Same data recorded from over PPA (gray and blue show single trials and trial average). Green line shows stimulus onset. Dashed lines highlight the phase offset between V1 and PPA.

(I) Similar to G except the signals are filtered at 3-6Hz. Slower (3-6Hz) oscillations also show a phase shift between V1 and the PPA.

*Data in C, H, and I are from a single representative mouse.
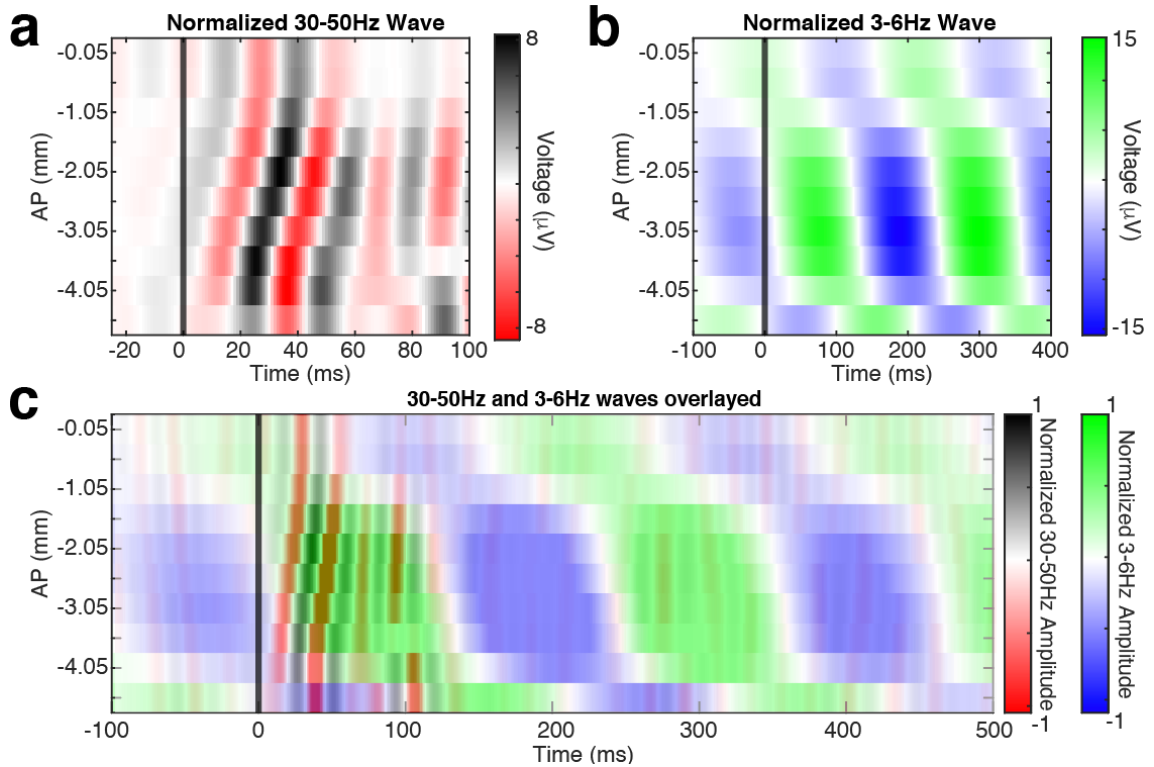
Figure 2.3: Average filtered LFP illustrate traveling wave-like behavior.

(A) Average of the VEP filtered at 30-50Hz from 10 electrodes along the anterior to posterior axis (-2.25mm ML) in a representative mouse. The x axis denotes time relative to stimulus onset, the y axis indicates AP position of an electrode relative to bregma. Note evoked high frequency waves starting at -4.05mm from bregma (V1) and traveling anteriorly over ~100ms.

(B) Average of the VEP filtered at 3-6Hz from the same mouse arranged in the same format at B. Note the low frequency waves begin more anteriorly (~2 mm from bregma) relative to the fast oscillations and travel in the posterior direction.

(C) Superimposition of the data in A-B (amplitude of the signals is normalized to highlight phase relationships between oscillations at different temporal frequencies). The fast wave begins posterior to the slow wave and travels rostrally towards the slow wave initiation zone.

46

a Modelled Data

Channels
1
2
3
4
5
6

1 mV
100 ms

Hilbert Transform →

b Analytical Signal

Imaginary
2
1
0
-1
-2
-3

Real 0

2

-2

200 400 600
Time (ms)

U•S•V' = SVD(Analytical Signal)

c Singular Values

% Variance
60
40
20

1 2 3 4 5 6
SVD Rank

d |U•S|: Amplitude of Spatial Mode

Channels
1
2
3
4
5
6

Spatial Amplitude

e |S•Vᵀ|: Amplitude of Temporal Modes

1 mV

100 ms

f tan⁻¹(U•S): Spatial Phases

Mode 1

π/2

dθ/dspace

π   0

3π/2

Mode 2

π/2

π   0

3π/2

g tan⁻¹(S•Vᵀ): Temporal Phases

Instantanous Phase

π

100 ms

→

Unwrapped Phaes

Phase
0

dθ/dt

-60

0 200 400 600
Time (ms)

h U • S • Vᵀ: Reconstructed Modes

Mode 1

Channels
1
2
3
4
5
6

200 400 600
Time (ms)

Amplitude (mV)
1.5
1
0.5
0
-0.5
-1
-1.5

Mode 2

Channels
1
2
3
4
5
6

200 400 600
Time (ms)

Amplitude (mV)
2
1.5
1
0.5
0
-0.5
-1
-1.5

47

Figure 2.4: Singular value decomposition (SVD) of the analytical signal data identifies coherent spatiotemporal activity modes.

(A) Modelled oscillatory activity for 6 electrodes. The signals in the first five electrodes record a traveling wave that propagates from electrode 5 to 1 (black through orange) The sixth electrode (red), is constructed to be independent from others. The green vertical line denotes the stimulus.

(B) Analytical (complex valued) signal is obtained using the Hilbert transform from data in A. In the complex plane, the travelling wave appears as phase shifted copies of the same signal and the divergent activity of the sixth electrode is distinct.

(C) Singular value decomposition (SVD) can be used to parse the analytical signal into mutually orthogonal modes. Real valued diagonal matrix S encodes the relative contribution of each mode to the overall activity pattern. Complex-valued U and V matrices encode the spatial and temporal characteristics of each mode respectively. SVD identifies only two modes with nonzero singular values, corresponding to the two oscillatory patterns within the signal.

(D) The columns of matrix |U*S| encode the spatial amplitude of each mode, and measures how much each electrode contributes to each of the temporal modes. SVD correctly identifies that the first 5 electrodes contribute to the first mode (the traveling wave) equally, whereas mode 2 exclusively involves electrode 6.

(E) The temporal amplitudes, computed as |S*VT|, reveal the envelope of each mode. Visually responsive modes were defined as modes that increase in temporal amplitude after the stimulus. In this example, only the first mode is visually responsive.

(F) The spatial phases are calculated as arctangent of U scaled by the corresponding singular value. The spatial frequency is computed from the phase gradient ($d\theta/ds = F_s$). Here, the phase map of the first mode illustrates that the first five electrodes contribute (black through orange) equally and have a constant phase offset from one another,

whereas the sixth electrode (red) has a smaller magnitude. In the second mode, only the sixth electrode has a large magnitude.

(G) The temporal phases are calculated as arctan of VT. The time derivative of this phase $(d\theta/dt = F_t)$ defines the temporal frequency of the mode and is approximated by measuring the slope of the unwrapped temporal phase. The propagation velocity of the mode is then computed as F_t/F_s.

(H) The activity corresponding to the i-th spatiotemporal mode can be reconstructed as $U_{:,i} *$ $S_{i,i} * V_{i,:}^T$. Here, the first mode shows a traveling wave in the first 5 electrodes. The independent spatiotemporal mode in the sixth electrode is present in the second mode.
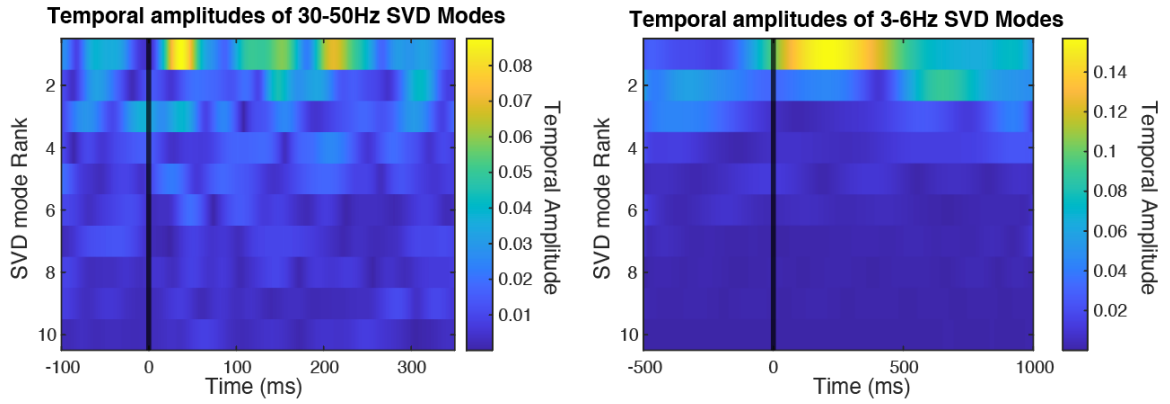
Figure 2.5: The first mode extracted from SVD typically has the highest post-stimulus temporal amplitude

Temporal amplitude of each of the first 10 SVD modes of a single trial filtered at 30-50Hz (right) or 3-6Hz (left), by time in ms. The stimulus occurs at the black line. Note in both frequency bands, the first mode has the largest increase in amplitude following the stimulus and is therefore defined as the most responsive visual mode.

(D)
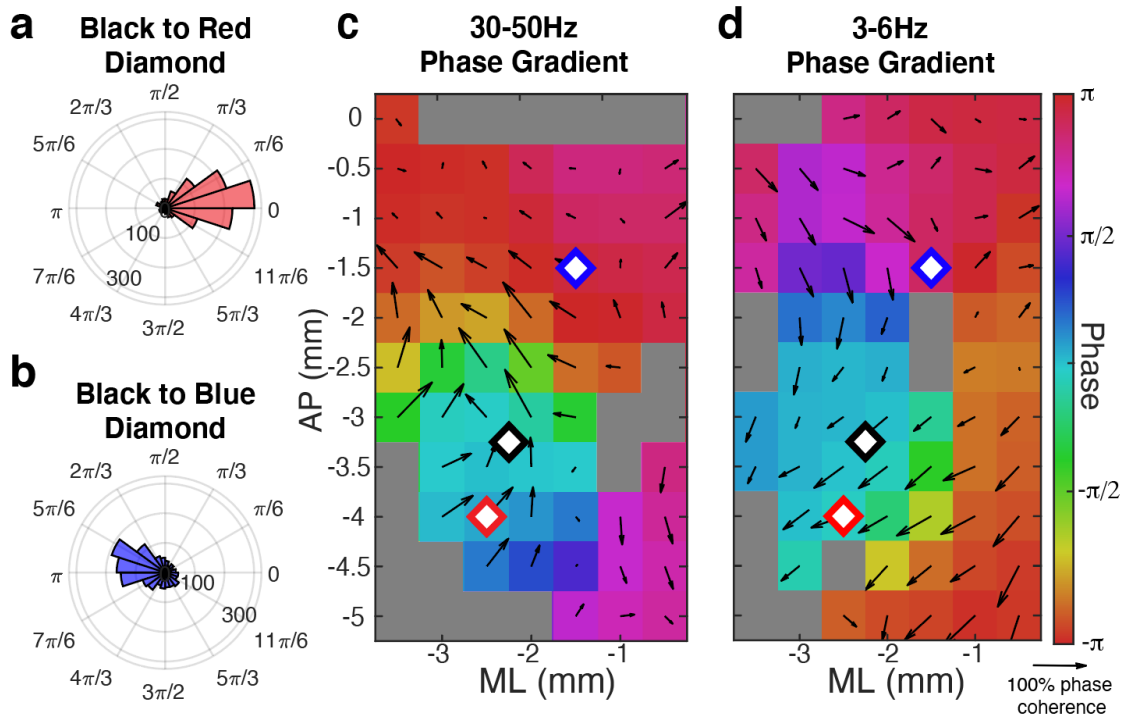
Figure 2.6: SVD identifies visual evoked traveling waves that are consistently elicited both across trials and across animals.

(A) Histogram of the difference in the spatial phase of the most visually responsive 30-50 Hz mode between two electrodes in V1 (black and red diamonds in C) across trials and animals.

(B) Histogram of phase angle difference of the most visually responsive 30-50 Hz mode between an electrode in V1 (black diamond in plot C) and PPA (blue diamond in plot C) across trials and animals. Note that the phase angle difference is increased as distance from V1 increases.

(C) At each stereotaxic location, the average phase offset of the 30-50Hz spatial mode relative to V1 (the black diamond) is plotted in color. Spatial phase gradient is depicted by black arrows. The direction of the arrows shows the direction of spatial phase gradient over trials and mice. The length of the arrows is 1- circular variance and therefore corresponds to the consistency of the angle of the spatial phase gradient over trials and

animals (scale arrow for 100% phase coherence underneath color axis in D). Locations

that are greyed out did not meet Bonferroni corrected statistical significance (p-value <

0.0006, Raleigh test).

(D) Phase offset relative to V1 and the spatial phase gradient of the most visually responsive

3-6Hz spatial mode at each stereotaxic location depicted as in D.
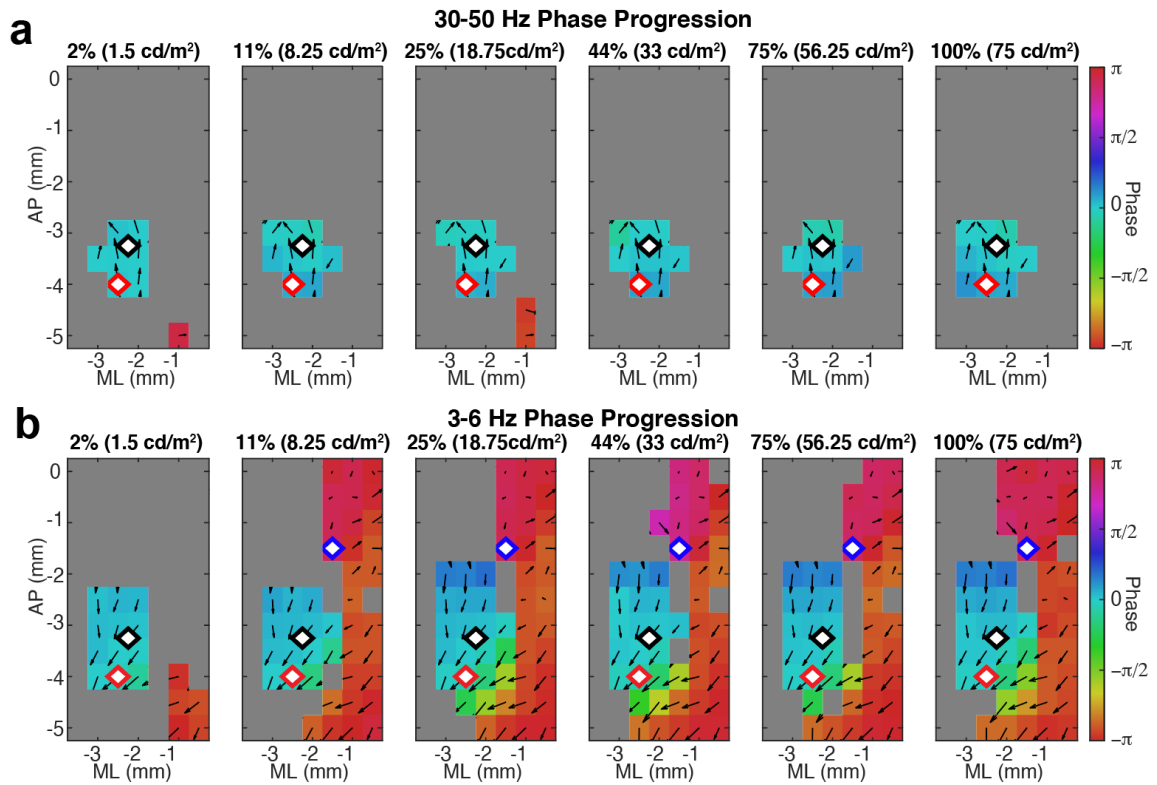
Figure 2.7: The consistency of the wave propagation pattern depends on stimulus intensity

(A) At each stereotaxic location, the average (over mice) phase offset of the 30-50Hz spatial mode relative to V1 (the black diamond) is plotted in color for each screen luminance, listed as a percent of maximum screen luminance. The red diamond is a different location in V1. Spatial phase gradient is depicted by black arrows. The direction of the arrows shows the direction of spatial phase gradient over trials and mice. The magnitude of the arrows corresponds to the consistency of the angle of the spatial phase gradient over trials and animals. Locations that are grayed out did not meet Bonferroni corrected statistical significance (p-value < 0.0006) across animals.

(B) Same plots as in A but for waves identified from 3-6Hz filtered data. The blue diamond denotes the location of the PPA.
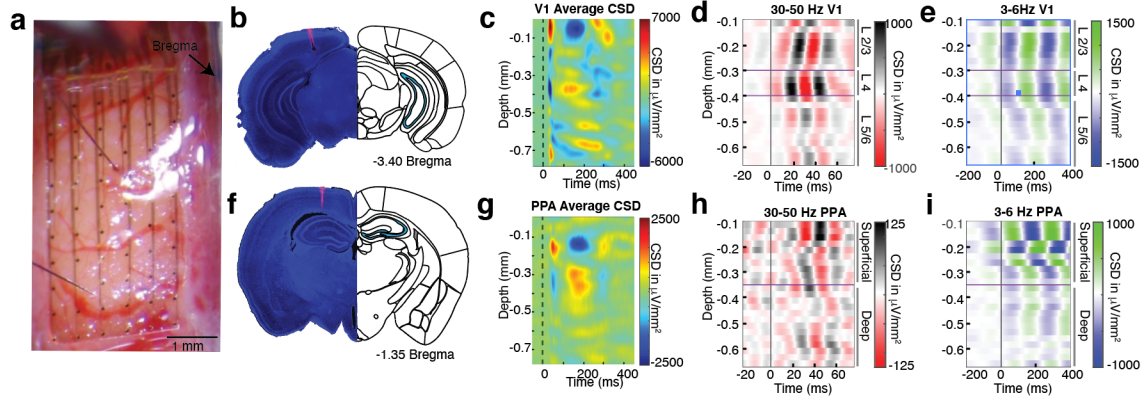
Figure 2.8: Intra-laminar recordings reveal vertical propagation pattern of waves

(A) Photograph of 64 channel electrocorticography grid with two 32 channel penetrating laminar probes placed in through holes in the grid into V1 and PPA.

(B) Histological verification of laminar electrode localization in V1.

(C) Current source density (CSD) in V1 averaged over trials and mice.

(D) V1 CSD filtered at 30-50Hz and averaged across trials in a representative mouse. 30-50Hz oscillations originate in layer IV and then propagate to superficial and deep cortical layers. In D and E purple lines show approximate location of layer IV defined by the earliest sink in the CSD.

(E) Same as D but filtered at 3-6Hz. The 3-6Hz oscillations appear approximately simultaneously in the supra- and granular layers and propagate to deeper layers.

(F) Histological verification of laminar electrode localization in PPA.

(G) CSD in PPA averaged over trials and mice. Purple lines show approximate location of superficial layers I-IV, and deep layers V/VI based on anatomy (Allen Brain Atlas).

(H) Same as D for PPA. The 30-50Hz oscillations are most prominent in the superficial layers.

(I) Same as E for PPA. The 3-6Hz oscillations begin in the superficial layers and propagate to deeper layers

*Data in D, E, H, I are from the same representative mouse.
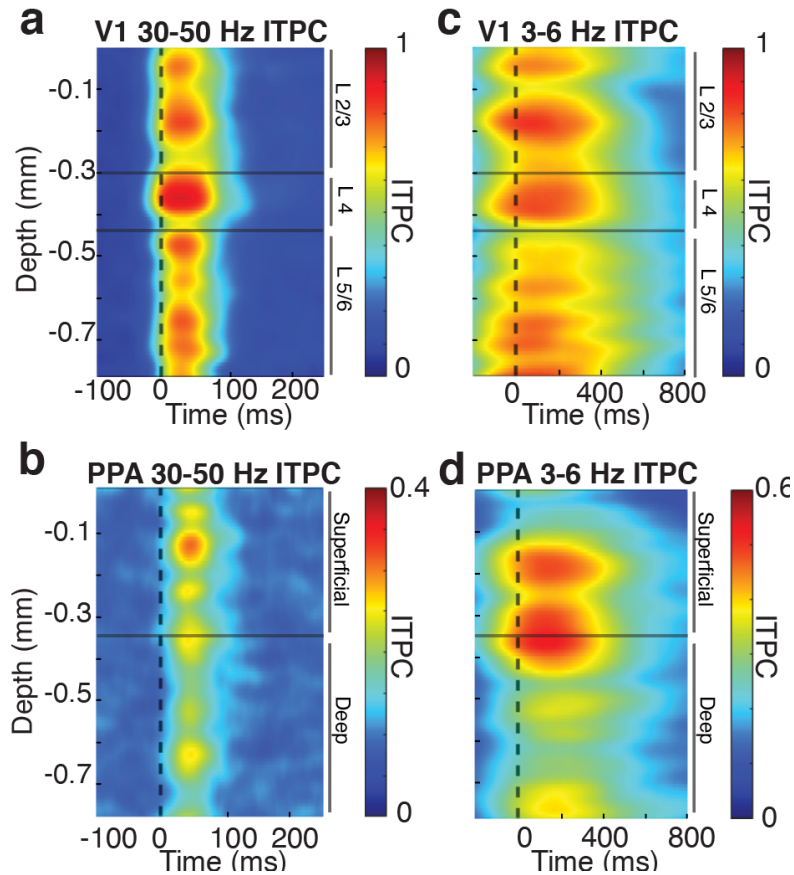
Figure 2.9: Superficial cortical layers of V1 and PPA contain high ITPC

(A) ITPC of CSD at 30-50Hz as a function of time and depth in V1, averaged over animals. The horizontal lines indicate the supra-, granular, and infragranular layers.

(B) Same plots as in A but for PPA. Note that high frequency ITPC is most prominent in superficial cortical layers.

(C) ITPC of CSD at 3-6Hz as a function of time and depth in V1, averaged over animals. The horizontal lines indicate the superficial and deep layers.

(D) Same plots as C but for PPA. In contrast to V1, ITPC is most dominant in the superficial layers.
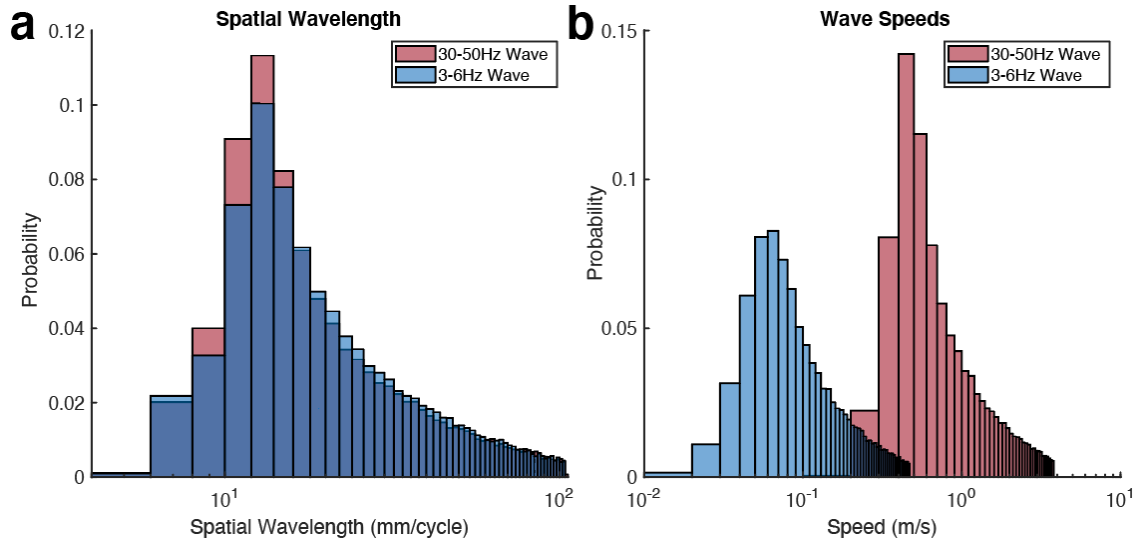
Figure 2.10: Fast and slow visual evoked waves have similar spatial wavelengths but significantly different propagation velocities

(A) Distribution of spatial wavelengths of 30-50Hz and 3-6Hz most visually responsive modes.

(B) Distribution of wave speeds of most visually responsive modes at 30-50Hz and 3-6Hz.

56
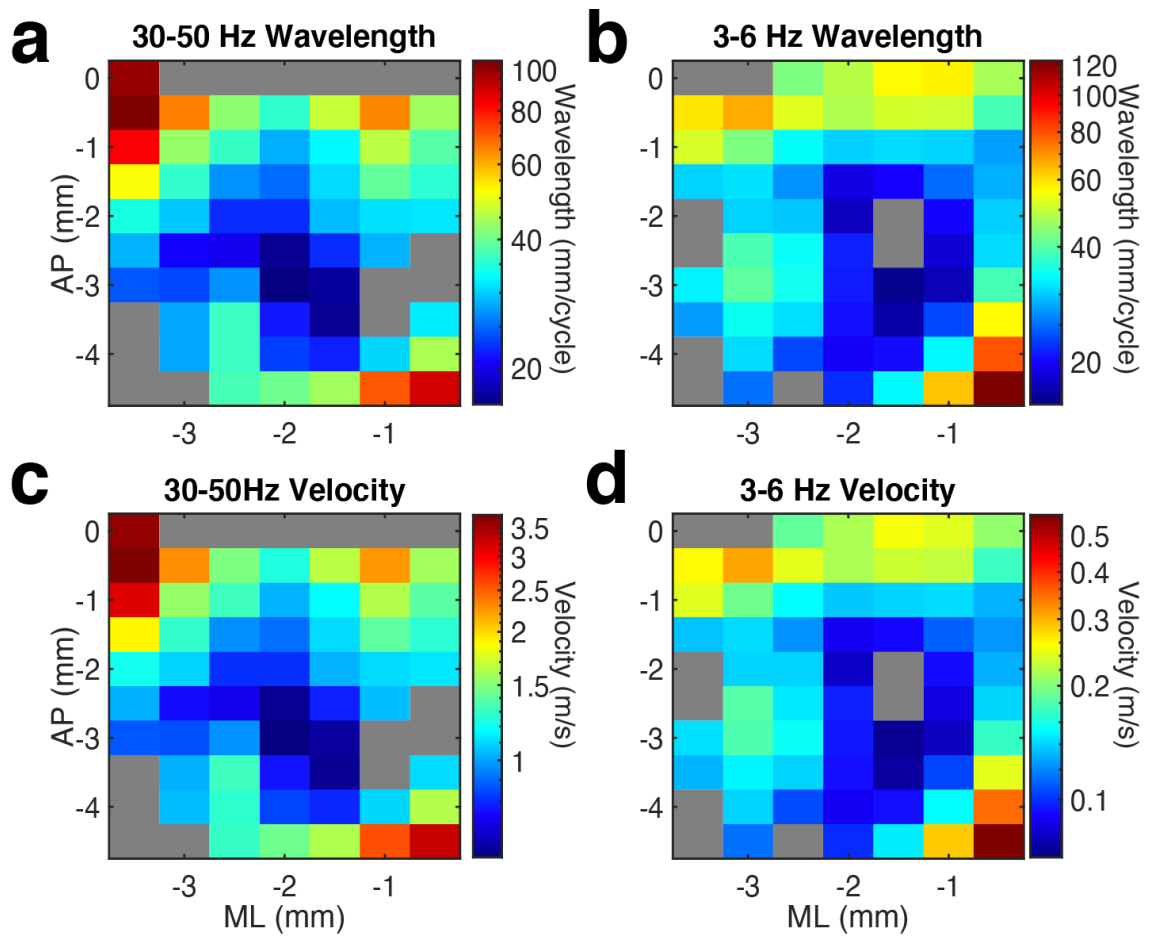
Figure 2.11: Spatial wavelength and wave velocity are not uniform over space

(A) Spatial wavelength of fast 30-50Hz most visually responsive SVD modes.

(B) Spatial wavelength of fast 30-50Hz most visually responsive SVD modes.

(C) Velocity of fast 30-50Hz most visually responsive SVD modes.

(D) Velocity of fast 30-50Hz most visually responsive SVD modes.

*Note that in all plots, the color axis is in log scale and locations that are grayed out did not meet Bonferroni corrected statistical significance (p-value < 0.0006) across animals.
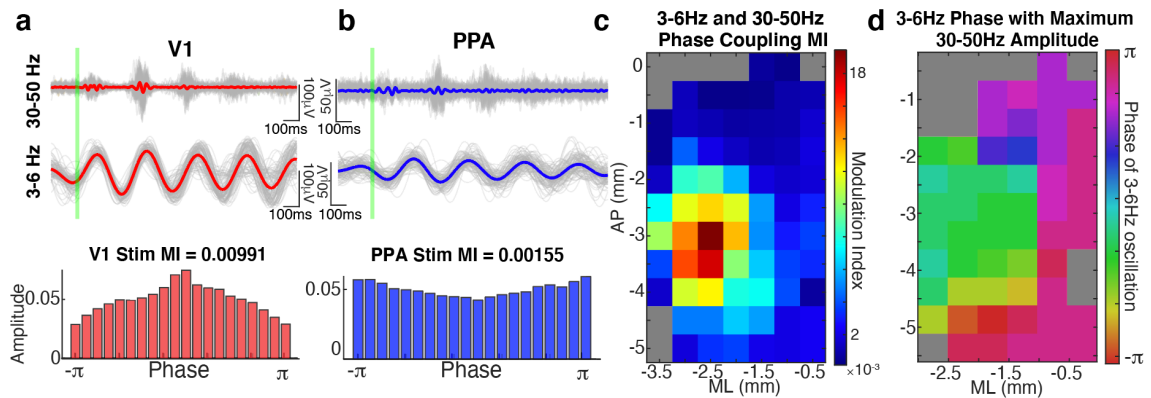
Figure 2.12: The phase of the slow wave modulates the amplitude of the fast wave both within V1 and throughout the cortex

(A) Top: single trials (gray) and average (red) data filtered at 30-50Hz over V1 of a representative mouse. Middle: same as above, but for 3-6Hz. Note fast oscillation bursts occur rhythmically in phase with slow oscillations. Bottom: Amplitude of high frequency oscillations at each phase of the low frequency oscillation, averaged over trials. The deviation of this distribution from a uniform distribution is summarized in the modulation index (MI) of 0.00991(p-value <0.0001, compared to time shuffled surrogates).

(B) Similar to A but for an electrode over PPA. The phase amplitude MI = 0.00155 (p-value <0.0001). Note that the phase of the 3-6Hz oscillation at which the gamma amplitude is maximum is shifted compared to that in V1.

(C) Modulation indices averaged over all 13 mice and plotted in color at each stereotaxic location. Locations that are greyed out did not meet Bonferroni corrected statistical significance (p-value < 0.0006) compared to time shifted surrogate data. MI peaks near V1 but remains statistically significant over much of the cortical surface.

(D) The phase of the slow 3-6Hz oscillation at which the fast 30-50Hz oscillation reaches maximum amplitude as shown for a representative mouse at each stereotaxic location. Grayed out locations did not meet statistical significance compared to time shifted surrogates.
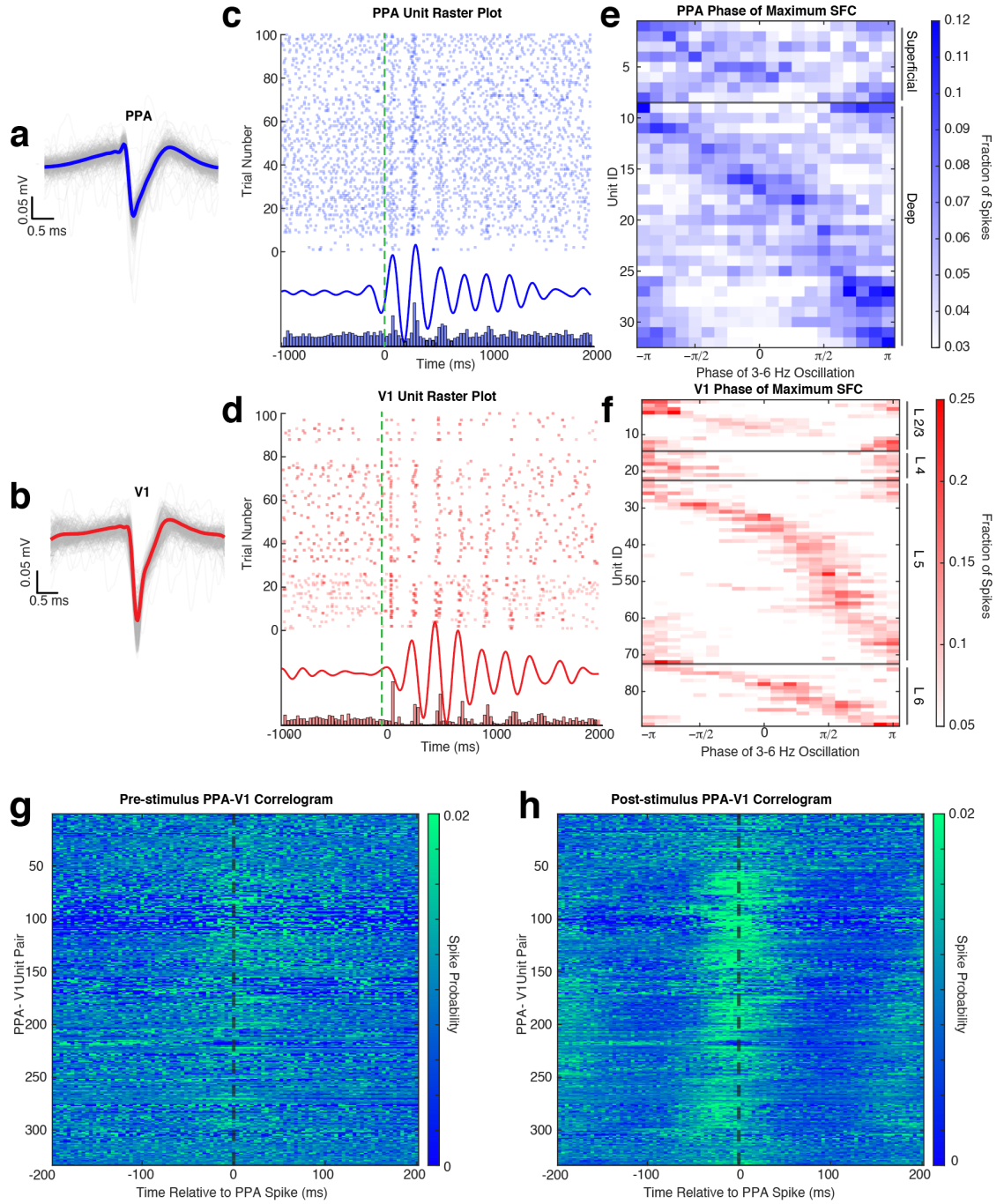
Figure 2.13: Probability of neural spiking in both V1 and PPA depend on the phase of the slow wave

(A) Individual action potential waveforms of a representative PPA unit located in layer V (gray traces), with the average waveform superimposed in blue.

(B) Same as A, but for a representative V1 neuron located in infragranular layers (gray traces), with the average waveform superimposed in red.

(C) Raster plot (top) of 100 trials of PPA unit (green dashed line marks stimulus onset). The average CSD, filtered at 3-6 Hz, of the LFP at the same depth as the unit in A (middle). The peristimulus histogram of the same unit (bottom).

(D) Same as C, but for the representative V1 unit in B.

(E) Probability of firing as a function of phase of the slow oscillation for each unit in the PPA. Each row is an individual unit in the PPA that has statistically significant spike field coherence (SFC) with the slow oscillation. Units above the black horizontal line are in the superficial layers of the PPA. Units below the black horizontal line are within the deep layers.

(F) Same as E for V1 units with statistically significant spike field coherence. The horizontal back lines highlight four sections in which V1 cells reside, in top-down order: layer II/II, layer IV, layer V, and layer VI.

(G) Cross-correlograms between PPA and V1 neurons entrained by the slow wave during the 500 ms before visual stimulation. Each row is an individual PPA V1 pair. Probability of firing is shown by color.

(H) Same as in G but for 500 ms after the stimulus.

*all videos can be found at
https://drive.google.com/drive/folders/18VYjQfhkuhRSGUww4RykrSeobuVt_BcY?usp=sharing

Video 2.1: Awake mouse

Three seconds of an awake mouse in recording both.

Video 2.2: Average visual evoked fast wave

Average of single trial LFP filtered at fast, 30-50Hz, frequencies over the cortical surface during

the first 100 ms of the visual evoked response. The flash occurs at time = 0 ms. Note that the

visual evoked gamma activity begins caudally within V1 and propagates rostrally.

Video 2.3: Average visual evoked slow wave

Average of single trial LFP filtered at slow, 3-6Hz, frequencies, over the cortical surface during

the first 600 ms of the visual evoked response. The flash occurs at time = 0 ms. Note that the

visual evoked gamma activity begins rostral to V1 in higher order cortical areas and propagates

caudally.

Video 2.4: Both visual evoked waves superimposed

Superimposition of the average fast and slow filtered waves (amplitude of the signals is

normalized to highlight temporal relationships between oscillations). The flash occurs at time = 0

ms. The fast wave begins caudal to the slow wave and travels anterolaterally towards the slow

wave initiation zone.

CHAPTER 3 - Coherence of visual-evoked gamma oscillations is disrupted by propofol but preserved under equipotent doses of isoflurane

Abstract

Previous research demonstrates that the underlying state of the brain influences how sensory stimuli are processed. Canonically, the state of the brain has been defined by quantifying the spectral characteristics of spontaneous fluctuations in local field potentials (LFP). Here, we utilized isoflurane and propofol anesthesia to parametrically alter the spectral state of the murine brain. With either drug, we produce slow wave activity, with low anesthetic doses, or burst suppression, with higher doses. We find that while spontaneous LFP oscillations were similar, the average visual-evoked potential (VEP) was always smaller in amplitude and shorter in duration under propofol than under comparable doses of isoflurane. This diminished average VEP results from increased trial-to-trial variability in VEPs under propofol. One feature of single trial VEPs that was consistent in all animals was visual-evoked gamma band oscillation (20-60Hz). This gamma band oscillation was coherent between trials in the early phase (<250 ms) of the visual evoked potential under isoflurane. Inter trial phase coherence (ITPC) of gamma oscillations was dramatically attenuated in the same propofol anesthetized mice despite similar spontaneous oscillations in the LFP. This suggests that while both anesthetics lead to loss of consciousness, elicit slow oscillations and burst suppression, only the isoflurane permits phase resetting of gamma oscillations by visual stimuli. These results demonstrate that accurate characterization of a brain state must include both spontaneous as well as stimulus-induced perturbations of brain activity.

Introduction

Anesthesia is a staple in modern healthcare due to its ability to provide a reversible state of unconsciousness, which is essential for painless surgery and for sedation in intensive care units (ICUs). Anesthetics have also proved indispensable for basic neuroscience. Indeed, much of our knowledge concerning sensory processing is derived from experiments performed in

anesthetized animals(Destexhe et al., 1999; Hubel and Wiesel, 1962; Mountcastle, 1957).

Despite their widespread use, the mechanisms by which anesthetics produce a reversible loss of

consciousness (LOC) remain unknown. One practical implication of this knowledge gap is that

clinical monitoring of the anesthetized state is unable to guarantee that all patients are, in fact,

unconscious during surgery. While depth of anesthesia monitors do ensure that majority of

anesthetized patients are unconscious, 4-10% of patients under general anesthesia exhibit a

covert return of consciousness as evidenced by their ability to follow simple verbal

commands(Mashour et al., 2011; Russell, 1989; Sanders et al., 2012; Schneider Gerhard et al.,

2005). Current EEG-based "depth of anesthesia" devices do not reliably detect these episodes of

awareness(Mashour, 2006; Sanders, 2016). While patients with covert awareness are less likely

to form memories(Mashour et al., 2011, 2012; Sanders et al., 2012), up to 70% of those that do,

develop long-lasting psychiatric consequences such as post-traumatic stress disorder

(PTSD)(Leslie et al., 2010).

General anesthetic agents are structurally heterogeneous and exhibit promiscuous binding

to a wide variety of molecular targets(Eckenhoff and Eckenhoff, 1998; Franks, 2008; Lydic Ralph

and Baghdoyan Helen A., 2005). It is highly unlikely that each anesthetic drug disrupts

consciousness using the same molecular effectors. Nevertheless, mechanistically distinct

anesthetics are known to generate similar patterns of brain activity. The most prevalent pattern of

brain activity observed in the anesthetized brain are the canonical slow oscillations first

demonstrated in human EEG in the 1930's(Gibbs, F., Gibbs, E., Lennox, 1937). For example,

propofol, a positive allosteric modulator at $GABA_A$ receptors(Jurd et al., 2003), induces low

frequency large amplitude EEG oscillations and sleep-like spindles(Ching et al., 2010; Purdon et

al., 2013). Likewise, the inhaled anesthetic, isoflurane, also produces slow wave activity with

distinct UP-states and DOWN-states in the EEG(Thengone et al., 2016). While isoflurane also

acts on the $GABA_A$ receptor(Hall et al., 1994), its actions on the $GABA_A$ receptor are distinct from

those of propofol(Krasowski et al., 1998a). Furthermore, actions of isoflurane on the $GABA_A$

receptor appear to be less critical for its ability to induce anesthesia than those of

propofol(Sonner et al., 2007). Finally, both propofol and isoflurane interact with a number of other receptors in the nervous system(Eckenhoff, 2002a; Weiser et al., 2015).

It is thought that the slow EEG oscillations observed with a variety, but notably not all anesthetics(Akeju et al., 2016; Maksimow et al., 2006), are a consequence of a switch in the activity patterns of thalamic neurons. These neurons shift from tonic firing, which denote awake desynchronized states, to bursting firing pattern, which synchronizes cortical activity. Thalamic bursting activity is thought to prevent reliable transmission of sensory stimuli from the thalamus to the cortex. This hypothesis suggests that, regardless of the molecular mechanism of action, slow oscillations induced by mechanistically distinct anesthetics should lead to similar disruptions of sensory-evoked responses in the cortex.

There is recent evidence, however, to challenge this hypothesis. Arena et al demonstrate that the amplitude of visual-evoked potentials is attenuated by propofol, but enhanced by increasing concentrations of sevoflurane in rats(Arena et al., 2017). Here, we build upon these observations and characterize the differences in visual-evoked responses in mice under isoflurane and propofol. We find that although there are similarities in the spontaneous activity elicited by hypnotic doses of isoflurane and propofol, visual-evoked responses to simple visual stimuli are quite different in the primary visual cortex (V1). In the time domain, we find that responses evoked by identical visual stimuli vary dramatically between trials under both anesthetics. However, analysis in the frequency-domain reveals a consistent visual-evoked gamma oscillation (20-60Hz) present in all mice. This gamma oscillation is coherent across trials in the early phase (<250 ms) of the visual-evoked potential when mice are under isoflurane anesthesia. Despite similar drug-induced brain states, visual-evoked gamma coherence between trials is greatly attenuated when the same mice are anesthetized with steady-state, target controlled infusions of propofol. This suggests that while both anesthetics disrupt consciousness and elicit slow oscillations, only the isoflurane-induced state of unconsciousness permits phase resetting of gamma oscillations by visual stimuli.

<u>**Results**</u>

To elucidate the effect of the anesthetic state on visual-evoked brain activity, we performed in vivo electrophysiological recordings in mice head-fixed with ear bars (n= 7) presented with simple visual stimuli using equipotent doses of two different anesthetic drugs. Each visual stimulus consisted of a short, 10 ms, flash of a green LED light that covered 100% of the right visual field. Spontaneous and evoked local field potentials (LFP) were collected using an electrocorticography (ECoG) electrode placed on top of the dura over the left hemisphere, including primary visual cortex.

Survey of spectrally defined brain states under isoflurane and propofol

In order to modulate the spontaneous cortical activity, we delivered two different anesthetics: isoflurane and propofol. We were able to maintain steady state concentration of isoflurane via a nose cone delivery due to its relatively fast pharmacokinetics. Propofol was administered intravenously (IV) through a jugular venous catheter with a target controlled infusion (TCI) to ensure that the propofol brain concentration remained constant(Shortal et al., 2018).

Three out of seven mice were first given two doses of isoflurane (high-1.2%, and low-0.6%), then given two doses of propofol (low- 20 g/g brain and high – 35 g/g brain). The remaining four mice had the aforementioned exposure and were subsequently re-exposed to the same two doses of isoflurane one hour after propofol was washed out. Re-exposure served as a control for the potential brain desiccation, which might occur during long recording sessions. Re-exposure experiments also established the consistency of specimen preparation (Figure 3.1). At every anesthetic dose, one minute of spontaneous activity was collected before visual stimuli were presented. Ten seconds of spontaneous data is shown in Figure 3.2a, illustrating that burst suppression occurs with high doses of both propofol (median suppression ratio (SR) = 6.65%, interquartile range (IQR) = 25.09%) and isoflurane (median SR = 9.55%, IQR = 14.74%); and that large amplitude slow waves arise with low doses of propofol (median SR = 0.80%, IQR = 4.23%) and isoflurane (median SR = 1.15%, IQR = 4.23%).

Consistent with these observations, spectra of the ECoG signals under isoflurane and propofol overlap over frequencies ranging from 1 Hz to 4 Hz (Figure 3.2b). While with respect to slow wave activity ECoG spectra under propofol and isoflurane anesthesia were highly similar, there was slightly more power at frequencies between 6 Hz – 10 Hz under propofol. There was also an increase 0.3-1 Hz under isoflurane compared to propofol (df = 3, n= 7, *p-value* = 0.011, Kruskal Wallis, pooled isoflurane vs pooled propofol, n = 7, p=0.005, Mann Whitney U test with *post hoc* Bonferroni Correction). Thus, by administering the same animal with these two chemically distinct anesthetics, we can determine how similar slow oscillations induced with two distinct anesthetics affect the characteristics of visual-evoked responses.

Isoflurane and Propofol have dramatically different average visual-evoked responses

After one minute of baseline recording, 100 visual-evoked responses were elicited using a green LED. Averaged visual-evoked potentials (VEPs) under each anesthetic condition are shown in Figure 3.3. The shape of average VEP has historically been described by its latency to onset, amplitude, and response duration. We defined the latency to onset of the VEP as statistical deviations from the pre-stimulus data (Methods). Similarly, we define the duration of VEPs by the number of timepoints for the post-stimulus data to recapitulate the pre-stimulus statistics (Methods). We defined the amplitude of the VEP as the root mean square (RMS) of the first 350 ms of post-stimulus data. No changes in the overall amplitude of the VEP were found for different concentrations of the same anesthetic (low dose isoflurane vs high dose isoflurane: n = 7, *p* =0.999, low dose propofol vs high dose propofol, n = 7, *p* =0.902, Mann-Whitney U test). When we normalize the evoked RMS to the RMS calculated from baseline, we still observe that the overall amplitude of the VEP was similar under the two concentrations of isoflurane (low dose isoflurane vs high dose isoflurane: n = 7, *p* =0.383). Low dose propofol was associated with small but statistically significant decrease in the VEPs relative to high dose propofol (n = 7, *p* < 0.001, Mann-Whitney U test). Furthermore, we were not able to detect differences in duration of VEP at different anesthetic concentrations (low dose isoflurane vs high dose isoflurane, n = 7, *p* =0.383;

66

low dose propofol vs high dose propofol, n = 7, p=0.209, Mann Whitney U test, with *post hoc* Bonferroni Correction). In contrast, differences in VEP characteristics were strongly dependent on the identity of the anesthetic agent. The high and low doses of drugs were combined since there were no dose dependent differences. VEPs under propofol were smaller in amplitude (n = 7, *p-value amplitude*<0.001, Mann Whitney U with *post hoc* Bonferroni Correction) and shorter in duration (n = 7, *p-value* duration= 0.003, Mann Whitney U with *post hoc* Bonferroni Correction) than under isoflurane. Kruskal-Wallis test of the latencies for all four drug conditions was borderline statistically significant (df = 3, n= 7, *p-value* = 0.044). None of the *post hoc* Mann Whitney U tests for pairwise comparisons between drug conditions reached statistical significance.

Large trial-to-trial variability under both anesthetics

Two distinct scenarios can potentially give rise to the observed differences in the amplitude and duration of the average VEPs: 1) VEPs could be larger in individual trials under isoflurane than under propofol, 2) VEPs could be more consistent among trials under isoflurane. To differentiate between these possibilities, we first surveyed the single trial visual-evoked responses. We found that single trials exhibit large trial-by-trial variability and are strongly dominated by ongoing spontaneous brain activity under both isoflurane and under propofol. (Figure 3.4a). We were unable to unequivocally determine the latency of onset or duration of the VEP on a single trial basis since the post-stimulus signal did not deviate significantly from pre-stimulus ECoG. Moreover, we could not find a difference in the amplitude of the single trial responses under isoflurane and propofol (χ^2= 1.05, df = 3, n= 7, *p-value* = 0.197, Kruskal Wallis). Despite this inter-trial variability, averaging across all 100 trials reveals a clear, visual-evoked potential. The shape of the average evoked potential, however, rarely resembles any individual trial (Figure 3.4b). Moreover, individual visual evoked trials do not have the same waveform in the time domain. We measured the average pairwise correlation between single trials as an indicator of reliability under each dose of each anesthetic(Kumbhani et al., 2007; Tiesinga et al., 2003). In aggregate, in the time domain, visual evoked single trials are weakly correlated with each other

under both anesthetics. Yet, there is a significant increase in the reliability under isoflurane (pooled mean reliability under isoflurane= 0.205) than under propofol (pooled mean reliability under isoflurane = 0.063) (n = 7, *p-value pooled reliability*<0.001, Mann Whitney U with *post hoc* Bonferroni Correction). This suggests, that the observed differences in the average VEPs under isoflurane and propofol are likely due to differences in the inter-trial consistency of responses rather than to differences in the shape of the VEP on individual trials.

Visual-evoked gamma power under isoflurane and propofol

While VEPs vary dramatically between trials in many respects, one aspect of the VEP – an oscillation around 40Hz – was highly consistent between trials and was present in all mice (Figure 3.5). This gamma oscillation can be clearly visualized in the frequency domain (Figure 3.6). To extract the frequency, power and phase characteristics of oscillations present in visual-evoked responses, we convolved single trials with a series of Morlet wavelets. Spectra averaged across trials were then normalized to the pre-stimulus interval (Figure 3.6a). On average, over the first 250 ms, higher gamma power (20-60 Hz), was evoked by the visual stimulus under isoflurane than under propofol (timepoints = 900, p-value<0.000001, Mann Whitney U).

To determine the variability of the phase of the visual-evoked gamma oscillation, we computed inter-trial phase coherence (ITPC) at each point in the time-frequency plane. Consistent with the observations in the time domain (Figure 3.5), ITPC was significantly increased in the gamma range following the visual stimulus. This increase in the ITPC was most prominent between 50 and 250 ms after stimulus between 20-60Hz (Figure 3.6b). Moreover, the increase in ITPC was larger during anesthesia with isoflurane than propofol. Propofol's reduced ITPC recovered following washout of propofol and re-exposure to isoflurane. Note, that coherence is normalized to signal power. Thus, differences in the ITPC cannot be attributed to higher power of gamma oscillations under isoflurane.

Figure 3.7 shows the difference between ITPC evoked under isoflurane and propofol. Here, both high and low concentrations for each individual anesthetic were combined, the anesthetic agent effects are larger than the concentration-dependent effects (Table 1). Yellow colors represent higher ITPC under isoflurane while dark blue colors represent higher ITPC under propofol. The maximum difference in evoked coherence occurred 80-130 ms after stimulus onset and was centered at 36 Hz. Indeed, we found a significant increase in the ITPC under isoflurane compared to propofol (timepoints = 900, p-value<0.000001, Mann Whitney U). Significant decrease in ITPC in the gamma range were present in each mouse (table 2). In 6 out of 7 mice, the visual evoked gamma coherence is statistically greater under isoflurane than under propofol anesthesia with *post hoc* Bonferroni correction. In contrast to the consistent increase in gamma coherence following the visual stimulus, the increase in coherence at lower frequencies (1-5 Hz, centered at 3 Hz) was not consistent among animals. Moreover, none of the average VEPs exhibited a clear oscillation in the 1-5 Hz range that lasted for one or more cycles.

Discussion

Maintenance of a stable perceptual world is a fundamental requirement of consciousness. In order to create such stable representation of the sensory stimuli, sensory information must be faithfully relayed and integrated with ongoing spontaneous brain activity. The mechanisms through which general anesthetics disrupt perception remain a mystery. Furthermore, it is unknown whether mechanistically distinct classes of anesthetics disrupt sensory processing in a similar manner. Here, we show that although two chemically distinct anesthetics, isoflurane and propofol, produce similar spontaneous ECoG activity, visual-evoked responses recorded in primary visual cortex obtained during each anesthetic state are quite different. When mice are anesthetized with isoflurane, there is a consistent visual-evoked gamma band oscillation (20-60Hz), which is synchronous across trials. However, when the same mice are anesthetized with propofol, visual-evoked gamma coherence between trials is greatly attenuated. This decrease in consistency of visual responses to identical stimuli likely contributes to the decrease in the size and duration of the visual-evoked responses under propofol.

Curiously, both anesthetics elicit similar oscillations in the spontaneous LFP. For instance, under high concentrations of both propofol and isoflurane, the LFP was characterized by burst suppression. Yet, the consistency of elicited responses varied dramatically depending on whether propofol or isoflurane was used to elicit burst suppression. These observations complicate analysis of "brain state" under anesthesia on the basis of spontaneous oscillations in the LFP.

Sensory neurophysiology research under anesthesia

For decades, much of sensory neurophysiology research has been performed in anesthetized preparations. There is increasing evidence that anesthetized and awake sensory responses differ greatly(Imas et al., 2005b; Reinhold et al., 2015a; Storchi et al., 2017). For example, visual cortical responses quickly adapt to a train of high frequency visual stimuli when mice are under isoflurane compared to the awake state(Reinhold et al., 2015a). This adaptation is thought to occur because under isoflurane, there is synaptic depression at the level of the lateral geniculate thalamic cells(Reinhold et al., 2015a). Furthermore, responses in V1 depend strongly on the behavioral state such as resting vs. running(Niell and Stryker, 2010). It is less obvious, however, that responses to simple visual stimuli in V1 should depend strongly on the anesthetic agent. The fact that responses to a simple flash in V1 depend strongly upon whether propofol or isoflurane was used to maintain anesthesia is especially surprising because the spontaneous fluctuations in brain activity produced by these anesthetics are very similar.

It is often difficult to determine how animals were anesthetized in existing literature. Methods sections sometimes note the fluctuations in the spontaneous EEG as a proxy for defining the brain state at the time of recording. However, given the results presented here, along with findings by others(Arena et al., 2017), the type of anesthetic can dramatically alter sensory responses even when the spontaneous oscillations in the ECoG signals are similar. Thus, the traditional characterization of the oscillations of spontaneous brain activity does not appear to unequivocally specify the characteristics of responses evoked by the visual stimulus.

Possible mechanisms of gamma coherence breakdown under propofol

Variability of evoked responses to identical sensory stimuli limits the ability of these response to reliably convey information about stimulus attributes. Currently, it is not understood which parameters of the visual evoked response encode sensory information. We find that the animal-to-animal and trial-to-trial variability of the visual evoked response decreases in the phase of the visual-evoked gamma oscillations. This makes the phase of the gamma oscillations an appealing candidate for encoding the visual stimulus. Gamma activity can be elicited by one of two prevailing mechanisms. The first arises from strongly activating interneuron-interneuron networks (I-I).(Ermentrout and Kleinfeld, 2001; Kopell et al., 2000; Vinck et al., 2015; Wang and Buzsáki, 1996) The second comes from reciprocally activating interneurons and pyramidal neurons (E-I)(Cardin, 2016a; Friston and Buzsáki, 2016; Sohal, 2016; Traub et al., 1996, 2016a; Whittington et al., 2000; Wilson and Cowan, 1972). Critical for both of these mechanisms is the shape of the IPSPs produced by fast spiking GABAergic interneurons. Propofol allosterically potentiates GABA signaling through the $GABA_A$ receptor(Hales and Lambert, 1991; Krasowski et al., 1998b; Weiser et al., 2015; Yip et al., 2013). Therefore, under propofol, the duration of the IPSPS may be prolonged(Bai et al., 1999). This may be why we see a decrease in total gamma power under propofol, and in some animals (for example, shown in figure 3.6), we see a shift to lower evoked gamma power. However, one caveat to this hypothesis is that isoflurane also is a positive allosteric modulator at synaptic and extrasynaptic $GABA_A$ receptors(Garcia et al., 2010; Krasowski et al., 1998a; Wang, 2009). Isoflurane suppresses GABAergic IPSPs at lower concentrations(Banks and Pearce, 1999; Jones and Harrison, 1993; Pearce, 1996) but, in a hippocampal slice preparation concentrations similar to that used in this study increased the amplitude and duration of GABAergic IPSPs(Miu and Puil, 1989). Yet, other studies in amygdalar slices suggest that isoflurane prolongs $GABA_A$ mediated currents without effectively increasing their amplitude(Ranft et al., 2004). Both isoflurane and propofol are highly promiscuous drugs that have significant interactions with a host of membrane proteins(Eckenhoff, 2002b; Tang and Eckenhoff, 2018; Weiser et al., 2015). Thus, in the absence of detailed biophysical model, which

would include actions of both propofol and isoflurane at the plurality of their molecular targets, it is difficult to attribute the differences in the visually induced gamma oscillations to specific differences in the molecular mechanisms of action of either anesthetic. Perhaps, most surprising is the difference in the visual-evoked responses under deep anesthesia characterized by burst suppression. *In vivo* extracellular and intracellular recordings in cats suggest that burst suppression induced with either propofol(Kroeger and Amzica, 2007) or with isoflurane(Amzica, 2009; Ferron et al., 2009b; Kroeger and Amzica, 2007) is associated with hyper-excitability of the cortex. Our observations concur with that of Amzica and colleagues – visual stimuli presented under both isoflurane-induced and propofol-induced burst suppression during the suppression period of the ECoG could on occasion trigger bursts(Amzica, 2009; Ferron et al., 2009a; Kroeger and Amzica, 2007). Yet, our results suggest that burst suppression induced with isoflurane allows visual stimuli to entrain the phase of the gamma oscillations while burst suppression induced with propofol does not.

Exactly how the laminar structure of the primary visual cortex generates spontaneous and induced gamma rhythms in V1 is also unknown. There is some evidence that the granular layer of V1 is more resistant spectral composition changes under a mixture of isoflurane and xylazine as compared to higher order brain regions in ferrets(Sellers et al., 2013). Moreover, mice under isoflurane/xylazine, tend to have spontaneous gamma waves that begin in all layers simultaneously, however, visual evoked gamma oscillations begin in granular and supra-granular layers(Welle and Contreras, 2015). This may be because isoflurane increases the number of excitatory and inhibitory cells that are recruited to participate in synchronous responses, as seen in Noda and Taskashi, 2015(Noda and Takahashi, 2015). This would also correspond well to findings seen in ferrets which show that visual evoked multiunit activity have a longer duration when animals are anesthetized with isoflurane/xylazine compared to in the awake state. Interestingly, just because gamma oscillations are seen in the superficial layers does not necessarily mean that there is in fact gamma oscillations in the deeper layers, or that there is

strong synchrony between spiking activity and phase of the gamma oscillation(Sellers et al., 2015; Welle and Contreras, 2015).

Visual-evoked gamma power and frequency has also been shown to increase with arousal and locomotion in mice(Fu et al., 2014; Niell and Stryker, 2010; Polack et al., 2013). While we can rule out locomotor effects given our anesthetized preps, the activation of arousal circuitry may be different under these two anesthetics. Indeed, when mice have larger pupillary diameters, indicating increased arousal(Aston-Jones and Cohen, 2005; Eldar et al., 2013; Gilzenrat et al., 2010), visual evoked responses have large signal to noise ratio, and exhibit two peaks of visual evoked gamma power centered around 75 Hz and 30 Hz(Vinck et al., 2015). These effects may be caused by neuromodulation from sleep and arousal systems. For example, the mix of cholinergic tone and noradrenergic input has been shown to maintain high signal to noise seen in V1 neurons during arousal and locomotion in mice(Polack et al., 2013). Moreover, cholinergic projections from the basal forebrain have been shown to increase visual evoked gamma oscillations in mice(Lee et al., 2014; Pinto et al., 2013). Our results thus may indicate that propofol may depress arousal circuitry involving cholinergic and noradrenergic input more than isoflurane. Thus, understanding how anesthetics alter sensory responses may help us formulate hypotheses about the mechanisms by which anesthetics affect the sleep and arousal system to differentially produce unconsciousness.

Functional Implications

The precise functional implications of visual-evoked gamma oscillations are currently unknown. Some evidence suggests that the sensory evoked gamma oscillations modulate the firing of sensory neurons and increase the efficiency of sensory encoding(Cardin et al., 2009; Womelsdorf et al., 2006, 2012). This may occur through decreasing noise by increasing inhibitory drive, or increasing signal by entraining sensory evoked firing to a specific phase of the gamma oscillation(Cardin et al., 2009; Fries et al., 2001; Sohal, 2016). It is important to note that we not only observe visual evoked gamma oscillations in the single trial data, and increase in gamma

power, but also that this increase in gamma power is consistent in phase from trial to trial under isoflurane. This implies that the neural processes leading to visual evoked responses occur in a stereotyped fashion under isoflurane compared to propofol anesthesia. A possible mechanism leading to such a phase resetting effect would be strong synchrony in visual cortex neuronal firing under isoflurane compared to propofol. Indeed, in ferrets given isoflurane and xylazine, visual stimuli increase ITPC in V1, however, when the same animals are awake there is an increase in ITPC both in V1 and in the PFC, thereby indicating that such phase coherence may be important for functional connectivity between different regions of the brain(Sellers et al., 2015). However, it is not yet clear if this increase in phase synchrony across the brain will necessarily be able to provide more information for encoding stimulus attributes. For example, there is an increase in auditory evoked gamma coherence between different areas of rat auditory cortex and belt in rats under isoflurane anesthesia as compared to awake rats(Noda and Takahashi, 2015).

Limitations

While visual-evoked gamma oscillations have been shown in both awake animals and in anesthetized animals, how these oscillations are associated with perception is beyond the scope of this presented research. To understand how the integration of brain state and the visual-evoked gamma oscillations affects perception, one must create a behavioral paradigm in which animals report their response to visual stimuli.

Another limitation is that all mice were induced with isoflurane and measured under the two doses of isoflurane before they were given propofol. Therefore, under the propofol delivery, there may be a slight mixing effect with isoflurane. This paradigm was chosen because in the acute setting, our induction and insertion of the jugular venous catheter is best done with isoflurane. This is because isoflurane has fast on – off kinetics and is much easier to titrate during the long, invasive surgeries of jugular cannulation and craniotomy. To induce and maintained an animal with only propofol, one would need to chronically insert the jugular catheter, allow the animal to recover, and then induce the animal with propofol for neurosurgery and beginning the

experiment. Moreover, the animal may need a relatively high dose of propofol for induction, which may take a long time to wash out to maintain a steady state low dose for visual stimulation. We attempted to correct for the amount of isoflurane present within the brain of animals by starting propofol delivery 45 minutes before recording visual evoked potentials with isoflurane off. Previous results by Kelz et al 2008 show that the brain has at most trace levels of isoflurane after 15 minutes after isoflurane is turned off(Friedman et al., 2010; Yanagisawa et al., 2008). Therefore, after 45 minutes of isoflurane off and propofol infusion, there should be virtually no isoflurane within the mouse brain. We also monitored propofol washout kinetics using the model that was fit to reflect the elimination time constant from the brain(Shortal et al., 2018). Thus, while there is a trace amount of propofol in the brain during the re-exposure to isoflurane, the albeit incomplete, recovery of responses first observed under isoflurane suggest that the order of drug administration is not likely to be a major contributor to our findings.

Finally, through employing high density, multichannel recording methods, including ECoG as we have used here, we can start asking questions about how visual evoked activity that initiates in V1 propagate to other visual areas. Answering such questions requires extensive analysis of the dynamically changing correlation structure of the spontaneous and evoked activity across electrodes. Moreover, concluding how anesthesia affect the propagation of such signals will require further parameterization of the visual stimulus characteristics as well as brain state with different anesthetics.

Conclusions

Here, we show that even when the spontaneous activity of the brain shows similar spectral features, i.e., delta power or burst suppression, visual evoked activity is better correlated with the anesthetic drug rather than with the ensuing spectral state of the brain. Therefore, the canonical methods of defining the brain state with spontaneous spectral activity are not complete. Recently there has been a resurgence in efforts to define the state of the brain as induced by different anesthetic agents. One promising approach uses phase based functional connectivity

measures to determine the flow of information from one brain region to the other(Kim et al., 2016; Lee et al., 2013a). Another interesting set of methods include observing changes in the dynamics of the correlations in the signals from multiple electrodes(Solovey et al., 2015). Critical to the success of these methods is the understanding of how these models cope with sensory perturbations. Therefore, in addition to studying spontaneous activity under anesthesia and wakefulness, it will also be important to observe sensory evoked activity.

Methods

Animals: All experiments in this study were approved by Institutional Animal Care and Use Committee at the University of Pennsylvania and were conducted in accordance with the National Institutes of Health guidelines. All experiments were performed using adult (12–28 weeks old, 20–30 g) male and female C57BL/6 mice (Jackson Laboratories). Mice were housed under a reverse 12:12 h, light: dark cycle. Mice were provided with food and water ad libitum. A total of 11 mice were recorded from in this study. Inclusion criteria for mice included the following: 1) presence of spontaneous activity that was not characterized as burst suppression at lower drug concentrations 2) presence of visual-evoked potentials at each dose of each anesthetic (as defined by the absolute value of the average LFP response exceeding 5 standard deviations of pre-stimulus data within 200 ms after stimulus presentation). With this inclusion criteria, we present data from 7 mice in this study.

Surgery: All surgery was performed under aseptic conditions. Each animal was weighed (20–30 g) immediately prior to surgery to adequately dose propofol delivery. Prior to surgery, 2 mg/kg of dexamethasone was given subcutaneously (SQ) to reduce brain edema. Animals were induced with 2.5% isoflurane in oxygen (flow rate 500ml/min), and maintained at 1.5% isoflurane for the remainder of the surgery. Core-body temperature was maintained at 37 (± 0.5) ˚C using a temperature controller with core-body temperature monitoring (TC- 1000 Temperature Controller, CWE, Incorporated, Ardmore, PA, USA). First, a jugular venous catheter was placed prior to neurosurgery to allow for Targeted Controlled Infusion (TCI) propofol infusion as described in Shortal et. al, 2018. Animals were then secured into a Kopf stereotaxic frame. 0.25ml of 2%

lidocaine gel was applied to the scalp to provide a local nerve blockade during surgery. The scalp was then incised and retracted, permitting maximum exposure of the surface of the skull. The bone was cleaned and dried before a craniotomy was performed using a dental drill. One large craniotomy was drilled over the left hemisphere (+1mm to -5 mm AP, +0.25 mm to +6 mm ML of bregma), and a small reference screw was secured in the right skull bone (+1mm AP, +1mm ML of bregma). A 64-electrode surface grid (Neuronexus: E64-500-20-60) was positioned over the dura to obtain ECoG signal. Mineral oil was applied on top of the ECoG grid every 20 minutes to preserve the health of the underlying dura and brain. Animals were scarified the same day immediately after the final visual recording session.

Visual Stimulation: Visual stimuli consisted of a brief 10 ms flash of a bright green LED light (0.43 mW/cm^2), placed 2 cm away from the mouse's right eye. The flash covered 100% of the mouse's visual field. 100 flashes were given under each anesthetic dose step.

Anesthetic delivery protocol: After the jugular catheter was placed and the craniotomy was completed, the doses and anesthetics were parametrically altered. The animal was first given two doses of isoflurane (Terrell Isoflurane, Novaplus): 1.2% (high dose isoflurane) and 0.6% (low dose isoflurane). Animals always received the higher isoflurane concentration before receiving the lower dose. The brain was allowed 15 minutes to equilibrate after the amount of isoflurane was changed(Friedman et al., 2010). After the two isoflurane doses, the TCI propofol (1000mg per 100ml Diprivan, Fresenius Kabi USA) was administered using the model described in Shortal et. al, 2018(Shortal et al., 2018). The two target concentrations were 20 g/g brain (low dose propofol), and 35 g/g brain (high dose propofol). One out of seven of the mice was producing spontaneous movement at the 20 g/g brain dose of propofol. Therefore, this mouse received 30 g/g brain for low dose propofol, and 40 g/g brain for high dose propofol to maintain slow waves and burst suppression activity, respectively. Due to the slow rate of excretion of propofol, the lower concentration of propofol was administered before the higher dose. Due to the fast rate

of onset of propofol, the equilibration time between propofol changes was 8 mins. Animals were not intubated, nor was an arterial catheter placed for pCO_2 or blood pressure measurement.

In 4 of the 7 animals, re-exposure doses of isoflurane were given in order to control for possible brain desiccation effects or impedance changes from keeping a large craniotomy open for a long period of time. In these animals, after achieving the 35 ug/g brain concentration of propofol, the propofol infusion was turned off and 1.2% isoflurane was administered for 1 hour in order to allow propofol to wash out. Propofol washout was monitored using the same TCI model used for propofol delivery. This model estimates the amount of propofol remaining in the brain parenchyma. Following this wash out period, visual stimuli were again given under 1.2% and 0.6% re-exposure isoflurane.

Electrophysiology and preprocessing: In 6 mice, signals were amplified via a Neuralynx headstage (HS36), digitized through Cheetah 64 acquisition system (Neuralynx, ERP-27, Lynx-8), and collected at a rate of 3030.3 samples/second. In one mouse, signals were amplified via an Intan headstage (Intan, RHD2132), digitized through Omniplex acquisition system (Plexon, Omniplex), and collected at a rate of 30,000 samples/second.

LFP data collected with Neuralyx was filtered online using a proprietary FIR filter between 0.1 Hz and 325 Hz. LFP data collected with Plexon was filtered offline using a custom-built FIR filter between 0.1 Hz and 325 Hz, with the MATLAB functions, *firls.m* and *filtfilt.m*. Offline, both data sets were decimated to 1000 samples/second, noise channels were manually removed and trials with excess motion artifact or saturated data was rejected before the mean was subtracted from the data. All data analysis was completed using custom built Matlab (Mathworks) code unless otherwise stated.

Selection of electrode over Primary Visual Cortex (V1): The latency of onset of the visual-evoked potential was calculated for each electrode in the array as the time point at which if their post-stimulus average exceeds 3 standard deviations above the pre-stimulus baseline for 3

consecutive time points. The electrode which had the lowest latency of onset was denoted as V1. The amplitude of the VEP was calculated by determining the Root Mean Square (RMS) of the first 350 ms of post-stimulus data. This was determined for both raw voltage signals and for voltage signals normalized to 500 ms of pre-stimulus data and expressed as a z-score.

$$RMS = \sqrt{\frac{1}{n}(x_1^2 + x_2^2 + \cdots + x_n^2)}$$

Where x is the voltage in the post-stimulus average, and n is the time point in ms. Duration of the VEP was defined as the first time point in which the post-stimulus data returns to within 2 standard deviations of the pre-stimulus data for 20 consecutive time points

Quantification of reliability in time domain: To asses reliability of the LFP evoked response to the visual stimulus in time domain, a similar method was used to that of Kumbhani et al 2007 and Schreiber et al 2003(Kumbhani et al., 2007; Tiesinga et al., 2003). First, pairwise correlations of single trial evoked potentials were computed over the first 350 ms of post stimulus activity for each dose of each anesthetic. These correlations were then averaged together to compute reliability. Correlation was computed using the Matlab *corr.m* function.

$$Reliability = \frac{\sum_{i=1}^{trials}\sum_{j=1+i}^{trials}(LFP_i - \mu_i)(LFP_j - \mu_j)\Big/ \sigma_i * \sigma_j}{(trials^2 - trials)\Big/ 2}$$

Where LFP_i is the evoked response during the *i*-th trial, μ_i and σ_i are the mean and standard deviation of the single trial response.

Quantification of suppression ratio (SR): To asses determine which epochs of the LFP were suppressed, both a frequency based metric and an amplitude based matric was applied to the data. First, spectrograms were calculated using multi-taper spectral analysis by applying the MATLAB function, *swTFspecAnalog.m*, written by Dr. Andrew Hudson. Spectral analysis was performed from 2 Hz to 500Hz with a set of 5 Slepian tapers, over a window size of 500 ms, with

80% overlap. The total power was then calculated for each window for frequencies between 2 and 100 Hz. The resultant total power time series of a burst suppression data set (high dose isoflurane or high dose propofol) was then subjected to k-means clustering to find 2 centroids- one that would correspond to bursts, and the other to suppressions. From this, the maximum threshold for classifying suppression based on total power was calculated for each mouse. Concurrently, RMS was also calculated over the LFP data in 500 ms windows with 80% overlap. A manual maximum RMS threshold by eye was selected for each mouse. Time windows were classified as suppression as long as the total power and RMS were below their respective thresholds. The suppression ratio (SR) was calculated by number of time windows with suppression divided by the total number of time windows.

Spectral analysis of spontaneous LFP: One minute of unstimulated LFP was extracted from each mouse under each concentration of isoflurane and propofol. Re-exposure isoflurane baseline data was excluded since excess propofol may have remained within the brain given the propofol's slow excretion rate. Power spectral density of each segment was calculated using multi-taper spectral analysis by applying the MATLAB function, *mtpsd.m*, written by Dr. Andrew Hudson. Spectral analysis was performed from 0.05 Hz to 100Hz with a set of 20 slepian tapers. All power spectra were normalized to total power. The average power spectra and 95% confidence intervals for each concentration of isoflurane and propofol was calculated using the ensuing normalized power spectra. Spectra in **Figure 3.2b** are show on a log-log scale.

Wavelet analysis: Power, phase, and frequency information was extracted by convolving single trial data with a set of Morlet wavelets (0.1 Hz to 150 Hz, with a step-width 0.25 Hz and normalized amplitude), generated with using continuous wavelet transform, *contwt.m*, in MATLAB, written by Christopher Torrence and Gilbert Compo (available at: http://paos.colorado.edu/research/wavelets/)(Torrence and Compo, 1998). The ensuing power spectrograms of single trial data were averaged within each mouse, under each concentration of

isoflurane and propofol. The average spectrograms were then normalized to 300 ms of baseline data. Spectrograms shown in **Figure 3.6** are shown with frequency in log space.

Inter-trial Phase Coherence (ITPC) Analysis: Inter-trial phase coherence (ITPC) was used to quantify the amount of phase synchrony between trials at each frequency. ITPC over V1 in each mouse under each concentration of anesthetics. First, angle vectors were extracted from the wavelet coefficients at each time point and each frequency by applying Euler's formula and setting the single trial vector length to 1. ITPC was then calculated by taking the mean length of the angle vector across trials. ITPC at each timepoint and frequency of all mice were averaged separately under isoflurane and propofol. **Figure 3.7** shows the difference in the average visual-evoked ITPC between mice under isoflurane and propofol.

Statistical Analysis: Statistics presented in **Figure 3.3** were presented using Krustal Wallis Mann test for group comparison and a Mann Whitney U test for concentration specific effects. P-values were Bonferroni corrected for multiple comparisons among 4 groups. **Figure 3.7** were performed using Mann Whitney U tests. P-values were made more stringent using a Bonferroni correction for multiple comparisons among 900 time points.

Figures
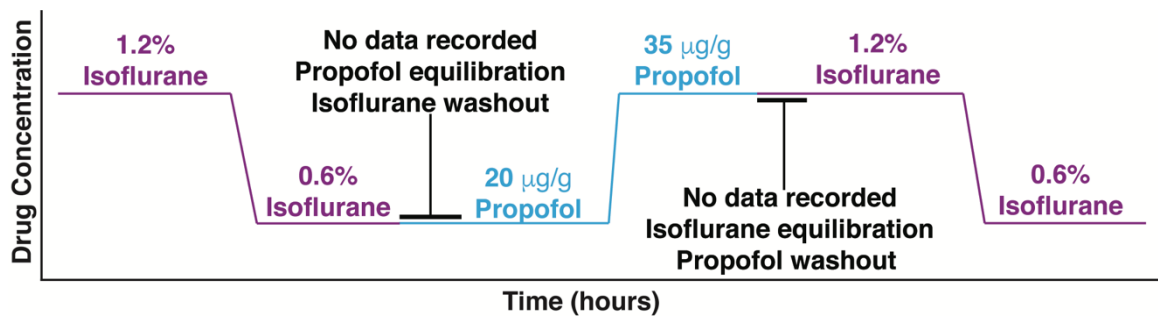
Figure 3.1 Experimental Design

Mice were first given two doses of isoflurane (high-1.2%, and low-0.6%), then given two doses of propofol (low- 20 μg/g brain and high – 35 μg/g brain). Between isoflurane and propofol recordings, the brain was allowed 45 minutes to wash out isoflurane and establish equilibrium with propofol. 4 out of 7 mice were re-exposed to the high and low isoflurane doses after propofol was washed out for one hour.
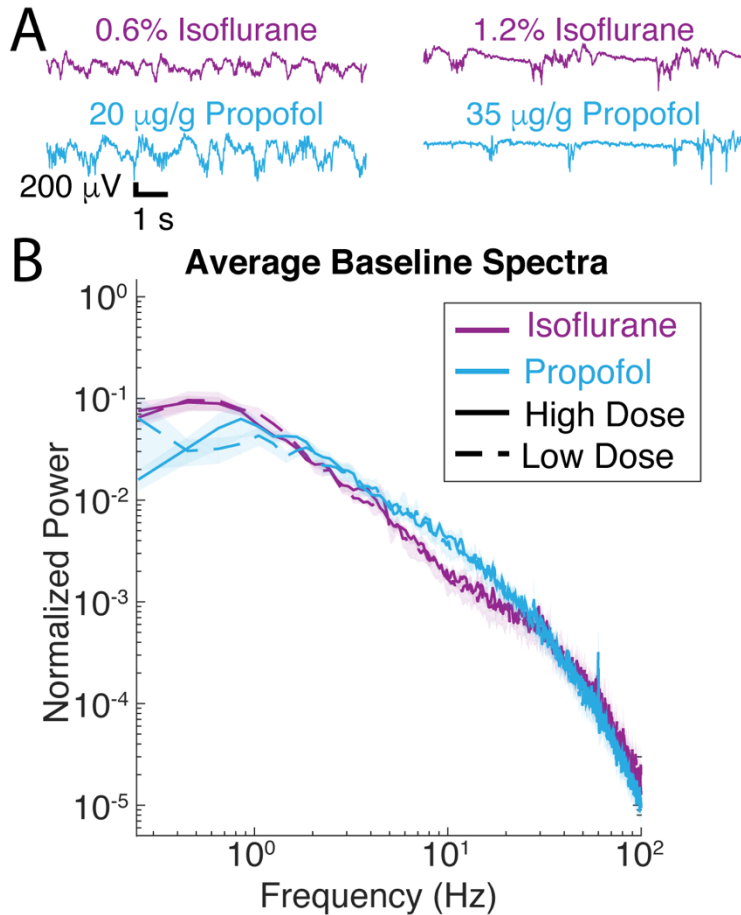
Figure 3.2 Spontaneous LFP of mice under isoflurane and propofol have similar spectral characteristics

(A) 10 seconds of unstimulated local field potential (LFP) recorded in V1 under high dose isoflurane (1.2%), low dose isoflurane (0.6%), high dose propofol (35 µg/g brain), low dose propofol (20 µg/g brain).

(B) Power spectra of 1 minute of unstimulated LFP from V1 were computed for all 7 animals. Blue curves are from animals under propofol, while purple traces are from animals under isoflurane. Solid lines denote high drug concentrations while dashed denote low drug concentrations. Shading represents the 95% confidence intervals for each condition.
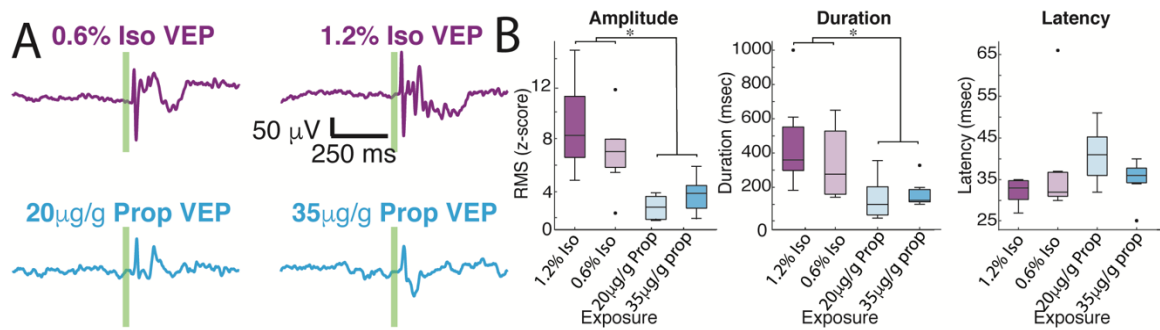
Figure 3.3 Average visual evoked responses under isoflurane and propofol are dramatically different within the same animal

(A) Average of 100 flash trials under each does of isoflurane (top) and propofol (bottom). The flash is denoted by the green vertical line.

(B) (B) Quantification of average VEP amplitude (n = 7, p-value amplitude<0.001 , Mann Whitney U with post hoc Bonferroni Correction), duration of VEP (n = 7, p-value duration= 0.003, Mann Whitney U with post hoc Bonferroni Correction), and latency of onset (df = 3, n=7, p-value = 0.044, Kruskal Wallis). asterisks (*) denote p-values <0.01.
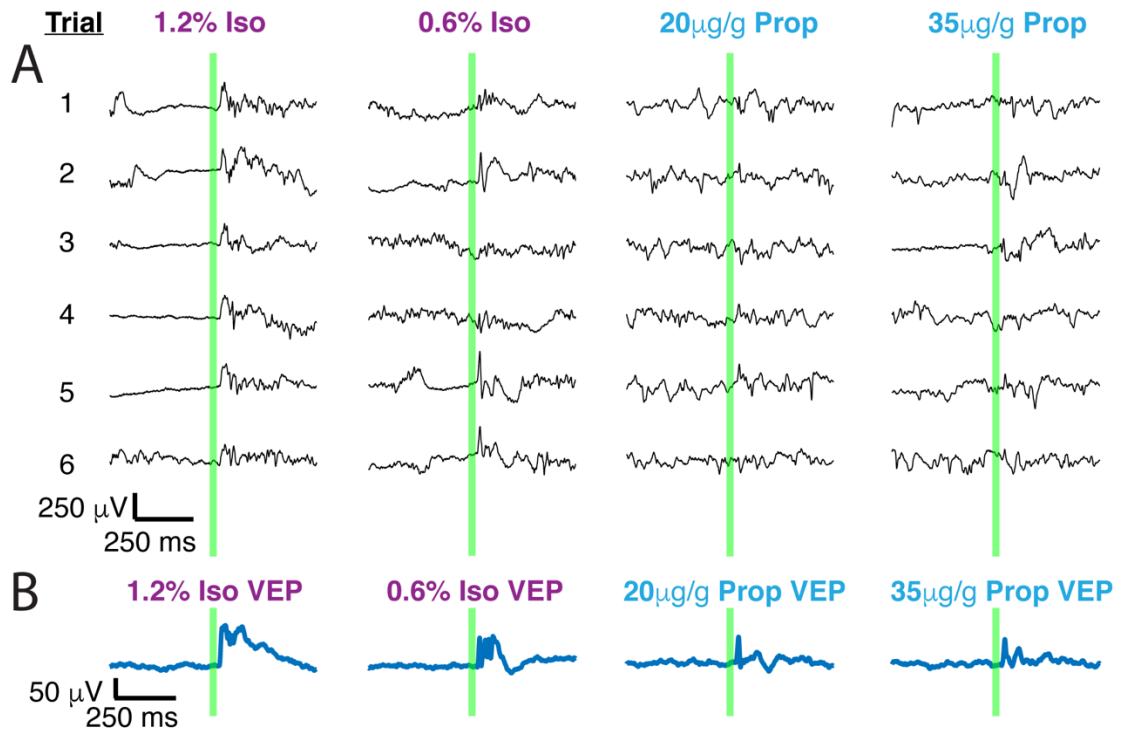
Figure 3.4 Single trials of visual evoked potentials under isoflurane and propofol both have high trial by trial variability:

(A) Six out of 100 randomly chosen individual flash evoked potentials (thin black traces) under high and low doses of each anesthetic: isoflurane, propofol.

(B) The average VEP over 100 trials for each anesthetic concentration. The flash is denoted by the green vertical line in both panels.
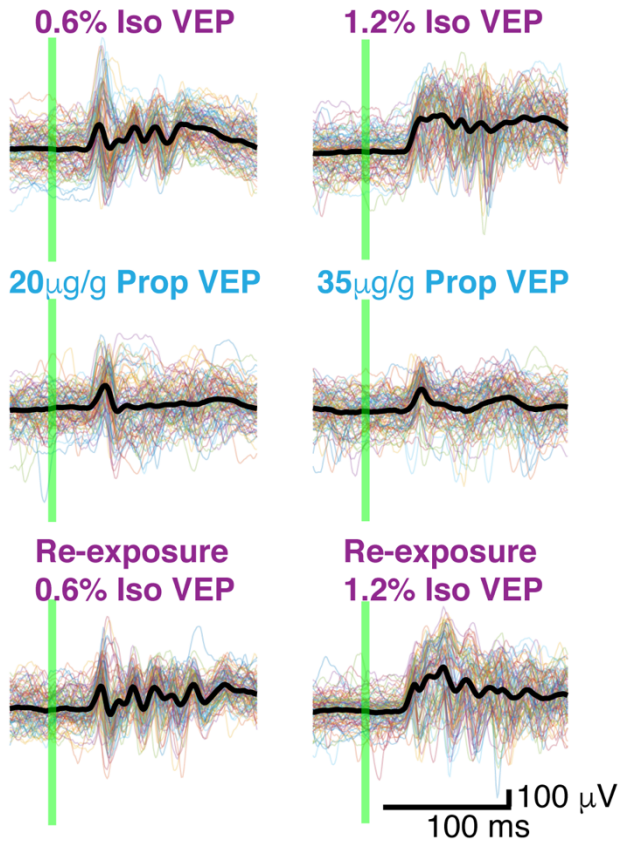
Figure 3.5 Butterfly Plots

Thin colored traces under high and low doses of each anesthetic: isoflurane, propofol, and isoflurane re-exposure in the same animal. Thick black lines represent the average VEP under each dose of each anesthetic. The flash is denoted by the green vertical line.
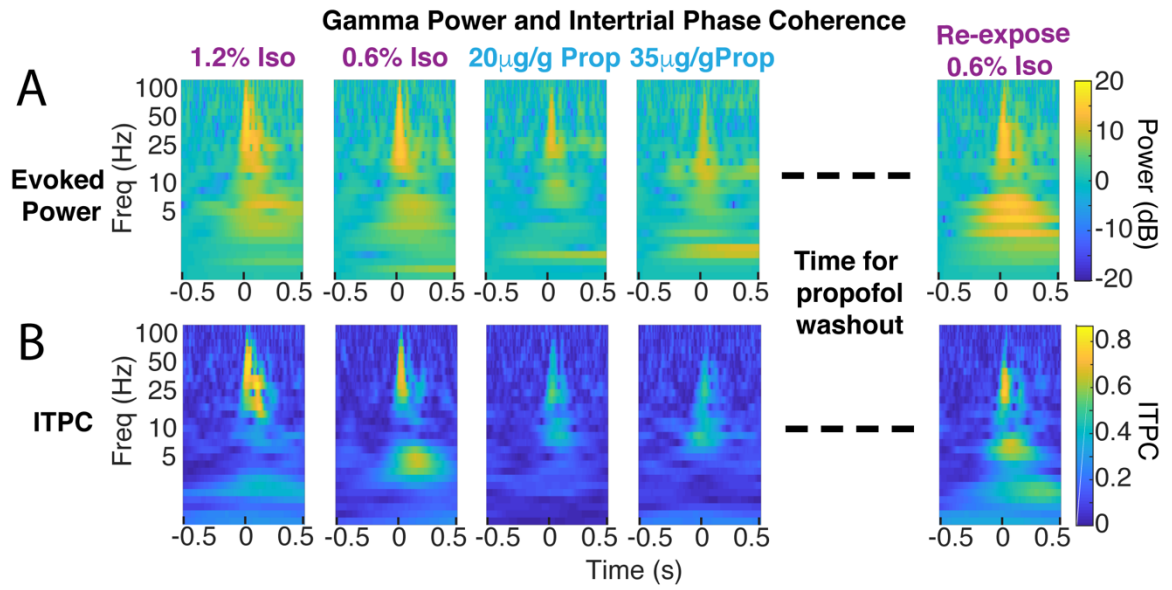
Figure 3.6 Decrease in coherent evoked gamma power in propofol compared to isoflurane within the same animal

(A) Color plot of average evoked power (first isoflurane exposure in the left panels, propofol exposures in the middle panels, and re-exposure to isoflurane acquired one hour after propofol wash out in the right panels).

(B) Color plot of ITPC
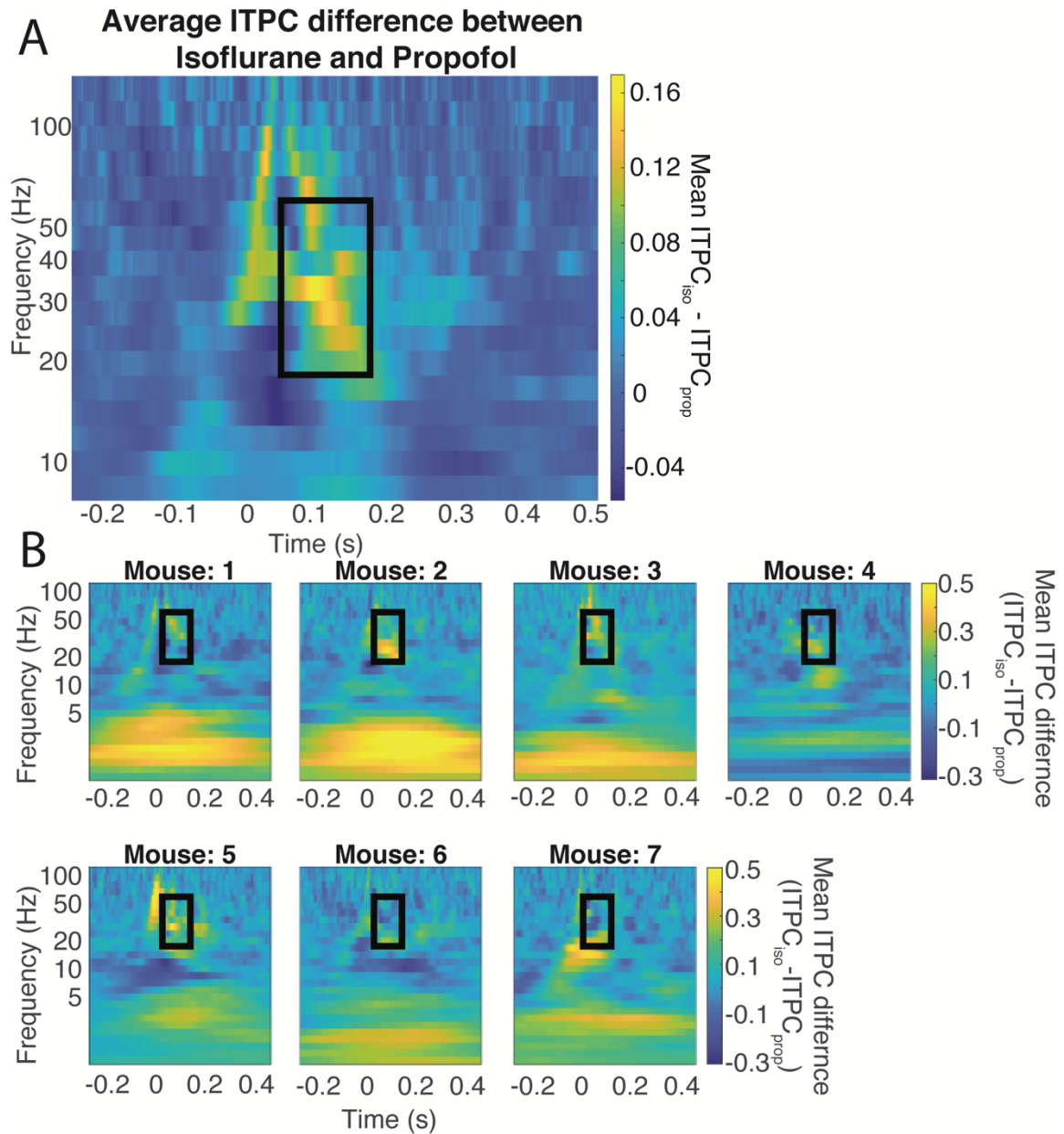
Figure 3.7 Difference in coherence is in the evoked gamma band

(A) Average difference between the ITPC under both doses of isoflurane and propofol. Yellow colors represent higher ITPC under isoflurane while dark blue colors represent higher ITPC under propofol. The maximum difference in evoked coherence occurs within the black rectangle, at 80 ms after stimulus onset and is centered at 36 Hz. The

Quantification of the ITPC in the gamma range (20-60 Hz) within the black rectangle

yields a significant difference between the gamma coherence of visual evoked responses

(timepoints = 900, p-value<0.000001, Mann Whitney U).

(B) Individual difference between the ITPC under both doses of isoflurane and propofol.

Yellow colors represent higher ITPC under isoflurane while dark blue colors represent

higher ITPC under propofol. The Quantification of the ITPC in the gamma range (20-60

Hz) within the black rectangle yields a significant difference between the gamma

coherence of visual evoked responses.

Tables

Table 3.1: Difference in evoked gamma coherence across mice (all p-values are Bonferroni corrected unless otherwise specified)

Comparison	Mann-Whitney U p-Value for ITPC difference
Pooled Isoflurane – Pooled Propofol	<0.000001
Low Dose Isoflurane – High Does Isoflurane	Uncorrected p-value = 0.0611
Low Dose Propofol – High Does Propofol	<0.000001
Low Dose Isoflurane – Low Does Propofol	<0.000001
High Dose Isoflurane – High Does Propofol	<0.000001

Table 3.2: Individual mouse differences in evoked gamma coherence from Isoflurane – Propofol (all p-values are Bonferroni corrected unless otherwise specified)

Mouse	Mann-Whitney U p-Value for ITPC difference
1	0.336
2	<0.000001
3	<0.000001
4	<0.000001
5	<0.000001

6	<0.000001
7	<0.000001

CHAPTER 4 - Mechanistically Distinct Anesthetics Commonly Disrupt Visual Evoked Feedback, But Exert Agent-Specific Impairment of Feedforward Signaling in Mice

Abstract

Feedforward and feedback signaling are critical for sensory information processing across the cortical hierarchy. In awake mice, simple visual stimuli evoke two traveling waves that span much of a cortical hemisphere: a fast (30-50Hz) feedforward wave and a slow (3-6 Hz) feedback wave. If these waves denote critical elements of visual processing, the delivery of hypnotic doses of anesthesia should impair their propagation patterns. To explore how arousal state affects the spatiotemporal properties of visual evoked responses, we performed high density electrocorticography recordings in mice during wakefulness or under mechanistically distinct anesthetics. We demonstrate that simple visual stimuli evoke fast oscillations over the cortical surface in all mice, regardless of anesthetic state. However, attributes of fast feedforward waves including single trial reliability, signal to noise, and spatial activation pattern, are disrupted in drug specific manner. Conversely, visual stimuli fail to evoke large amplitude slow oscillations under any of the anesthetics. Thus, evoked slow waves are rarely elicited, contain low signal to noise, and have highly variable spatial activation patterns in anesthetized animals. Moreover, evoked slow waves observed in anesthetized animals resemble those elicited from weak stimuli in awake animals. Obstruction of feedback connectivity may be a unifying mechanism underlying anesthetic induced unconsciousness.

Introduction

A cardinal feature of consciousness is the maintenance of a stable perceptual world. For the brain to accomplish this, sensory information must be faithfully relayed and integrated. In its corresponding primary sensory cortex, evoked sensory responses remain largely spared by anesthetic agents (Hubel and Wiesel, 1962; Imas et al., 2005b; Nourski et al., 2017; Sellers et al.,

2013). This suggests that anesthetic-induced perceptual breakdown occurs in higher order cortical networks

Anesthetic agents comprise a family of compounds that reliably produce loss of consciousness despite their structural heterogeneity (Eckenhoff and Eckenhoff, 1998; Franks, 2008; Hao et al., 2020; Hemmings et al., 2019; Kelz and Mashour, 2019; Lee, UnCheol and Mashour, 2018; LJ et al., 2019; Lydic Ralph and Baghdoyan Helen A., 2005; Platholi and Hemmings Jr, 2021). For example, some anesthetics tend to modulate GABA$_A$ receptors such as propofol and isoflurane (Ferron et al., 2009a; Hall et al., 1994; Jones and Harrison, 1993; Jurd et al., 2003; Krasowski et al., 1998a; Sonner et al., 2007), while others, such as ketamine act through NMDA and HCN antagonism (Chen et al., 2009; Yamamura et al., 1990; Zhou et al., 2018). However, most anesthetics have promiscuous binding with many other receptors throughout the nervous system (Alkire and Miller, 2005; Eckenhoff, 2002a). While significant strides have been made in understanding the molecular mechanisms of how anesthetics interact with their receptors and downstream effectors, distinguishing the critical in vivo neurophysiologic mechanisms through which anesthetics exert their desirable actions has proven more difficult. Many have attempted to understand the anesthetic state by examining the EEG patterns generated by different agents. For instance, propofol induces low frequency large amplitude EEG oscillations and sleep-like spindles (Ching et al., 2010; Purdon et al., 2013). Likewise, isoflurane produces slow wave activity with distinct UP-states and DOWN-states (Ferron et al., 2009a; Sonner et al., 2007). On the other hand, ketamine induces an "awake-like" EEG with pronounced gamma oscillations (Blain-Moraes et al., 2014; Maksimow et al., 2006). Since the induced spontaneous activity is also diverse across anesthetic agents, researchers have turned to network analysis to understand if anesthetics produce unconsciousness through a unified pathway.

It was once believed that anesthetic agents disrupt perception through the common suppression of the thalamus, leading to the prevention of ascending flow of sensory information. However, sensory evoked responses are readily recorded from primary cortices and may even be

locally enhanced by select anesthetics (Alkire and Miller, 2005; Hudetz and Imas, 2007; Imas et al., 2005b). Therefore, focus has turned towards understanding the network effects of the breakdown of higher order sensory processing and integration under anesthesia (Lee, UnCheol and Mashour, 2018). For example, in the visual system, anesthetics suppress integration of local receptive field information, as well as preferentially affect motion detection (Pack et al., 2001). In the auditory system, general anesthetics preferentially affect the neural mechanisms enabling identification of a global odd ball compared to local odd balls in pitch pattern detection (Nourski et al., 2017). Moreover, human functional connectivity studies also show that integration decreases and modularity increases during sleep, anesthesia and vegetative states (Achard et al., 2012; Monti et al., 2013; Rosanova et al., 2012; Tagliazucchi and Laufs, 2014). Similarly, multiple anesthetics, including the volatiles (Imas et al., 2005a; Ito et al., 2014; Lee et al., 2013b), propofol (Jordan et al., 2013; Lee et al., 2009; Liu et al., 2012) and ketamine (Blain-Moraes et al., 2014; Lee et al., 2013b) have been shown to preferentially disrupt feedback signaling from frontal to parietal areas, while maintaining feedforward signaling from primary sensory to parietal to frontal.

The studies establishing anesthetic-induced breakdown of neural integration is mostly derived from analyzing pairwise interactions between neural oscillations recorded from different brain regions. While this method can measure the influence of neural activity in one region on another, it is unable to capture the richness of stimulus-induced traveling waves that percolate across the cortical surface and through its laminar depths. Recently, we demonstrated simple visual stimuli in awake mice evoke a series of coupled neuronal oscillations over the cortical surface which forms two coherent traveling waves (Aggarwal et al., 2021). The fast (30-50Hz) waves begin in the primary visual cortex (V1) and travel anteriorly in a feedforward fashion. Slow (3-6Hz) waves originate in higher order areas and propagate posteriorly in a feedback manner. Moreover, the phase of the feedback wave modulates amplitude of feedforward wave and the firing patterns of individual neurons both in the association cortex and in V1, thereby forming a transient coordinated assembly throughout the cortex after stimulus presentation.

To rigorously assess the potential neurophysiologic significance of slow feedback and fast feedforward traveling waves, we hypothesized that delivery of hypnotic doses of mechanistically distinct general anesthetic drugs should impair these signals if they denote critical elements of perceptual encoding. We therefore performed high density surface and intraparenchymal electrocorticography (ECoG) recordings in mice during wakefulness or under isoflurane, ketamine, or propofol, to explore the how anesthesia affects the spatiotemporal properties of visual evoked fast (30-50Hz) feedforward and slow (3-6Hz) feedback waves that propagate through the awake brain (Aggarwal et al., 2021). We illustrate that simple visual stimuli evoke high frequency oscillations both within V1 and in higher order cortical areas in all mice, regardless of anesthetic state. However, several attributes of visual evoked fast feedforward waves are disrupted by the presence of anesthetics, including their single trial reliably, signal to noise, and spatial activation pattern, compared those observed in awake mice. Furthermore, under all tested anesthetics, visual stimuli fail to evoke large amplitude slow frequency oscillations that are coherent from trial to trial during wakefulness. Thus, visual evoked slow waves are rarely elicited, contain low signal to noise, and have high variability in spatial activation pattern in anesthetized animals. Finally, visual evoked slow waves observed in anesthetized animals resemble slow waves elicited in awake animals that are presented with weak stimuli. These results suggest that a shared mechanism underlying anesthetic induced unconsciousness might be obstructing feedback connectivity.

<u>Results</u>

In order to determine how mechanistically distinct anesthetics affect visual evoked activity, we performed high density *in vivo* electrophysiological recordings in awake and anesthetized head fixed mice (n = 32), receiving 10ms flashes of a green LED (Figure 4.1a). A 64 channel electrocorticography (ECoG) grid was placed over the dural surface of the contralateral (left) hemisphere in order to record local field potentials (LFPs) from the visual, association, retrosplenial, somatosensory, and motor/frontal areas. In a subset of animals (n = 14), two 32

channel laminar probes were also inserted within the cortical lamina through holes in the ECoG grid, targeting the primary visual cortex (V1) and the posterior parietal area (PPA). In these animals, the histological localizations of the laminar probes were used to determine the stereotaxic locations of ECoG electrodes and compare activation patterns across mice.

The mouse's anesthetic/behavioral state was parametrically altered by following one of two anesthetic delivery regimes (Methods, Figure 4.1b, Figure 4.2a, 1b). In the first regimen, the same animals (n = 25) were recorded during 0.6% isoflurane, wakefulness, and then during 100µg/g IP ketamine (Figure 4.2c). In the second group (n = 7), mice received 0.6% isoflurane and target controlled infusion dose of 20µg/g brain propofol (Figure 4.2d). All anesthetic doses were chosen to be in the hypnotic range (Ganguly et al., 2018; McKinstry-Wu et al., 2019).

Visual stimuli elicit high (30-50Hz) frequency activity within V1 when mice are awake or under anesthesia, but low (3-6Hz) frequency activity is diminished preferentially in anesthetized states

As prior research has demonstrated, (Aggarwal et al., 2019, 2021; Childers et al., 1987; Churchland et al., 2010; Churchland and Abbott, 2012; Liberati et al., 1991), simple visual stimuli elicit variable single trail LFP responses in V1 of both awake and anesthetized mice (Figure 4.1c, Figure 3.3a). However, when trials are averaged, a clear early component of the visual evoked potential (VEP) emerges, regardless of the animal's anesthetic/behavioral state (Figure 4.1c, Figure 4.3a). The consistency of the early visual evoked potential is highlighted by an increase in high (30-50Hz) frequency inter-trial phase coherence (ITPC) seen in the first 100ms of the VEP in awake mice, and in mice under isoflurane, ketamine, and propofol, compared to both pre-stimulus data (Figure 4.1d-e, Figure 4.3b-c). However, only the awake brain exhibits a strongly intertrial phase coherent slow (3-6Hz) oscillation that lingers long after stimulus onset (Figure 4.1d-e, Figure 4.3b-c).

The consistency of the early component and dissolution of the later component of the VEP is mirrored in the current source density (CSD) profile within the laminar structure of V1. In

all mice, regardless of anesthetic/behavioral state, there is a dependable early sink in the granular layer (layer 4), followed by subsequent sinks in supra- (layers 2/3) and infra- (layer 5) granular layers, within the first 100ms of the VEP (Figure 1f). However, when mice are awake, an alternating sink source pattern that is differentially organized across the layers of V1 continues for the next 300ms (Figure 4.1f). This is indicative of the faithful transfer of visual information from the visual thalamus to V1 that occurs both when mice are awake or under hypnotic doses of anesthesia (Douglas and Martin, 2004; Jones, 1985). When the same mice are anesthetized with isoflurane or ketamine, the later sink source pattern is diminished in amplitude (Figure 4.1f). This data also suggest that the early intracortical dynamics involved in visual processing (i.e, visual information transfer from the L4 to L2/3 and L5, and the generation of early fast frequency oscillations) are also preserved under hypnotic doses of anesthesia. However, the neural processes that allow for the generation of the later, visual evoked slow oscillation is specifically impaired by anesthetic agents.

Trial average VEPs can also be observed in higher order cortical areas in mice (Sup. Figure 3). During wakefulness, however, VEPs have higher amplitude, spread over larger distances in cortical space, and reverberate across time in contrast to VEPs in same individuals anesthetized with isoflurane or ketamine (Figure 4.4a). In accordance with the surface recordings, visual evoked CSD is also present within the cortical parenchyma of the Posterior Parietal Area (PPA) of individual mice (Figure 4.4b) and in the average of all mice (Figure 4.4c). Within the PPA, oscillatory visual evoked activity is primarily observed in the superficial lamina during wakefulness. This activity is diminished, but not eliminated, when the same mice are anesthetized (Figure 4.4b and c). Thus, visual evoked activity relays to both V1 and higher order cortical structures, even in the anesthetized brain.

Fast frequency activity is observed throughout many cortical areas, but the activity is highly variable across trials outside of V1 in anesthetized mice

Our previous work demonstrates that simple visual stimuli evoke a pair of traveling waves that span much of the cortical surface in awake mice: a fast (30-50Hz) feedforward wave, and a slow (3-6Hz) feedback wave (Aggarwal et al., 2021). To determine how anesthetic agents modulate the structure of these two visual evoked waves, we detail how evoked voltage in high frequency, low frequency, and ITPC are affected by anesthesia.

In both awake and anesthetized mice, the amplitude of visual evoked fast frequency oscillations, normalized to baseline activity, is increased within the first 350ms of stimulus onset both in V1 and secondary visual areas (Figure 4.5a). Notably, mice under isoflurane exhibit the highest total baseline normalized 30-50Hz amplitude (averaged over trials and ECoG electrodes), compared to awake mice, mice under ketamine, or propofol (p-value < 0.001; Kruskal Wallis; p-value = 0.042, Wilcoxon rank sum; Figure 4.6a). To quantify the spread and consistency of fast frequency evoked activity, we measured the fraction of VEP trials in which the 30-50Hz amplitude exceeded its baseline average by 5 standard deviations within 350ms of stimulus onset, for each ECoG electrode (Figure 4.5b). During wakefulness, V1 and higher order areas consistently display fast frequency VEPs over trials and mice. When the same mice are placed under isoflurane, fast frequency VEPs are consistently evoked across trials within V1 and some of V2. However, the variability of fast frequency VEPs presentation increases with distance from V1. Less consistent fast frequency VEPs are observed in mice under ketamine, both within and outside of V1 (Figure 4.5c). When averaging the consistency over electrodes, indeed, awake mice exhibit more fast frequency VEPs over the cortical surface, compared to mice under anesthesia (p-value <0.00001; Kruskal Wallis; p-value = 0.0006, Wilcoxon rank sum; Figure 4.6b). Over the cortical surface, the phase of the evoked fast frequency oscillations is more consistent across trials in awake mice as compared to the same animals under anesthesia (p-value <0.00001; Kruskal Wallis; p-value = 0.024, Wilcoxon rank sum; Figure 4.5c, Figure 4.6c). Thus, our findings suggest that processes generating visual evoked high frequency oscillations

remain intact, but the organization of visual evoked high frequency oscillations over the cortical surface is disrupted under general anesthesia.

Visual stimuli evoke long range slow frequency oscillations throughout cortical surface only in awake animals

We performed a similar set of analyses quantifying the total evoked amplitude, spread, and ITPC of visual evoked slow oscillations over the cortical surface in awake and anesthetized mice. Visual stimuli evoke significantly higher slow frequency amplitude in awake mice as compared to mice under isoflurane, ketamine, or propofol (p-value<0.00001, Kruskal Wallis; p-values = 0.0006, Wilcoxon rank sum, Figure 4.5d, Figure 4.7a). Likewise, in awake mice, visual stimuli evoke 3-6Hz VEPs more consistently over trials over and cortical space as compared to mice under anesthesia (p-value<0.00001, Kruskal Wallis; p-values = 0.0006, Wilcoxon rank sum, Figure 4.5e, Figure 4.7b). Finally, the phase of evoked slow frequency oscillations is more consistent across trials over much of the surface in awake mice compared anesthetized mice (p-value= 0.00001, Kruskal Wallis; p-value = 0.0024, Wilcoxon rank sum; Figure 4.5f , Figure 4.7c). Therefore, all three anesthetics greatly reduce visual evoked slow frequency activity and organization over the cortical surface, and consequently critically disrupt the generation and maintenance of visual evoked slow feedback waves observed in awake mice.

Travelling waves are observed in the average filtered LFP data in awake mice, but their amplitude and propagation pattern are disrupted under anesthesia

The average of single trial LFPs filtered at fast frequencies from electrodes along the anterior-posterior (AP) axis in a representative mouse (Figure 4.8a) show a coherent visual evoked fast feedforward wave that begins in posterior V1 and travels anteriorly when the animal is awake. However, when this same animal is under isoflurane, amplitude of the trial average activity is diminished. Since visual stimuli evoke higher fast frequency power in mice under isoflurane compared to wakefulness (Figure 4.3a, Figure 4.8a), the most likely rationale for the

low amplitude and disrupted structure of the trial average is the high variability in the phase of visual evoked 30-50Hz oscillations. Finally, when the same mouse is under ketamine, the spatial activation profile of the feedforward wave is distorted compared to that seen during wakefulness (Figure 4.8a).

In line with this view, the average of single trial LFPs filtered at slow frequencies from the same mouse in Figure 4.8a show a coherent visual evoked slow feedback wave that begins anterior to the feedforward wave initiation zone, in V2M, and travels posteriorly when the animal was awake (Figure 4.8b). However, when this same animal is under either isoflurane or ketamine, amplitude of the average filtered signal is greatly diminished.

The laminar structure of the fast feedforward waves is preserved in V1, but, the layer organization of fast and slow frequency oscillations are disrupted in PPA in mice under anesthesia

To determine how anesthetics affect the laminar organization of visual evoked fast and slow waves, we averaged the filtered CSD data at each depth within a different representative mouse. We find that the fast frequency oscillations originate in layer 4 in V1 and propagate to supra- and infra-granular layers (Figure 4.9a), regardless of state. This finding indicates that the thalamocortical and corticocortical circuitry necessary for the initiation and early intracolumnar propagation of the visual evoked fast oscillations remains intact under hypnotic doses of anesthesia (Figure 4.9b) (Reinhold et al., 2015b; Saleem et al., 2017). However, average visual evoked fast frequency oscillations are only seen in an organized fashion in the superficial layers of the PPA during wakefulness compared to under anesthesia. This suggests that the circuitry underlying the long-range propagation of fast oscillations within the PPA is specifically disrupted by hypnotic doses of anesthetics, even though local connections within V1 remain intact.

Visual evoked slow oscillations observed during wakefulness are predominantly present in the supragranular and granular layers of V1 and the superficial layers in PPA and propagate ventrally within the cortical column. However, the average slow frequency amplitude is diminished

throughout the cortical lamina in both regions when the same mice are under either isoflurane or ketamine.

Visual evoked spatiotemporal responses can be identified on a single trial basis using complex Singular Value Decomposition (SVD)

Previously, we utilized complex SVD of the analytical signal of filtered LFP data to identify visual evoked waves on a single trial level in awake mice (Aggarwal et al., 2021). Singular value decomposition (SVD) is a matrix factorization technique that decomposes spatiotemporal data into a set of mutually orthogonal modes:

$$\mathbf{A = USV^T}$$

where A is an n channels by t timepoint matrix of analytical signals, U is an n by n complex valued spatial matrix in which each column encodes the spatial phase and spatial amplitude of a single mode at each channel, V is a t by t complex valued temporal matrix in which each column encodes the instantaneous temporal phase and temporal amplitude of each mode at each time point, and S is an n by t diagonal real valued matrix which defines the fraction of the total signal variance described by each mode. Therefore, SVD may be able to extract stimulus evoked spatiotemporal patterns, herein referred to as waves, of activity from noisy single trial LFP data, which has a mix of spontaneous and evoked neural activity (Arieli et al., 1996; Kisley and Gerstein, 1999).

We performed SVD on the analytical signal of single trials filtered at fast and slow frequencies in mice. For each trial, we confined our analysis to the first ten modes that contained the majority of signal variance (accounting for $FastVar_{awake}$ = 63-81%, $FastVar_{Iso}$ = 66-85%, $FastVar_{Ket}$= 69-86%, $FastVar_{Prop}$ = 64-85% of the variance of LFP filtered at fast frequencies and $SlowVar_{awake}$ = 99.6-99.9%, $SlowVar_{Iso}$ = 99.6-99.9%, $SlowVar_{Ket}$= 99.7-99%, $SlowVar_{Prop}$ = 99.6-99.9% of the variance of LFP filtered at fast frequencies). This limitation protects against numerical instability present in lower rank modes, and the results were not affected by the

number of modes chosen to analyze. We identified an SVD mode as visually responsive if its temporal amplitude during the post-stimulus period exceeded the pre-stimulus temporal amplitude average by 6 standard deviations (Methods). Further, we define the most visually responsive mode on each trial as the mode in which the post-stimulus temporal amplitude is maximum, compared to pre-stimulus temporal amplitude.

Mechanistically distinct anesthetic agents disrupt different characteristics of fast frequency feedforward waves

To measure the reliability of visual evoked fast frequency traveling waves in anesthetized mice, we quantified the number of trials that contained at least one visually responsive mode. In awake mice, the vast majority of trials contain visually responsive modes (p-value <0.00001; Kruskal Wallis; p-value = 0.0006, Wilcoxon rank sum; Figure 4.10a, Figure 4.11b). When the same mice are anesthetized, the proportion of trials without any detected visually responsive modes increases (Figure 4.10a, Figure 4.11b). Moreover, when mice are under isoflurane, more trials contain at least one visually responsive modes compared to when mice are under ketamine or propofol (p-value <0.00001; Kruskal Wallis; p-value = 0.0006, Wilcoxon rank sum; Figure 4.10a, Figure 4.11b).

In awake mice, the most visually responsive mode is often associated with the first singular value (first rank from SVD), and thereby contains the highest amount of signal variance (p-value <0.00001; Kruskal Wallis; p-value = 0.0002, Wilcoxon rank sum; Figure 4.10b, Figure 4.11a). Interestingly, the most visually responsive mode is also likely to have the highest rank in mice under hypnotic doses of isoflurane; however, the skewness of the rank distribution is less than that found in awake animals (s_{awake} = 1.28, CI = 1.18-1.38; $s_{isoflurane}$ = 0.42, CI = 0.37-0.47; $s_{ketamine}$ = 0.15, CI = 0.08-0.22; $s_{propofol}$ = 0.22, CI = 0.10-0.34; Bootstrapped Pearson's moment coefficient of skewness). In addition, when mice are under ketamine or propofol, the most visually responsive mode is often not the first mode identified with SVD. This evidence suggests that in awake mice, visual stimuli elicit a high frequency global spatiotemporal response that has high

102

signal relevance, whereas under anesthesia, the response pattern is more likely dominated by spontaneous activity.

Visual stimuli consistently evoke fast frequency feedforward waves over the cortical surface across trials in awake mice

In awake mice, the spatial phase relationship of the most visually evoked high frequency mode was highly consistent across trials and animals (Aggarwal et al., 2021). To determine the consistency in the spatial phase relationship of fast oscillations, we computed the average difference in spatial phase of the most visually responsive mode from each channel to that of V1, across trials. The direction of the resultant vector corresponds to the average phase difference (colors in Figure 4.12a), whereas the magnitude corresponds to 1-variance in the coherence of the inter-site phase angle differences across trials (heat map in Figure 4.12b). Within V1, there is little variance between the spatial phase offset, regardless of whether or not the animal is anesthetized (Figure 4.12b and 4.12c). However, as distance from V1 increases, the variance in the phase offset across trials and animals increases at a steeper rate when mice are under isoflurane or ketamine, compared to when animals are awake (Figure 4.12b and 4.12d). The same pattern is observed when calculating the fraction of channels that have significant coherent phase offset from V1 across trials within each animal (Figure 4.12e, Figure 411c). In awake mice, the majority of the channels on the cortical surface contain a phase offset from V1 that is consistent across trials, however, when the same mice are under anesthesia, only about 20% of electrodes exhibit a consistent phase offset from V1 (p<0.00001, Kruskal Wallis, pairwise p= 0.0013, Rank Sum; Figure 4.12e, Figure 4.11c). Thus, under anesthesia, the consistency of the spatial phase relationship across trials breaks down.

In order to quantify how anesthetics alter the spatial phase progression of visual evoked fast oscillations, we quantified the average spatial phase gradient of the most visually responsive mode across trials and animals (Methods). The angle of the resultant average vector is the direction of phase progression, and the magnitude corresponds to 1-variance in the coherence of

this direction of spatial phase progression over trials and animals (shown as black arrows in Figure 4.12a). Within V1, the phase gradient progresses in the rostral, feedforward direction, regardless of the behavioral state. However, when animals are anesthetized, the consistency of the feedforward wave becomes weaker outside of V1, compared to awake animals (Figure 4.12a).

Finally, to determine if the same electrodes participate in visual evoked fast waves across trials, we computed the cosine similarity (defined as 1-cosine distance, Methods) of the spatial amplitude of the most visually responsive mode between pairs of single trials. We find the number of trials that have high cosine similarity to one another is higher when mice are awake than anesthetized. Similarly, the number of trials that have low cosine similarity (large cosine distance) is higher when animals are anesthetized compared to awake animals (Figure 4.11d, Figure 4.12f). The increase in consistency of the visual evoked spatial activation pattern across trials suggests that in the waking brain, similar brain regions might be recruited to process visual stimuli across trials. However, the dynamics present in the anesthetized brain may hinder the effective coordination of disparate brain regions necessary for signal processing.

Visual stimuli consistently evoke slow frequency feedback waves over the cortical surface in awake, but not in anesthetized mice

In awake mice, visual stimuli evoked slow feedback waves along with fast feedforward waves (Aggarwal et al., 2021). Under anesthesia, there is much less evoked slow frequency power and ITPC over the cortical surface (Figure 4.6, Figure 4.7). Therefore, we hypothesized that it is unlikely for visual stimuli to robustly elicit large scale visual evoked waves, in the anesthetized brain. To test this theory, we performed similar complex SVD analysis on the analytical signal of single trials filtered at slow frequencies and show in wakeful mice that visual evoked slow waves are much more reliably elicited ($p<0.0001$, Kruskal Wallis, pairwise $p<0.001$, Rank Sum), and the most visually responsive slow wave tends to be the first SVD ranked mode ($p<0.00001$, Kruskal Wallis, pairwise $p=0.0196$, Rank Sum) as compared to anesthetized mice

(Figure 4.13a and 4.13b). Moreover, the spatial activation profile of visual evoked slow waves is much more consistent across trials both in terms of spatial phase coherence (p<0.0001, Kruskal Wallis, pairwise p=0.0007, Rank Sum), and spatial amplitude, in awake animals compared to anesthetized animals (Figure 4.13c and 4.13d, Figure 4.14a-f). Further, the variance of the spatial phase consistency is much greater outside of V1 in mice under isoflurane and ketamine as compared to awake mice (Figure 4.14a-c). Finally, in awake mice, visual evoked slow waves propagate caudally, in the feedback direction over much of the cortical surface, mirroring the pattern seen in the average filtered LFP (Figure 4.8b, Figure 4.14a). In the same mice under isoflurane, the phase gradient vectors have divergent angles and small magnitudes, thereby suggesting higher variance in the spatial phase progression of slow oscillations over trials (Figure 4.14a). When mice are under ketamine, the phase gradient vectors within V1 are longer than those found under isoflurane and the vector angles target both V2L in the feedforward direction, and posterior V1, thereby indicating that the coherent feedback pattern of awake slow waves is distorted under ketamine (Figure 4.14a).

Visual evoked slow waves under anesthesia resemble slow waves elicited from low luminance stimuli

Weaker visual stimuli presented as full field luminance changes on a screen also elicit spatiotemporal VEPs in the fast and slow frequency ranges, regardless of anesthetic state. In both awake and anesthetized mice, visual evoke fast feedforward waves are spatially contained within V1, regardless of stimulus intensity (Figure 4.15a-c). In contrast, visual evoked slow feedback waves tracked stimulus intensity only in awake mice (Figure 4.16a). Specifically, slow frequency feedback waves were predominantly observed in V1 for the lowest luminance stimulus, but they extended over more of the cortical surface for higher luminance stimuli (Figure 4.16a). Interestingly, the visual evoked slow waves observed in mice under isoflurane or ketamine resembled slow visual evoked waves in awake mice presented with the smallest screen luminance (Figure 4.16b, and 4.16c). Thus, visual evoked slow waves observed in mice under

hypnotic anesthesia have the same spatiotemporal dynamics as slow waves evoked from weak visual stimuli.

Discussion

Using a rigorous neurophysiological characterization spanning the almost a complete hemisphere as well as laminar recordings through V1 and the PPA, we demonstrate that unlike visual stimuli presented during wakefulness, visual stimuli fail to evoke coherent, large amplitude slow frequency oscillations in the same animals exposed to a hypnotic dose of any tested anesthetic. Analysis of individual trials finds that visual evoked slow waves under anesthesia are not reliably elicited, contain low signal to noise, and have variable spatial activation patterns and phase gradients, compared to those observed in awake animals. Finally, the visual evoked slow waves identified in anesthetized animals resemble visual evoked slow waves elicited in awake animals that are presented with weak stimuli. During exposure to hypnotic doses of isoflurane, propofol, or ketamine, simple visual stimuli readily evoke high frequency oscillations throughout the cortical surface. Fast oscillations within V1 lamina begin in the granular layer and then relay to the supra- and infra-granular layers, in all mice, regardless of arousal state. However, large scale visual evoked fast waves are not reliably evoked or have high signal to noise, in anesthetized animals as compared to waking ones. Moreover, on a trial-by-trial basis, the spread and spatial phase gradient of visual evoked fast feedforward waves are highly variable outside of V1 compared to evoked fast waves detected during wakefulness. Our detailed neurophysiologic results emphasize a shared mechanism by which general anesthetics disrupt sensory processing through blocking feedback connectivity.

Feedforward distortion vs feedback breakdown under anesthesia

We described the visual evoked waves observed in the awake brain as feedback and feedforward given their sites of initiation and their direction of propagation: the fast frequency

106

feedforward wave initiates in posterior V1 and travels rostrally whereas the slow frequency feedback wave begins in higher order cortical areas and travels caudally (Figure 4.8). The patterns of these waves also match the presumed function of feedforward feedback visual processes. Feedforward signaling is thought to mediate the hierarchical formation of abstract concepts in higher order areas from simple receptive fields in V1. Feedback processing, conversely, is thought to mediate the top-down modulation of primary and secondary cortical areas from higher order processing centers (Felleman and Van Essen, 1991; Markov et al., 2014). Several lines of evidence have supported the notion that feedback processing is disrupted while feedforward processing is maintained during states of unconsciousness (Boly et al., 2011; Hudetz, 2009; Imas et al., 2005a; Ku et al., 2011; Lee, UnCheol and Mashour, 2018; Mashour, 2014; Mashour and Hudetz, 2017; Shushruth, 2013).

Previous studies dissecting anesthetic effects on feedforward feedback connectivity have analyzed pairwise activity patterns measured at different cortical areas. While such methods can measure the influence of the neural activity in one region onto another, the analysis of pairwise correlations is unable to capture coherent traveling waves that percolate across and through the depths of the cortical surface. Moreover, previous work relied on spontaneous EEG activity in humans, in which the direction of connectivity was not temporally related to stimuli, and therefore the function of this connectivity was not known (Boly et al., 2011; Ku et al., 2011; Lee et al., 2009). Nevertheless, prior research using spontaneous human data consistently points to a common translational relevance of our murine findings (Ku et al., 2011; Lee, UnCheol and Mashour, 2018; Lee et al., 2009; Mashour, 2014; Mashour and Hudetz, 2017). By recording high density ECoG nearly spanning a full mouse hemisphere during visual stimulation and analyzing data with SVD, a tool beneficial for finding spatiotemporal relationships, we demonstrate that distinct anesthetics disrupt the coordinated waves of visual evoked neural activity across multiple brain regions. Moreover, by pairing surface and depth recordings together, we begin to describe how the three-dimensional propagation pattern of visual evoked waves is influenced by anesthetic state.

We show that coordinated visual evoked feedback activity is nearly abolished by each anesthetic. Coordinated feedforward activity, on the other hand, is differentially altered by anesthetic agents. For example, evoked total high frequency power is greatest when mice are under isoflurane and visual evoked high frequency ITPC is the lowest when mice are under propofol. Likewise, visual stimuli are more likely to evoke high signal to noise activation patterns when animals are under isoflurane compared to when animals are under ketamine and propofol. Our findings therefore suggest that the tested anesthetics interact with circuits involved in visual feedforward processing in different ways. This could come at the level of excitation-inhibition neural firing patterns, neuromodulatory drive, and/or interactions with arousal circuitry (Cardin, 2016b; Ermentrout and Kleinfeld, 2001; Friston and Buzsáki, 2016; Kopell et al., 2000; Lee et al., 2014; Pinto et al., 2013; Sohal et al., 2009; Traub et al., 1996, 2016b; Vinck et al., 2015; Wang and Buzsáki, 1996; Whittington et al., 2000; Wilson and Cowan, 1972). Finally, the sum of the effects that anesthetics have on visual evoked feedforward feedback waves in mice mirrors the disruption of cortical communication observed in human EEG, in which evoked activity in the anesthetized brain is shorter lived and curtailed in space compared to that observed during wakefulness (Casali et al., 2013; Ferrarelli et al., 2010; Massimini et al., 2005).

The pattern of loss of feedback connectivity during states of unconsciousness has also been noted at the level of evoked potentials. Specifically, loss of consciousness is associated with the disappearance of the late phase, but preservation of the early phase of evoked potentials evoked (Del Cul et al., 2007; Ferrarelli et al., 2010; Hudetz et al., 2009). Similarly, we show that the late phase of VEPs, even within V1, is specifically sensitive to isoflurane, ketamine and propofol (Figure 4.1, Figure 4.3). However, the early visual evoked fast oscillations are maintained, especially within V1 (Figure 4.9). Thus, aspects of the early evoked visual response such as signaling from the thalamus to the primary cortex and onward are relatively spared, but the later response, which is associated with the slow feedback wave, is disrupted by anesthetic agents.

Luminance dependence of slow wave generation

One interesting observation is that there is a step function increase in spatial phase consistency over trials of slow feedback waves evoked from the two weakest stimuli presented in awake mice (Figure 4.16a). Slow feedback waves were seen mostly in V1 for the weakest stimulus, 2% of maximum screen brightness, but they extended across the cortical surface for stimuli with brightness at or above 11% of maximum screen brightness (Figure 4.16a). Remarkably, slow waves elicited from the flashes of maximum screen brightness or even the LED in mice under isoflurane or ketamine resemble the curtailed pattern of slow waves evoked from the weakest stimulus presented awake mice (Figure 4.16b, and 4.16c). While directly determining the luminance threshold for perceptual detection in our animals was beyond the scope of the present study, several lines of evidence suggest the murine threshold for visual perception falls between our experimental 2% stimulus and our 11% stimulus. The weakest stimulus has a measured luminance of $1.5cd/mm^2$, which is in the mesopic, or intermediate luminance conditions in which both rods and cones are active. All other stimuli are within the photopic ($>3cd/mm^2$) range, in which cones relay the majority of visual information (Denman et al., 2018; Wysocki and Stiles, 1982). Thus, the results we present may be due to the mouse only perceiving photopic stimuli, given the fast interstimulus interval between a series mostly phototopic visual stimuli and insufficient dark adaptation (Alam et al., 2015; Peirson et al., 2018). Alternatively, visual evoked slow waves might be generated only with stimuli that strongly cones within the retina, thus implying that anesthetics may be affecting visual processing beginning at the retina (Alam et al., 2015; Peirson et al., 2018).

Implications of dosing and behavior

Anesthetics disrupt specific attributes of visual evoked fast feedforward waves in an agent-specific manner, but commonly thwart the propagation of visual-evoked slow feedback waves that is observed in awake mice. Whether the feedforward and feedback waves are necessary for visual processing into conscious perception remains unknown. To determine the behavioral significance of traveling waves, one must train mice to report when they saw the stimulus. This

task becomes considerably more complicated to interpret in animals under low doses of anesthesia, given the potential confound that an animal's motivation to complete the task might decrease even though it may perceive the visual stimulus. The doses of anesthetics used in this experiment were targeted to be hypnotic, and therefore allow for loss of consciousness while avoiding deep general anesthesia. At 0.6% steady state isoflurane, approximately 44% of mice lost their righting reflex, the gold standard for testing for loss of unresponsiveness in rodents, on a given trial (McKinstry-Wu et al., 2019). Moreover, since the TCI dosing method for targeting brain concentration of propofol in mice is new, behavioral assays determining the responsiveness level of mice at 20 ug/g brain concentration of propofol is unknown (Shortal et al., 2018). We targeted this dose in order to reproducibly induce slow waves seen in the LFP, similar to those seen in mice under 0.6% isoflurane. Finally, understanding the ketamine dosing on behavior is also complicated given the pharmacokinetics and pharmacodynamics of intraperitoneal ketamine. At 100mg/kg, ketamine induces sedation mice in which rigid spontaneous movements are common (Ganguly et al., 2018; Vesuna et al., 2020). Mice at this dose however lose their righting reflex for an average time of 6 minutes (Ganguly et al., 2018). Thus, a drawback of targeting low doses of anesthesia is the chance of animals regaining consciousness on a subset of trials or experiments. To this point, a reoccurring finding in our analysis is that the average slow wave amplitude in anesthetized mice is considerably lower than the average slow wave amplitude discovered during wakefulness. It is possible that this low amplitude might arise from mice being able to effectively process the visual stimulus on some trials but not others.

Increase VEP variability under anesthesia

One of the common themes in this study is an increase in the variability of VEPs when mice are under anesthesia compared to during wakefulness. This phenomenon is observed in the decrease in ITPC of fast and slow visual evoked oscillations over the cortical surface (Figure 4.5 and 4.7, Figure 4.8), and an increase in variability of spatial activation pattern and spatial phase relationships from trial to trials of visual evoked fast and slow waves (Figure 4.11 through 4.14)

This high variability might arise from the dynamical systems theory that anesthetics induce highly stable network dynamics in which small perturbations dampen quickly and brain activity resembles ongoing spontaneous activity. In the awake brain, conversely, the network dynamics may be close to critical and therefore brain activity may be more susceptible to changes by stimulus perturbation. Consistent with this, stability analysis of ECoG recordings from monkeys under ketamine or propofol anesthesia exhibit stable dynamics whereas that of awake monkeys reveal critical dynamics (Solovey et al., 2015). A fascinating future direction would be to understand how the stability of post-stimulus activity is affected by anesthetic state. Our data would suggest that stimulus evoked dynamics might be more stable in the waking state compared under anesthesia, since awake VEPs are spatiotemporally coherent from trial to trial.

Conclusion

Here, we show that coordinated visual evoked slow feedback waves are largely abolished by all anesthetics tested, but attributes of visual evoked fast feedforward waves are disrupted in a drug specific manner. While the behavioral relevance and circuit mechanisms underlying the generation, maintenance, and breakdown of these waves are up for future directions, the fact that all three mechanistically distinct anesthetics similarly break down feedback waves may give way to a common neural correlate of anesthetic induced loss of consciousness.

<u>Methods</u>

Animals: All experiments in this study were approved by Institutional Animal Care and Use Committee at the University of Pennsylvania and were conducted in accordance with the National Institutes of Health guidelines. Experiments were performed using 32 adult (12–32 weeks old, 20–30 g, 21 male and 11 female) C57BL/6 mice (Jackson Laboratories). Mice were housed under a reverse 12:12 h, light: dark cycle, and were provided with food and water ad libitum. Inclusion criteria for mice included the following: 1) presence of visual-evoked activity in which the absolute value of the first 100 ms of post-stimulus activity exceeds five standard deviations of pre-stimulus

activity and 2) presence of spontaneous activity that was not characterized as burst suppression at low anesthetic doses. Mice were divided into two anesthetic delivery cohorts: isoflurane/ketamine/awake (25 mice), and isoflurane/propofol (7 mice).

Headplate implantation, habituation, and craniotomy for Awake-Isoflurane-Ketamine: Headplate implantation, mouse habitation and craniotomy for mice performing isoflurane, ketamine, and awake recordings followed protocols described in Aggarwal et al, 2021 (Aggarwal et al., 2021). Briefly, mice were anesthetized with 2.5% and maintained with 1.5% isoflurane, and secured a stereotaxic frame (Narishege). Periosteum was exposed and bregma, lambda, and the site of the future craniotomy were marked (+1mm to -5 mm AP, +0.25 mm to +6 mm ML of bregma) on the left hemisphere. The skull was then scored and a custom designed headpiece was secured with dental cement (Metabond), cyanoacrylate adhesive (Loctite 495), and 3 skull screws (Fine Science Tools, Self tapping skull screws, 19010-10). Mice received 0.5mg cefazolin, 0.125mg meloxicam, and 7 ml of normal saline SQ post operatively, and recovered for one week. Then, mice were habituated to head fixation with body restraint with visual stimuli during one 45-minute session per day over the course of 4 days.

After completing the habitation protocol, mice were ready for recordings. Animals were anesthetized with 2.5% isoflurane in oxygen, secured onto the stereotax and maintained at 1.5% isoflurane. Before surgery, local anesthesia was injected subcutaneously in the face, scalp and neck muscles, targeting the trigeminal and occipital nerves (0.625 mg bupivacaine, 0.025%)(Osborn and Sebeo, 2010). Analgesia was supplemented with subcutaneous injection of 0.125mg meloxicam. To reduce potential swelling, 0.006mg dexamethasone was also injected subcutaneously before surgery. A 4 mm ML by 6 mm AP craniotomy was then drilled through the dental cement along the markings. A bone screw (Fine Science Tools, Self tapping skull screws, 19010-10) on the right skull bone (+2mm ML, -2mm AP) was used for a reference. A 64-electrode surface grid (E64-500-20-60, Neuronexus) was positioned over the dura (right most electrode anterior electrode at ~ 1mm lateral and 1mm posterior to bregma).

112

In 14 animals, two DiI coated (Sigma-Aldrich) laminar 32 channel probes (H4, Cambridge Neurotech) were also inserted 800um into the cortex. One targeted a hole in the ECoG grid closest to V1 (-3.25 AP, -2.25 ML). The other targeted a hole in the ECoG grid closest to PPA (-1.5 AP, -1.5 ML). Both were placed using a motorized micromanipulator (NewScale Technologies). The grid and exposed dura were then covered with gel foam soaked in mineral oil to prevent desiccation. Upon completing recordings, animals were deeply anesthetized (5% isoflurane) and sacrificed. Brains were extracted and fixed in 4% paraformaldehyde (PFA) overnight prior to sectioning and histology.

Anesthetic delivery protocol for Awake/Isoflurane/Ketamine experiments: After ECoG electrodes were positioned, animals were ready for electrophysiology recording. Isoflurane/awake/ketamine mice were first given 0.6% isoflurane through a nose cone and presented visual stimuli. Isoflurane was then turned off for 30 minutes before awake recordings with visual stimuli began. After awake recordings concluded, mice were re-induced with a transient 2 minute inhalation of 2.5% isoflurane to allow for accurate administration of 100mg/kg IP ketamine. Visual stimulation and recording under ketamine anesthesia began 2 minutes after ketamine administration.

Isoflurane Propofol Acute Surgery: Acute surgeries for animals receiving only isoflurane and propofol were performed as described in Aggarwal, et al 2019 (Aggarwal et al., 2019). Briefly, animals were induced with 2.5% isoflurane in oxygen, and maintained at 1.5% isoflurane with closed loop temperature control (37 ± 0.5 degrees C) for the remainder of the surgery and electrophysiological recording. A jugular venous catheter was placed to allow for Targeted Controlled Infusion (TCI) propofol infusion (Shortal et al., 2018). Animals were then secured into a stereotaxic frame (Kopf), where a craniotomy was drilled over the left hemisphere (+1mm to -5 mm AP, +0.25 mm to +6 mm ML of bregma), and a reference screw (Fine Science Tools, Self tapping skull screws, 19010-10) was secured in the right skull bone (+1mm AP, +1mm ML of bregma). A 64-electrode surface grid (Neuronexus: E64-500-20-60) was positioned over the dura

such that the most anterolateral electrode was approximately 1mm lateral 1mm posterior to bregma.

Anesthetic delivery protocol for Isoflurane/Propofol experiments: Animals receiving isoflurane and propofol underwent the same anesthesia delivery protocol as described in Aggarwal, et al 2019 (Aggarwal et al., 2019). Briefly, after jugular line was placed, craniotomy was drilled, and electrodes were positioned, animals were first given 0.6% isoflurane (Terrell Isoflurane, Novaplus) in 100% oxygen through a nose cone during visual stimulation. Then, TCI of propofol (1000mg per 100ml Diprivan, Fresenius Kabi USA) was set to produce 20 mg propofol / g brain levels exactly as described in Shortal et. al, 2018 (Shortal et al., 2018). To allow for isoflurane wash out, mice were equilibrated with steady state propofol for 15 minutes before visual stimulation began. Animals were sacrificed immediately after the final visual recording session.

Histology: Brains from the 14 animals in which laminar probes were inserted, were sectioned at 80μm on a vibratome (Leica Microsystems). Sections were mounted with a medium containing a DAPI counterstain (Vector Laboratories) and imaged with an epifluorescence microscopy (Olympus BX41) at 4x magnification.

Visual Stimulation: Two sets of visual stimuli were used in the study. The first consisted of 100 trials of 10 ms flashes of a green LED (650 cd/m^2) delivered at a random interstimulus interval drawn from a uniform distribution between 3 to 4 seconds. The flash covered 100% of the mouse's visual field. In 17 animals, a second class of visual stimuli were presented. These consisted of 240 trials of 100ms full flashes of a CRT monitor (Dell M770, refresh rate 60 Hz, maximum luminance 75 cd/m^2), placed 23 cm away at an angle of 60% from the mouse's nose, thereby covering 70% of the mouse's right field of view. The monitor full field flashes varied in luminance's (2%, 11%, 25%, 44%, 75%, 100%) in random order at a random interstimulus time interval between 3 and 5 seconds.

Electrode registration: The stereotaxic locations of the laminar probes were determined using post-mortem histology by comparison to the brain atlas (Franklin, Keith, B. and Paxinos, 2007).The position of the laminar probes in the electrode coordinate system was established by identifying the through holes the probes entered. The rotation of the grid about the AP axis was established by computing the cosine of the angle (θ) between the distance between the laminar probe in the electrode and stereotaxic coordinate system. The ECoG electrodes were assigned locations based on the Euclidean distance from the probes. The resultant ECoG locations were then multiplied to a rotation matrix (R) to account for grid rotation.

$$R = \begin{bmatrix} cos\theta & -sin\theta \\ sin\theta & cos\theta \end{bmatrix}$$

The resulting ECoG coordinates were then compared to photographs of the ECoG grid relative to bregma and lambda in order to verify locations.

Electrophysiology and preprocessing: In 6 mice, signals were amplified via a Neuralynx headstage (HS36), digitized with a Cheetah 64 acquisition system (Neuralynx, ERP-27, Lynx-8), and collected at a rate of 3030.3Hz/channel. In the remaining mice, signals were amplified and digitized on an Intan headstage (Intan, RHD2132) connected to an Omniplex acquisition system (Plexon, Omniplex), and collected a sampling rate of 40KHz/channel.

To extract LFP, data were downsampled to 1KHz and filtered between 0.1 Hz and 325 Hz, with the MATLAB functions, *firls.m* and *filtfilt.m* to minimize phase distortion. Channels with line noise and trials with excess movement were manually rejected. The mean signal across electrodes was subtracted from the LFP to minimize volume conduction. All subsequent analysis was performed using custom built Matlab (Mathworks) code, unless otherwise stated.

Selection of electrode over Primary Visual Cortex (V1): In 18 mice, laminar probes were not inserted and therefore grid electrodes were not aligned to stereotaxic coordinates. In these mice, the V1 electrode was identified neurophysiologically (Aggarwal et al., 2019, 2021). The latency of

onset of the visual-evoked potential was calculated for each ECoG electrode as the time point at which the post-stimulus average LFP exceeded 3 standard deviations above the pre-stimulus baseline for 3 consecutive time points. The electrode which had the lowest latency of onset was denoted as V1.

In the 14 mice in which laminar probes were inserted and the stereotaxic positions of the ECoG probes were inferred, the electrode closest to stereotaxic V1 (-3.25 AP, -2.25 ML) was chosen for each animal. To confirm that the chosen electrode neurophysiologically corresponded to V1, the latency of onset of the VEP at each grid electrode was also computed in the same manner as for the mice without laminar probe recordings. The position of the stereotaxically identified V1 electrodes was within 1-2 electrodes (<1000um) in distance and the onset was within 2 ms of the electrode with the earliest latency of onset in all mice.

Current Source Density Analysis (CSD): LFP from the laminar probes was converted in CSD by computing the second spatial derivative (Freeman and Nicholson, 1974):

$$\frac{d^2\varphi}{dz^2} = \frac{-[\varphi(z + 2\Delta z) - 2\varphi(z) + \varphi(z - 2\Delta z)]}{(2\Delta z)^2}$$

where φ is the LFP, z is the vertical coordinate depth of the probe, and Δz is the interelectrode distance (25 μm). Estimation of the CSD at the boundary electrodes was projected using the Vaknin estimation procedure (Vaknin et al., 1988). Channels with the earliest current sink in the V1 probe were assigned as layer 4 (granular layer). Subsequent sinks were found above and below layer 4 in layers 2/3 and layer 5 of the V1 probe. The channels of the PPA probe were assigned a laminar structure based on their distance from the cortical surface - channels within the first 350 mm of the surface (where the CSD converged to zero) were identified as the most superficial 4 layers, based on thickness (Franklin, Keith, B. and Paxinos, 2007; Lein et al., 2007b; Reference Atlas :: Allen Brain Atlas: Mouse Brain). Channels within the following 400 μm of parenchyma were identified to be within deep layers. Laminar data

was only included in analysis if the channels could clearly be assigned to layers in this manner (resulting in 11 out of 14 mice).

Wavelet analysis: Power, phase, and frequency characteristics were extracted from LFP or CSD by performing a continuous wavelet transform with Morlet wavelets with *contwt.m* (0.1 Hz to 150 Hz, with a step-width 0.25 Hz and normalized amplitude) (available at: http://paos.colorado.edu/research/wavelets/) (Torrence and Compo, 1998).

Inter-trial Phase Coherence (ITPC) Analysis: Inter-trial phase coherence (ITPC) was used to quantify the degree of phase synchrony between trials in time- frequency space. Briefly, the phase of each oscillation at each timepoint was extracted from wavelet coefficients and projected onto a unit circle by applying Euler's formula. The magnitude of the mean of the angle vector across trials corresponds to ITPC. (Cohen, Mike, 2014)

ITPC in Figure 4.7c and 4.8c were calculated by averaging the ITPC at each stereotaxic location over animals and over the first 100ms of the signal between 30-50Hz, or over the first 800ms of the signal between 3-6Hz, respectively.

Filtering data for wave analysis: LFP or CSD data was filtered into high (30-50Hz) or low (3-6Hz) using the inverse wavelet transform, *invcwt.m*, (available at: http://paos.colorado.edu/research/wavelets/) (Torrence and Compo, 1998). All wavelet coefficients outside the desired frequency band were set to zero.

Hilbert transform was used to derive the analytical signal of LFPs or CSDs filtered for high (30-50Hz) or low (3-6Hz) frequencies. This produced a time series of complex numbers, in which the modulus of the analytical signal corresponds to the instantaneous amplitude and the arctan of the analytical signal corresponds to the instantaneous phase.

Spread of filtered VEPs: Each single trial was filtered at 50-30Hz or 3-6Hz and its amplitude was extracted using the Hilbert Transform. The post-stimulus amplitude was then normalized to the

mean and standard deviation of 500ms of pre-stimulus amplitude on a single trial basis. At each

ECoG channel, trials were defined to have a 30-50Hz VEP if within the 350ms of stimulus onset,

the post-stimulus amplitude exceeded its baseline by 5 standard deviations. Trials were defined

to have a 3-6Hz VEP if within 1000 of stimulus onset, the post-stimulus amplitude exceeded its

prestimulus baseline average by 3 standard deviations. The fraction of trials containing filtered

VEPs was calculated for each electrode in each mouse to demonstrate the spread and

consistency of filtered VEPs. In Figures 2b and 3b, the fraction of trials containing filtered VEPs

were averaged at each stereotaxic location across animals. In Figure 4.6, the fraction of trials

containing filtered VEPs were averaged across mice.

Complex Singular Value Decomposition (SVD): Detailed methods and examples

describing complex SVD analysis of filtered LFP can be found in Aggarwal et. al., 2021 (Aggarwal

et al., 2021). Briefly, the Hilbert Transform was used on single trial, filtered LFP from ECoG

electrodes (containing 500ms of pre-stimulus and 1000 ms of post-stimulus activity) to derive

analytical signal matrix **A**. Oscillatory modes were extracted from A by performing singular value

decomposition, which factorizes A into mutually orthogonal modes:

$$\mathbf{A} = \mathbf{USV^T}$$

the spatial and temporal components of each mode, respectively. The diagonal real-valued S

contains singular values ($\lambda's$) and corresponds to the fraction of the total variance explained by

each mode.

The spatial amplitude and spatial phase of the $i - th$ mode is computed from calculating the

modulus and arctan of $U_{(*,i)} * \lambda_i$. Similarly, the temporal amplitude and temporal phase are

computed from calculating the modulus and arctan of $V_{(*,i)} * \lambda_i$.

Reliability of visually responsive modes: The temporal amplitudes of the first ten singular modes

were computed for each single trial, as above, and then normalized to their mean and standard

deviation of 400 ms of pre-stimulus activity. Modes in which the normalized temporal amplitude exceeded 6 standard deviation above pre-stimulus activity within the post-stimulus period (defined as 350ms post-stimulus for 30-50Hz activity and 1000ms post-stimulus for 3-6Hz activity), were defined as visually responsive modes. The fraction of trials in which at least one visually responsive mode was detected in each mouse, under each condition is shown in Figure 4.10a, Figures 4.11b and 4.13b.

Defining the most visually responsive mode: The mode that displayed the greatest increase in temporal amplitude during the post-stimulus period (defined as 350ms post-stimulus for 30-50Hz activity and 1000ms post-stimulus for 3-6Hz activity) compared to pre-stimulus activity, was defined as the most visually responsive mode.

Consistency of Spatial Amplitude Loading: To determine the similarity in the spatial activation of the most visually evoked modes across trials, the cosine distance of the spatial amplitude of the most visually evoked mode was computed interactively between pairs of single trials, within each mouse in each condition. Subsequently, the probability density function (PDF) of the cosine similarity (1-cosine distance) was computed for all pairs of trials across all mice for each anesthetic/behavioral state. In Figures 4.12 through 4.14, the PDF of the cosine similarity of spatial amplitudes in mice under anesthesia is subtracted from the PDF of the cosine similarity of spatial amplitudes in awake mice.

Spatial phase offset from V1: For each single trial, the phase offset from V1 was computed by extracting the spatial phase of the most visually responsive mode at each electrode and projecting it onto a unit circle. To find the average angle and consistency of each channel's phase offset relative to V1, the circular mean was computed across trials within each animal (Fisher, N, 1995). The direction of the mean vector corresponds to the angle of phase offset whereas the magnitude of corresponds to 1-variance.

119

In the 14 animals in which ECoG electrode stereotaxic positions were identified, the circular mean and variance were computed across trials and animals at each stereotaxic location in order to determine the consistency of the phase relationship across mice.

Spatial phase gradient: Using *phase_gradient_complex_multiplication.m*, written by Lyle Muller (available at: https://github.com/mullerlab/wave-matlab), the spatial phase gradient was calculated on a single trial basis by iteratively multiplying the complex valued spatial component of the most sensory evoked mode at one electrode location to the complex conjugate of the spatial component of the next electrode in the medial-lateral and anterior-posterior directions (Muller et al., 2014). The average gradient over trials was calculated by projecting each trial's gradient vector at each position onto a unit circle and computing the circular mean. The angle of the resultant vector corresponds to the direction of spatial phase advancement, whereas the magnitude of the resultant vector corresponds to 1-variance in the direction of the gradient over trials.

Averaging stereotaxic coordinates over animals: A query set of stereotaxic locations was defined from -5 to 0 mm AP and -3.5 to 0 mm ML, with 0.5mm spacing. The weight of each electrode at each query site was assumed to be Gaussian function of the distance between the electrode and the query location, as described in the following equation:

$$W = \frac{1}{\sigma\sqrt{2\pi}} e^{\frac{||p_q||}{\sigma}}$$

Where pq is the Euclidean distance between the electrode p and query location q, = 0.15 is the standard deviation. For all electrodes within 0.3 mm of the query position, the weight was determined as in the preceding equation, and was set to zero otherwise. When calculating averages and variances among mice as a function of stereotaxic coordinates, this weighting was employed.

Statistical Analysis: To determine the significance of the ITPC at each query location, the observed ITPC were compared to time shifted surrogates (n = 100 sets, 100 trials per set), using a one tailed t-test. A Stouffer's Z-score was computed and the resulting p-values were Bonferroni corrected for multiple comparisons (77 query stereotaxic locations) to the combine data across mice.

To determine the effects of arousal state on the visual evoked power, spread of filtered VEPs, total ITPC over the cortical surface, reliability of visually evoked modes, SVD rank of most visually evoked mode, and consistency in phase offset from V1 of most visually responsive mode, a Kruskal Wallis test was first performed. If there was a statistically significant effect of arousal state, pairwise Wilcoxon rank sum tests were performed, and resulting p-values were Bonferroni corrected for multiple comparisons (6 pairwise arousal states).

To determine if the spatial phase relationships and spatial phase gradients at each location were significant, a Rayleigh test for deviation from circular uniformity was performed. The resulting p-values were Bonferroni corrected for multiple comparisons (64 ECoG channels within individual mice, 77 query stereotaxic locations for aggregating across mice).

Presentation of previously printed figures: Awake data in Figures 4.1 through 4.14 have been presented in Aggarwal et. al, 2021 (Aggarwal et al., 2021). The figures are reproduced in the current manuscript in order to highlight the distinct effects that anesthetics have on visual evoked waves of cortical activity.
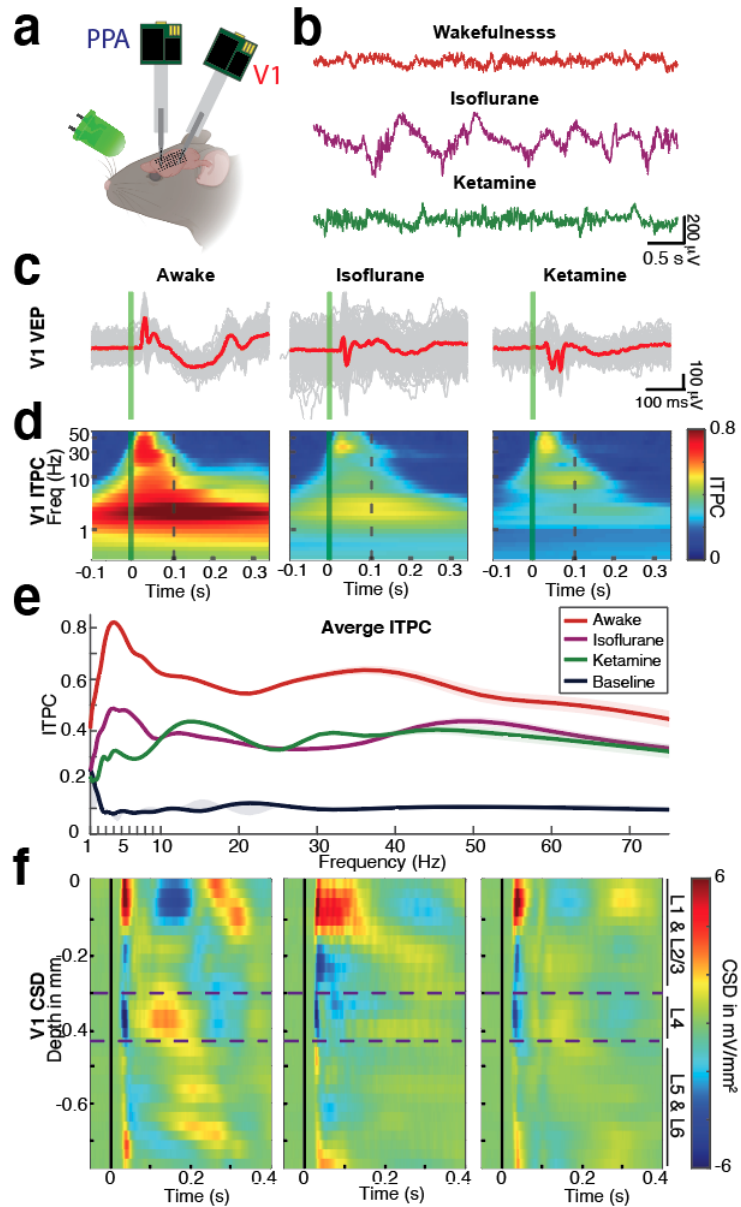
Figure 4.1: Visual stimuli elicit strong VEPS in V1 when animals are awake or under anesthesia

(A) Experimental design: 64 channel electrocorticography (ECoG) grid used to record local field potentials (LFPs) from the cortical surface of the left hemisphere of 32 awake mice. In 14 mice, 32 channel laminar probes were placed in the primary visual cortex (V1) and

the Posterior Parietal Area (PPA). Stimuli consisted of 10ms flashes from a green LED placed in front of the right eye.

(B) Five seconds of LFP traces of spontaneous activity at the V1 electrode in awake mice (top), or the same animal under isoflurane (middle), or under ketamine (bottom).

(C) Single trial (gray) and average (red) visual evoked potentials (VEPs) from a representative mouse during wakefulness (left), under isoflurane (middle), and under ketamine (right). The vertical green line denotes stimulus onset.

(D) Intertrial phase coherence at the V1 electrode averaged over animals during wakefulness (left), under isoflurane (middle), or under ketamine (right). The vertical green line denotes stimulus onset. The vertical dashed line marks the end of the 100ms epoch over which the average ITPC was calculated for each condition.

(E) Average ITPC over the first 100ms of the VEP at V1 in mice during wakefulness (orange), under isoflurane (purple), or under ketamine anesthesia (green). The baseline ITPC (calculated 800-900ms before stimulus onset) in awake mice is shown in black. The 95% confidence intervals around the mean are indicated by the shading.

(F) Current source density (CSD) of LFP averaged over mice from laminar electrode arrays placed in V1 in animals that are awake (left), under isoflurane (middle), or under ketamine (right). Current sinks are depicted in blue and current sources are shown in red. The purple dashed lines indicate the granular layer boundaries (L4). Note that the early VEP is preserved; however, later aspects of the visual evoked response are diminished in amplitude under each mechanistically distinct anesthetic.
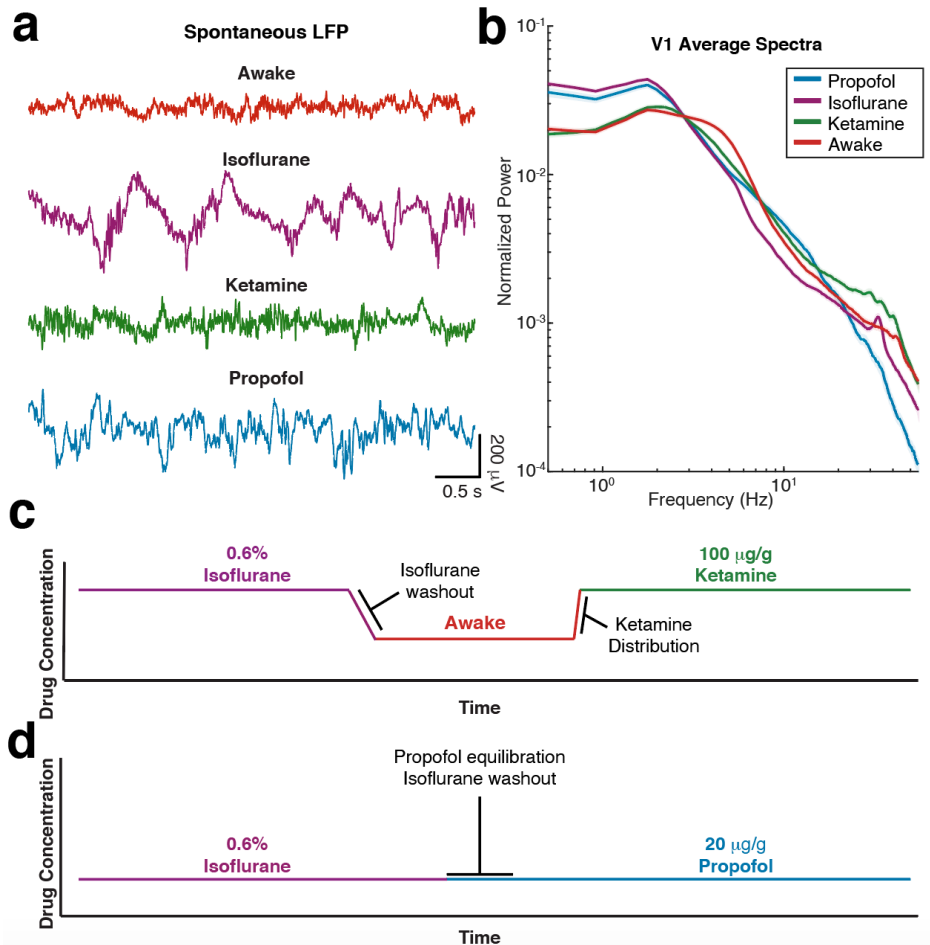
Figure 4.2: Baseline spectrum and experimental timeline

(A) LFP traces of 5 seconds of spontaneous activity recorded from an ECoG electrode on top of V1 in mice when awake (top, red) and under isoflurane (top middle, purple), ketamine (bottom middle, green) and propofol (bottom, blue).

(B) Average power spectrum of spontaneous activity recorded from an ECoG on top of V1 for awake mice (red) and mice under isoflurane (purple), ketamine (green) and propofol (blue). Shading indicates the 95% confidence intervals of the average. LFP recorded from awake mice and mice under ketamine have higher power at higher frequencies whereas LFP recorded from mice under isoflurane and propofol have a predominance of low frequency oscillations.

(C) Experimental timeline of mice recorded from under isoflurane, awake, and under

ketamine. Mice were first given 0.6% isoflurane through a nose cone, then given 15 mins

for isoflurane washout before awake recordings began, then given 100 μg/g ketamine IP

(D) Experimental timeline of mice recorded from under isoflurane and propofol. Mice were

first given 0.6% isoflurane through a nose cone, then started on a 20 μg/g brain target

concentration of propofol IV. Animals were given 15 mins for isoflurane washout before

propofol recordings began.
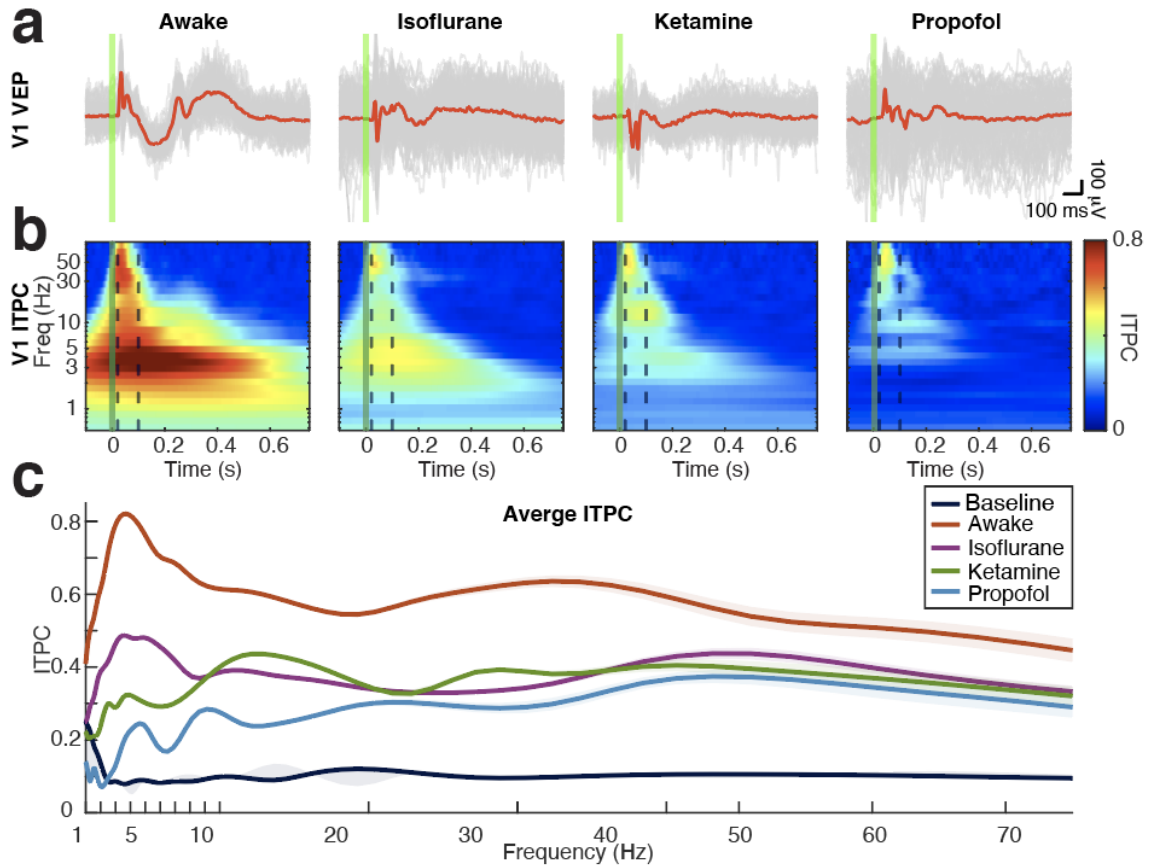
Figure 4.3: Visual evoked potentials in V1 contain high frequency ITPC, but not low frequency ITPC under isoflurane, ketamine, and propofol anesthesia

(A) Single trial (gray) and average (red) visual evoked potentials (VEPs) from a representative mouse when awake (left), under isoflurane (middle left), ketamine (middle right) and propofol (right). The vertical green line denotes stimulus onset.

(B) Intertrial phase coherence at the V1 electrode averaged over animals when awake (left), under isoflurane (middle left), ketamine (middle right), and propofol (right). The vertical green line denotes stimulus onset. The vertical dashed lines indicate the time frame for calculating average early ITPC under each condition. Note that evoked trial coherent activity below 5Hz diminishes under anesthesia.

(C) Average ITPC over the first 100ms of the VEP at V1 in mice that are awake (orange), under isoflurane (purple), ketamine anesthesia (green), and propofol (blue). The baseline

ITPC (calculated for 900-800ms before the stimulus onset) in awake mice is shown in

black. 95% confidence intervals of the mean are indicated by the shading.
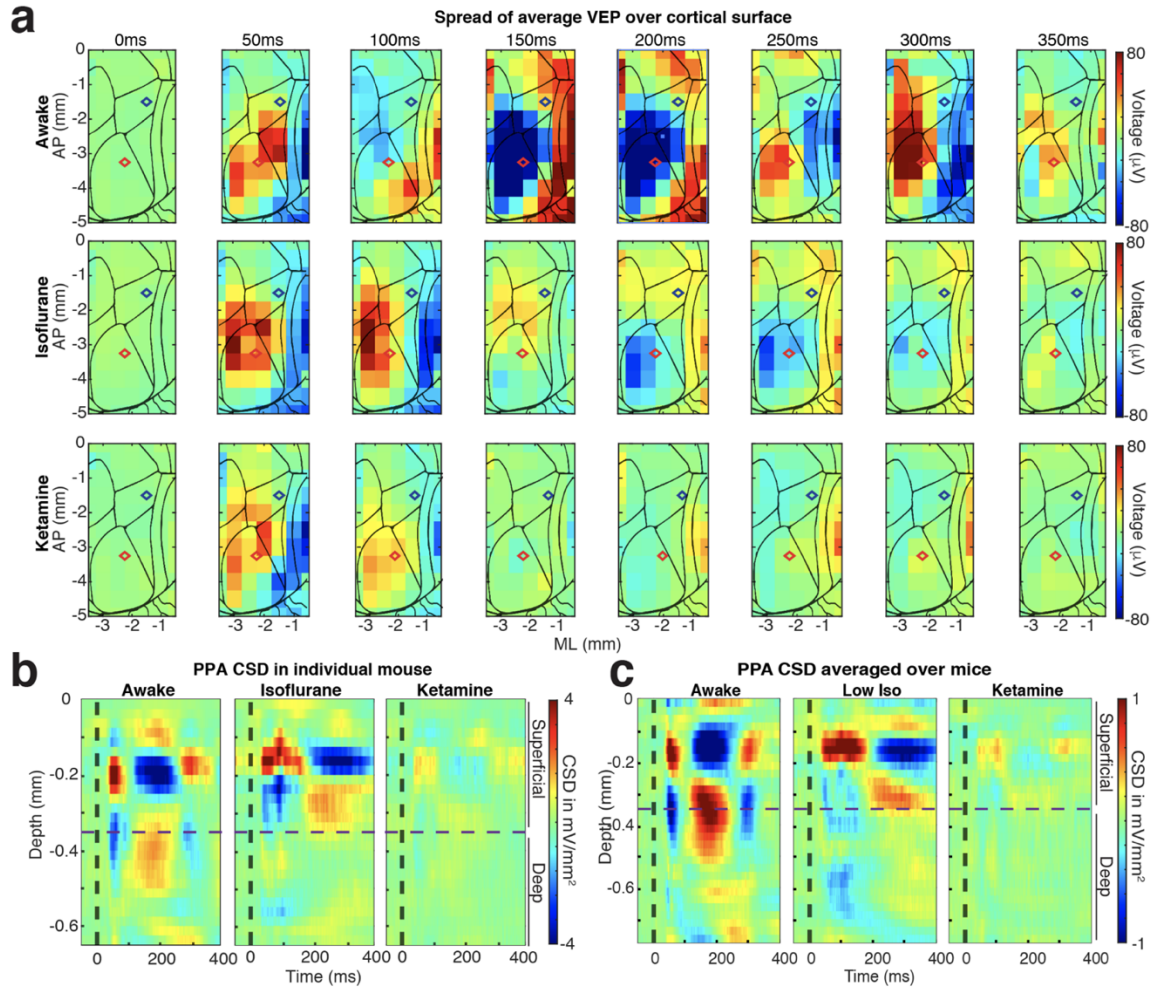
Figure 4.4: Visual evoked responses are seen outside of V1 in mice that are awake and under isoflurane and ketamine

(A) Time series of how the average visual evoked response progresses over space and time in mice that are awake (top), or under isoflurane (middle), or ketamine (bottom). Data at each stereotaxic location has been averaged over trials and animals. While the average response to visual stimuli is larger in amplitude in the awake brain, visual evoked activity is observed outside of V1 in mice under anesthesia.

(B) Current source density (CSD) of LFP from a laminar electrode array placed in PPA in a representative animal when he was awake (left), under isoflurane (middle) and under ketamine (right). The purple dashed lines indicate the boundary between superficial and

deep layers (between L4 and L5). Oscillatory visual evoked activity is observed

predominantly in the superficial layers when the mouse is awake, but the activity within

the PPA is diminished when the same mouse is given anesthesia.

(C) Current source density (CSD) of LFP averaged over mice from laminar electrode arrays

placed in PPA in animals displayed in the same manner as B. Similar to the activity

profile of the individual mouse, visual stimuli tend to elicit activity within the superficial

layers of the PPA when mice are awake, but activity is diminished when mice are under
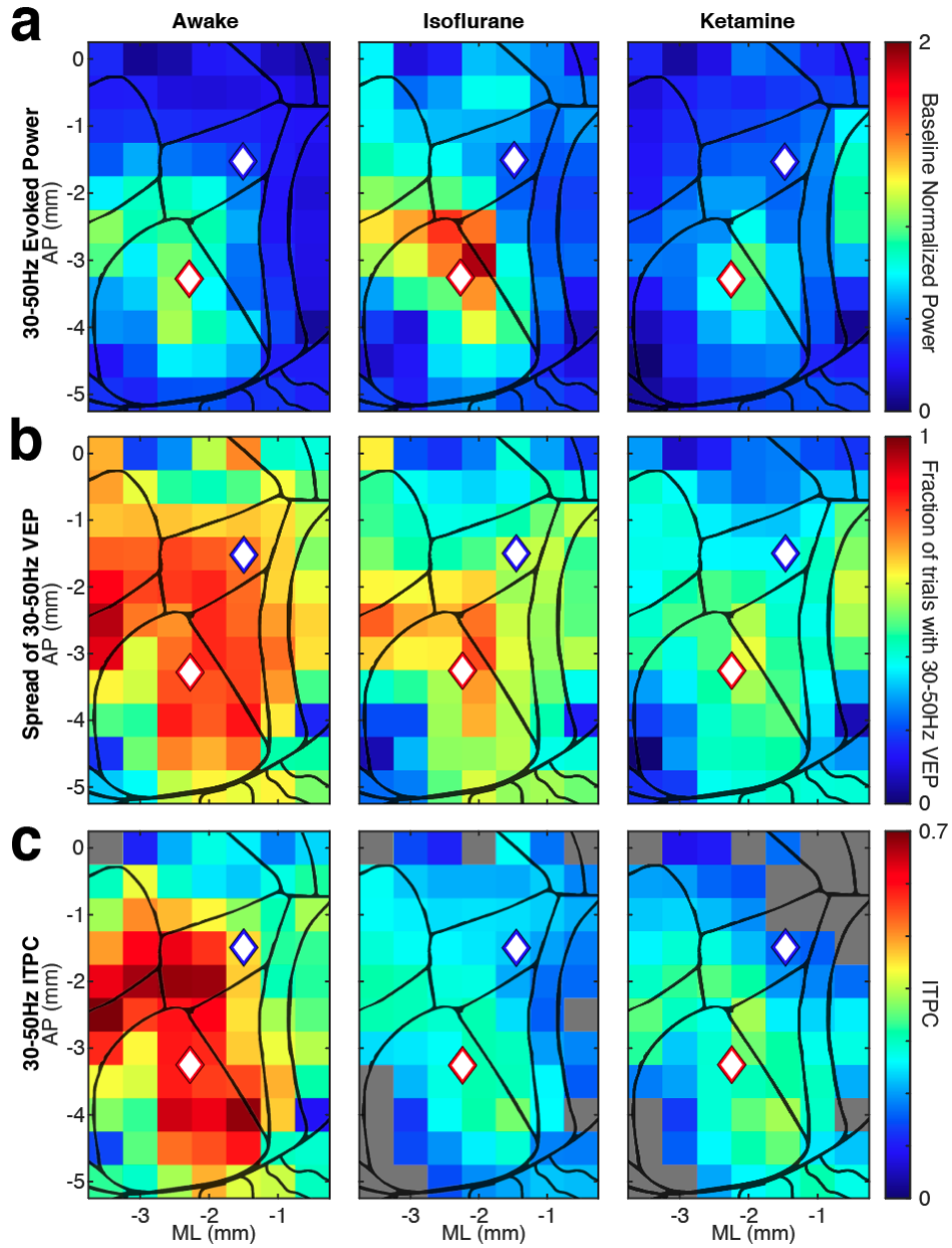
anesthesia.

Figure 4.5: Evoked fast frequency amplitude over the cortical surfaces is preserved, but intertrial coherence is diminished under anesthesia

(A) Evoked 30-50Hz signal amplitude during the first 350ms after stimulus onset is normalized to 500ms of baseline 30-50Hz activity, averaged across animals, and plotted over the cortical surface during wakefulness (left), under isoflurane (middle), or under ketamine (right).

(B) Fraction of trials at each location that exceed 5 standard deviations of baseline 30-50Hz amplitude during the first 350ms after stimulus onset were averaged across animals and plotted over the cortical surface during wakefulness (left), under isoflurane (middle), or under ketamine (right).

(C) Intertrial phase coherence (ITPC) at 30-50Hz over the first 100ms of post-stimulus activity at each cortical surface location averaged over animals during wakefulness (left), under isoflurane (middle), or under ketamine (right). Note that cortical areas both within and outside of V1 have higher ITPC in animals that are awake compared to the same animals under anesthesia. Locations in gray signify locations in which ITPC did not increase compared to time shuffled surrogates (Stouffer's test).
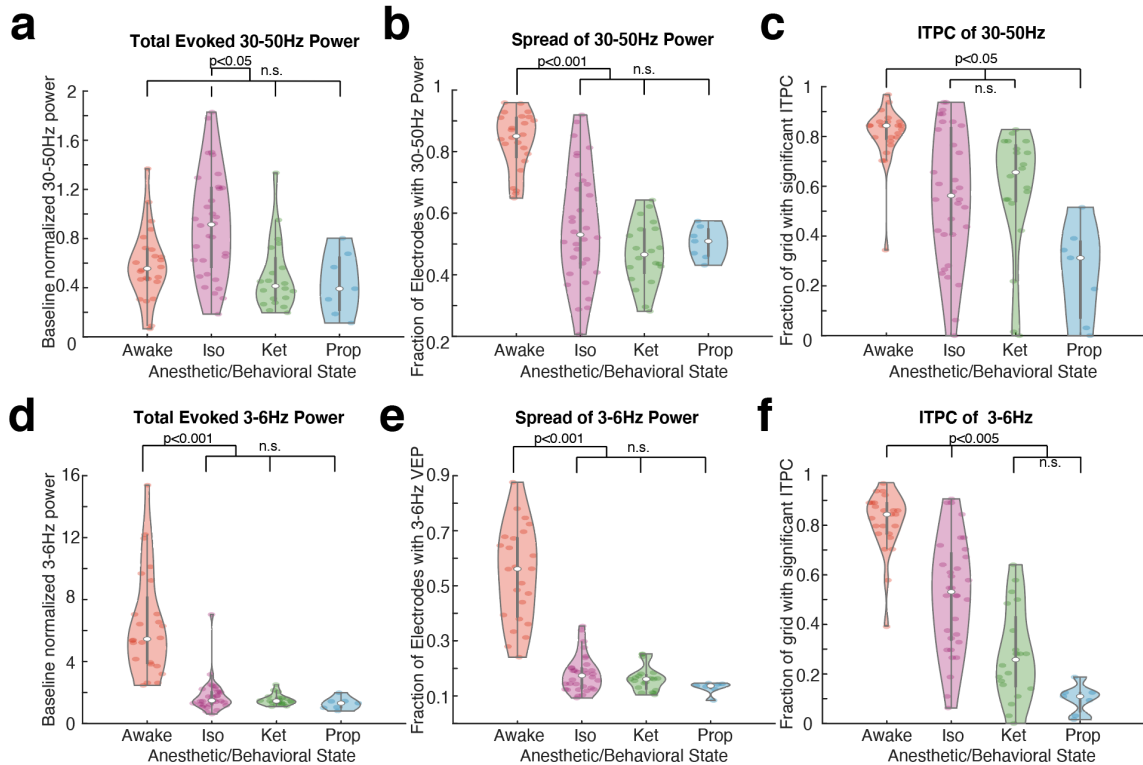
Figure 4.6: Quantification of 30-50Hz and 3-Hz evoked power, spread, and ITPC

(A) Visual evoked 30-50Hz power within the first 350ms after stimulus onset, normalized to baseline power, and averaged over electrodes and trials. Visual stimuli evoked higher baseline normalized power when mice are under isoflurane compared to when mice are awake or under ketamine or propofol (p-value < 0.001; Kruskal Wallis; p-value = 0.042, Wilcoxon rank sum)

(B) Fraction of trials in which visual stimuli evoked a 30-50Hz VEP at each electrode (quantified by a greater than 5 standard deviation increase in 30-50Hz power within the first 350ms after stimulus onset, compared to baseline power), at each location, averaged over electrodes within each mouse. Visual stimuli evoke 30-50Hz activity consistently across electrodes and trials when mice are awake compared to when mice are under anesthesia (p-value <0.00001; Kruskal Wallis; p-value = 0.0006, Wilcoxon rank sum)

(C) Average 30-50Hz ITPC within the first 100ms after stimulus onset, averaged over electrodes for each animal. Visual stimuli evoke higher 30-50Hz phase coherence across trials and electrodes when mice are awake compared to when mice are under anesthesia p-value <0.00001; Kruskal Wallis; p-value = 0.024, Wilcoxon rank sum)

(D) Visual evoked 3-6Hz power within the first 1000ms after stimulus onset, normalized to baseline 3-6Hz power, and averaged over electrodes and trials. Visual stimuli evoked higher baseline normalized power when mice are awake compared to when mice are under anesthesia (p-value= , Kruskal Wallis; Wilcoxon p-values = 0.0006, Wilcoxon rank sum)

(E) Fraction of trials in which visual stimuli evoked a 3-6Hz VEP at each electrode (quantified by a greater than 5 standard deviation increase in 3-6Hz power within the first 1000ms after stimulus onset, compared to baseline power), at each location, averaged over electrodes within each mouse. Visual stimuli evoke 3-6Hz activity consistently across electrodes and trials when mice are awake compared to when mice are under anesthesia (p-value< 0.00001, Kruskal Wallis; p-values = 0.0006, Wilcoxon rank sum)

(F) Average 3-6Hz ITPC over the first 500ms after the stimulus onset, averaged over electrodes for each animal. Visual stimuli evoke higher 3-6Hz phase coherence across trials and electrodes when mice are awake compared to when mice are under anesthesia (p-value= 0.00001, Kruskal Wallis; p-value = 0.0024, Wilcoxon rank sum)
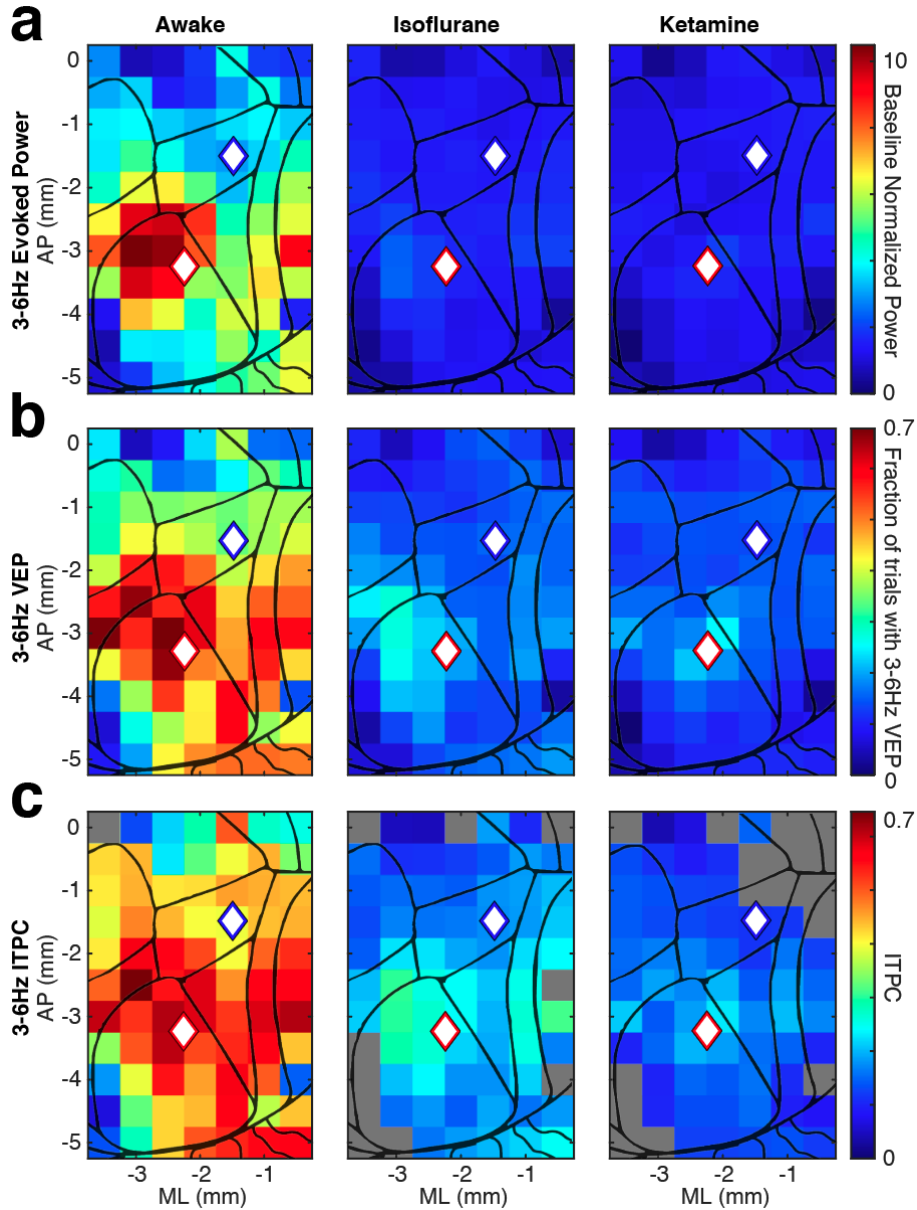
Figure 4.7: Evoked slow frequency amplitude and intertrial phase coherence are decreased under anesthesia

(A) Evoked 3-6Hz amplitude during the first 1000ms after stimulus onset is normalized to 500ms of baseline activity, averaged across animals, and plotted over the cortical surface during wakefulness (left), under isoflurane (middle), or under ketamine (right). Note that

there is more evoked 3-6Hz amplitude over the cortical surface in the waking state
compared to under anesthesia.

(B) Fraction of trials at each location that exceed 5 standard deviations of baseline 3-6Hz
amplitude during the first 1000ms after stimulus onset were averaged across animals and
plotted over the cortical surface during wakefulness (left), under isoflurane (middle), or
under ketamine (right).

(C) Intertrial phase coherence (ITPC) at 3-6Hz over the first 500ms of post-stimulus activity
at each cortical surface location averaged over animals during wakefulness (left), or
under isoflurane (middle), or ketamine (right). Note that cortical areas both within and
outside of V1 have higher ITPC in animals that are awake compared to when the same
animals are under anesthesia. Locations in gray signify locations in which ITPC did not
increase compared to time shuffled surrogates (Stouffer's test).
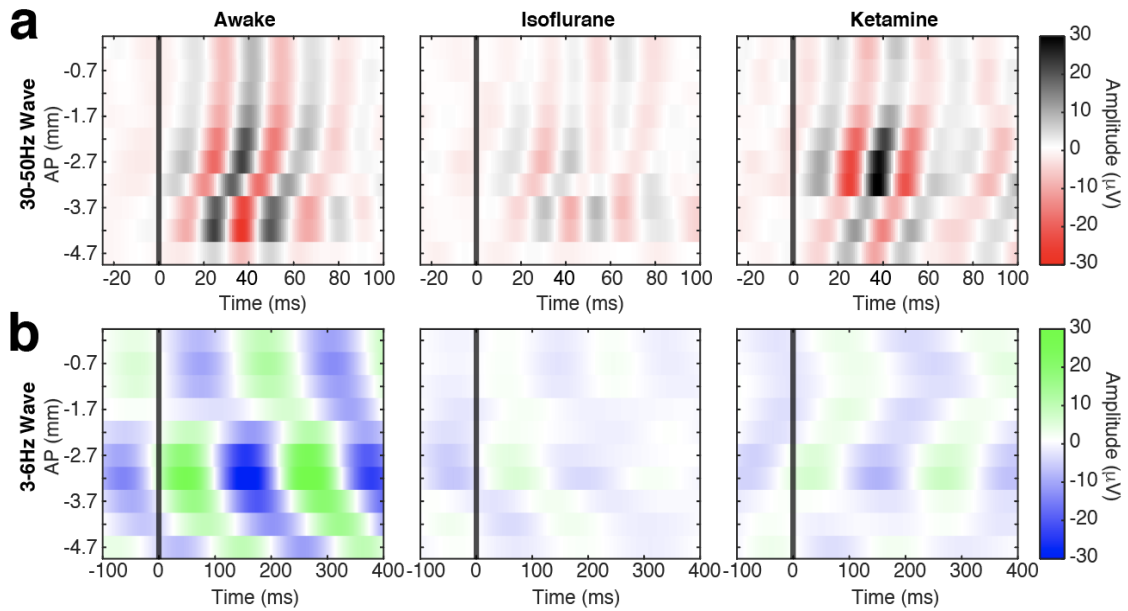
Figure 4.8: Visual evoked fast feedforward surface waves are disrupted under anesthesia while feedback slow waves are abolished

(A) VEPs filtered at 30-50Hz, averaged over trials, from 10 electrodes along the anterior to posterior (AP) axis (-1.80 mm ML) in a representative mouse. The x-axis denotes time from stimulus onset. The y-axis denotes AP distance from bregma. Note that the high frequency signal begins in posterior V1 and propagates anteriorly when the animal was awake, but the average amplitude propagation patterns are attenuated and disrupted when the same animal is under isoflurane or ketamine.

(B) VEPs filtered at 3-6Hz, averaged over trials, from the same representative mouse as in A. Note the low frequency waves begin more anteriorly to the fast wave initiation zone and travel posteriorly when the animal is awake. However, the slow wave average amplitude is greatly diminished when the animal is under isoflurane or ketamine.
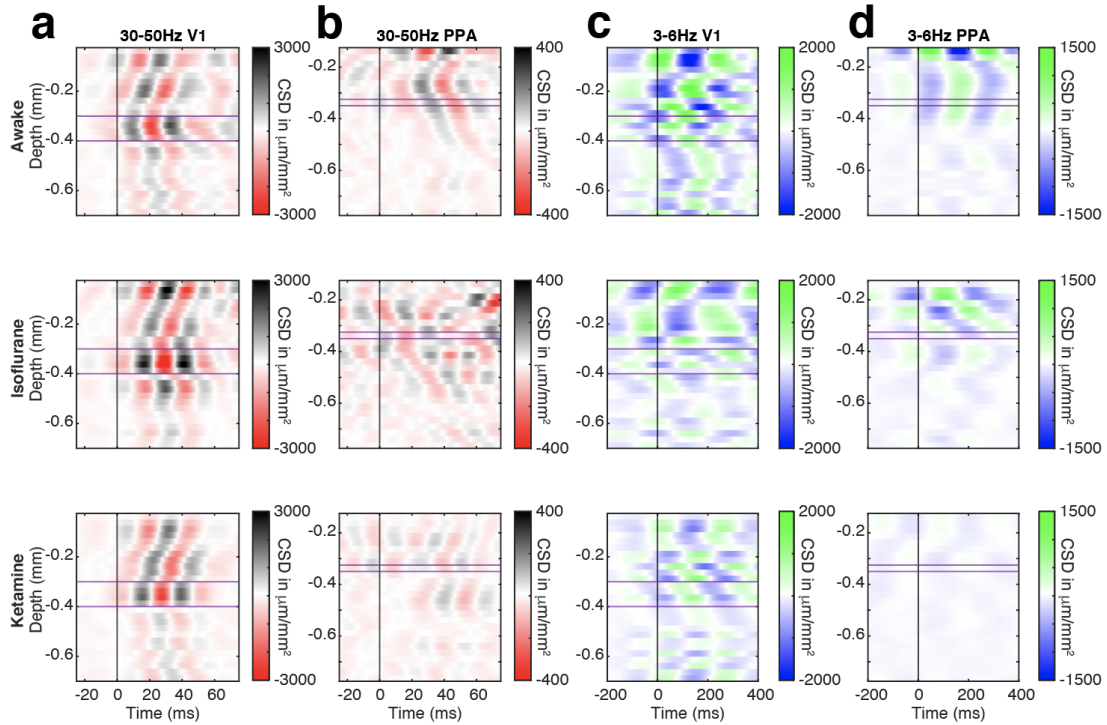
Figure 4.9: Laminar organization of fast wave is maintained in V1 under anesthesia, but the laminar profile of both fast and slow oscillations is disrupted in PPA under anesthesia

(A) Depth profile of average LFP within the V1 parenchyma, filtered at 30-50Hz, in a single mouse during distinct states: wakefulness (top), under isoflurane (middle), and under ketamine (bottom). The x-axis is time, with the black line at 0ms indicating stimulus onset. The y-axis indicates depth from the pia. The purple lines are layer 4 boundaries. Note that under all three anesthetics, fast frequency oscillations begin in layer 4 and propagate superficially and deep.

(B) Depth profile of average LFP within the PPA parenchyma, filtered at 30-50Hz, in the same mouse and organized in the same manner as A. Note that in phase coherent fast frequency oscillations are prominent when mice are awake in the superficial layers, but 30-50Hz oscillations are more disorganized under anesthesia.

(C) Depth profile of average LFP within the V1 parenchyma, filtered at 3-6Hz, in the same mouse and organized in the same manner as A.

(D) Depth profile of average LFP within the PPA parenchyma, filtered at 3-6Hz, in the same mouse and organized in the same manner as A. Note that in phase coherent slow frequency oscillations are prominent when mice are awake in the superficial layers, but 30-50Hz oscillations are distorted under anesthesia.
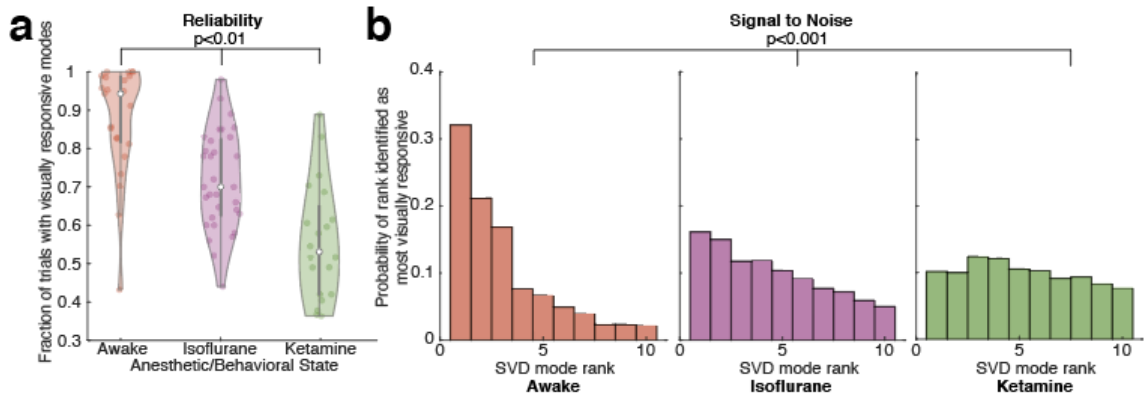
Figure 4.10: Feedforward fast waves are more reliable and contain higher signal variance in when animals are awake compared to when animals are under anesthesia

(A) Probability of the SVD mode rank of the most visually responsive mode identified on each trial aggregated across animals. The most visually responsive mode was more likely to be the first mode when animals were awake or under isoflurane, but not when the same animals were under ketamine (p<0.00001, Kruskal Wallis, pairwise p= 0.0057, Rank Sum).

(B) Fraction of trials in which at least one visually responsive mode was found (methods) in each mouse under each behavioral state. In the waking state, visually responsive modes were found more often than under isoflurane, and both had more visually responsive modes uncovered than other ketamine (p<0.0001, Kruskal Wallis, pairwise p<0.001, Rank Sum).
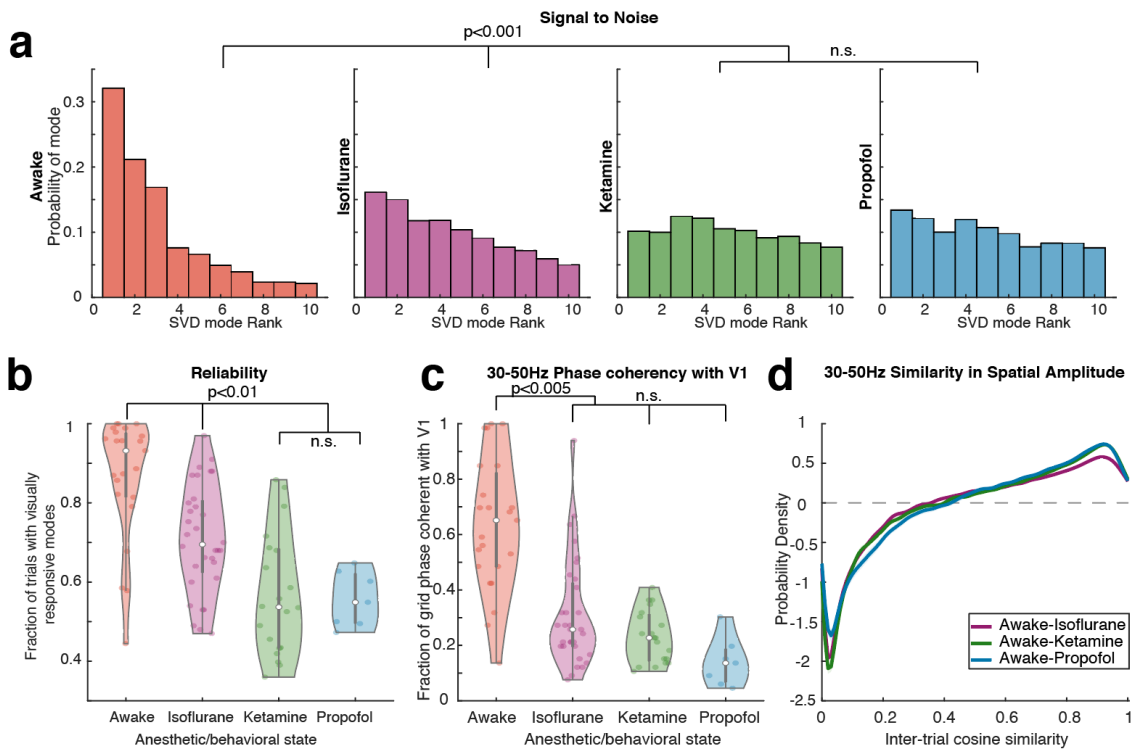
Figure 4.11: Visual stimuli elicit fast traveling waves that are higher signal to noise, reliability evoked, and consistent in activation pattern from trial to trial when animals are awake compared to when animals are under anesthesia

(A) Rank profile of most visually responsive 30-50Hz mode on each trial aggregated across animals when mice are awake (left), or under isoflurane (middle left), ketamine (middle right) or propofol (left). While the most visually responsive mode is often the first mode when mice are awake or under isoflurane, the most visually responsive mode is often not the first mode when mice are under ketamine or propofol (p<0.00001, Kruskal Wallis, pairwise p = 0.0002, Rank Sum).

(B) Fraction of trials in which at least one visually responsive mode was found (Methods) in each mouse, when awake or under isoflurane, ketamine or propofol. In the waking state, visually responsive modes were found more often than under isoflurane, and both had

140

more visually responsive modes uncovered than other ketamine or propofol (p<0.00001, Kruskal Wallis, pairwise p = 0.0082, Rank Sum).

(C) The fraction of electrodes that are significantly phase coherent with V1 (Raleigh test) within each animal, under each condition (p<0.00001, Kruskal Wallis, pairwise p= 0.0013, Rank Sum).

(D) The difference in the cosine similarity between the spatial amplitude of the most visually responsive SVD mode between awake and isoflurane (purple), awake and ketamine (green) and awake and propofol (blue). Shading displays the 95% confidence intervals of mean differences in cosine similarity between the waking and anesthetic states. The dashed black horizontal line denotes no change in the cosine distances of spatial modes. Note that when mice are awake, the spatial activation across electrodes is more similar from trial to trial than when animals are under anesthesia.
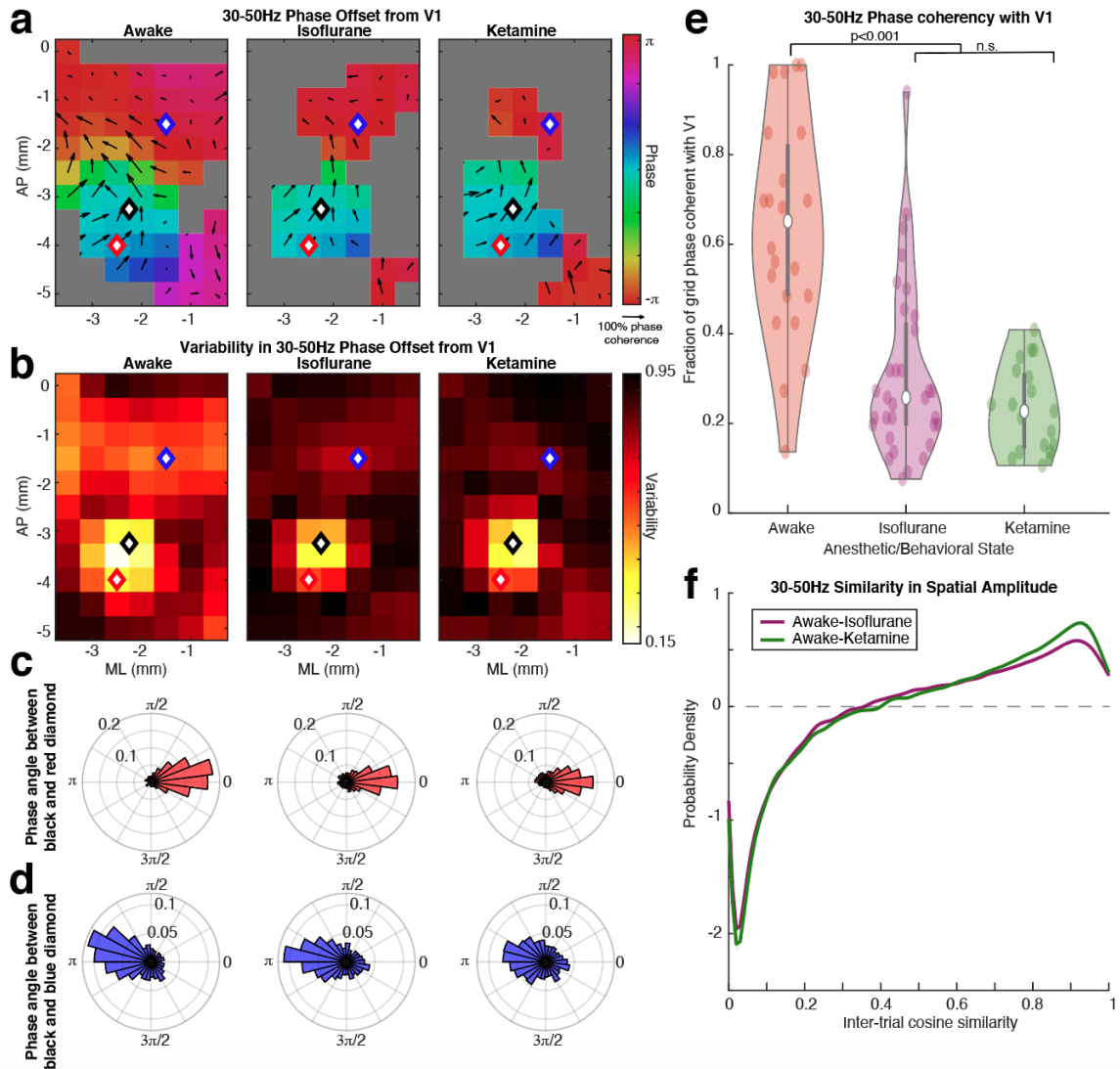
Figure 4.12: Fast frequency oscillations form a coherent wave over large areas of the cortical surface in awake mice, but when mice are under anesthesia, the trial-to-trial variability in the visual evoked fast waves increases outside of V1

(A) At each stereotaxic location, the average phase offset of the most visually responsive 30-50Hz spatial mode relative to V1 (the black diamond) is plotted in color. The arrows depict the spatial gradient. The directions of the arrows show the direction of spatial phase progression and the magnitude of the arrows correspond to the consistency of the angle of the spatial phase gradient over trials and animals. Gray locations did not meet

142

Bonferroni corrected statistical significance (Raleigh test) across trials and animals. Note that the direction of propagation of visually evoked fast waves are similar in V1 when animals are anesthetized and awake.

(B) The variance of the spatial phase offset relative to V1 (black diamond) is plotted across trials and animals at each stereotaxic location. Lighter colors correspond to a more consistent phase angle offsets, whereas darker colors correspond to more variance in phase angles across trials and animals. Under anesthesia, the variance in the phase relationship of channels outside of V1 increases compared to when animals are awake.

(C) Histogram of the phase angle difference of the most visually responsive 30-50 Hz modes at two different locations within V1 (black and blue diamonds in A and B) across trials and animals in mice that are awake (left), or under isoflurane (middle) or ketamine (right).

(D) Histogram of phase angle difference between V1 and PPA (black and red diamonds, respectively, in A and B) across trials and animals in mice that are awake (left), or under isoflurane (middle) or ketamine (right). Note that the distribution of angle difference is wider when mice are under anesthesia as compared to awake mice

(E) The fraction of electrodes that are significantly phase coherent with V1 (Raleigh test, Bonferroni corrected) within each animal, under each condition (p<0.00001, Kruskal Wallis, pairwise p< 0.0001, Rank Sum).

(F) The difference in the cosine similarity between the spatial amplitude of the most visually responsive SVD mode between awake and isoflurane (purple) and awake and ketamine (green). The dashed black horizontal line denotes no change in the cosine distances of spatial modes. Note that when mice are awake, the spatial activation across electrodes is more similar from trial to trial than when animals are under anesthesia.

Figure 4.13: Visual stimuli elicit slow traveling waves that are higher signal to noise, reliability evoked, and consistent in activation pattern from trial to trial when animals are awake compared to when animals are under anesthesia

(A) Rank profile of most visually responsive 3-6Hz mode on each trial aggregated across animals when mice are awake (left), or under isoflurane (middle left), ketamine (middle right) or propofol (left). (p<0.00001, Kruskal Wallis, pairwise p=0.0196, Rank Sum).

(B) Fraction of trials in which at least one visually responsive mode was found (Methods) in each mouse, when awake or under isoflurane, ketamine or propofol (p<0.0001, Kruskal Wallis, pairwise p<0.001, Rank Sum).

(C) The fraction of electrodes that are significantly phase coherent with V1 (Raleigh test) within each animal, under each condition (p<0.0001, Kruskal Wallis, pairwise p=0.0007, Rank Sum).

(D) The difference in the cosine similarity between the spatial amplitude of the most visually responsive SVD mode between awake and isoflurane (purple), awake and ketamine

144

(green) and awake and propofol (blue). Shading displays the 95% confidence intervals of mean differences in cosine similarity between the waking and anesthetic states. The dashed black horizontal line denotes no change in the cosine distances of spatial modes. Note that when mice are awake, the spatial activation across electrodes is more similar from trial to trial than when animals are under anesthesia.
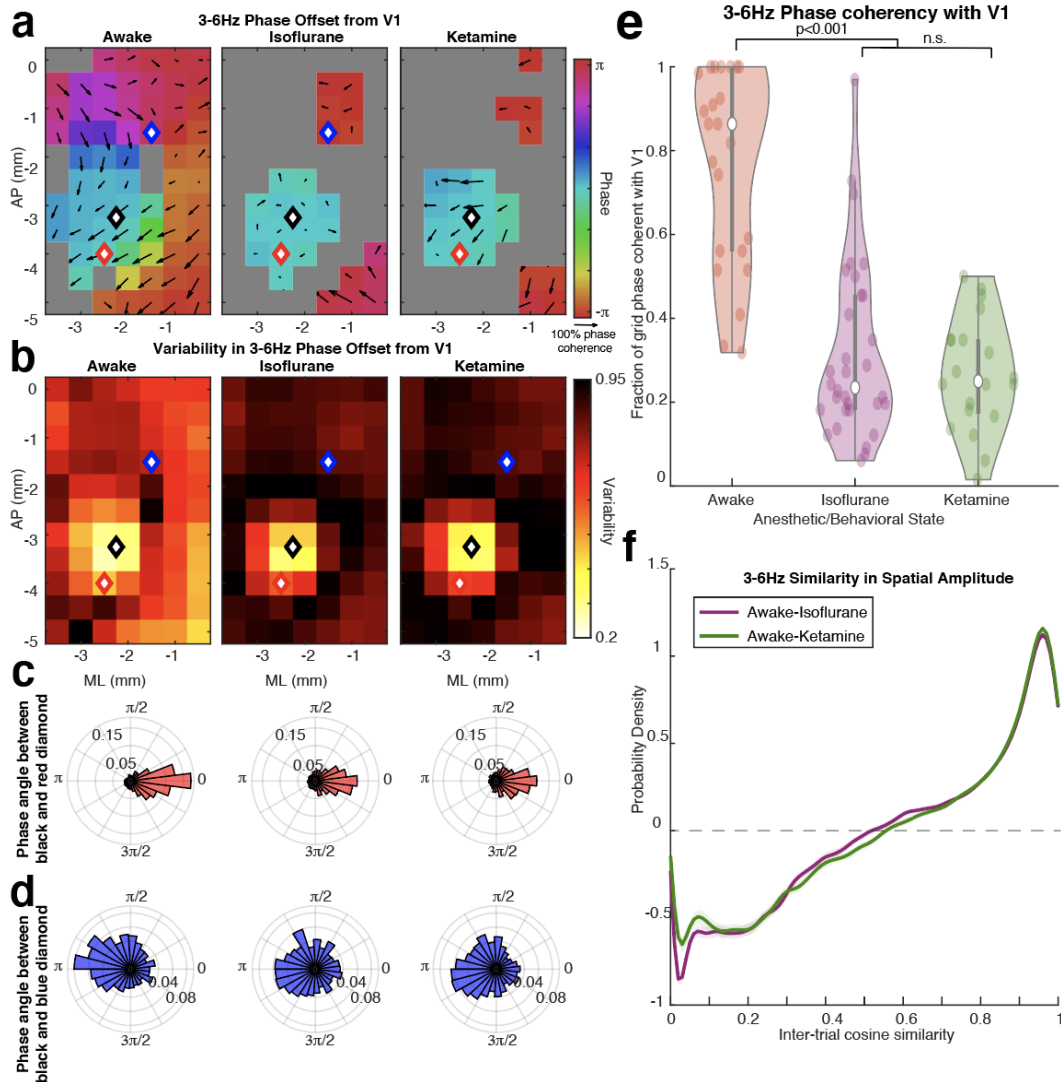
Figure 4.14: Slow frequency oscillations form a coherent wave over large areas of the cortical surface in awake mice, but when mice are under anesthesia, the slow wave is only present within V1

(A) At each stereotaxic location, the average phase offset of the most visually responsive 3-6Hz spatial mode relative to V1 (the black diamond) is plotted in color. The arrows depict the spatial gradient. The directions of the arrows show the direction of spatial phase progression and the magnitude of the arrows correspond to the consistency of the angle of the spatial phase gradient over trials and animals. Gray locations did not meet

Bonferroni corrected statistical significance (Raleigh test) across trials and animals. Note that the direction of propagation of visually evoked fast waves are similar in V1 when animals are anesthetized and awake.

(B) The variance of the spatial phase offset relative to V1 (black diamond) is plotted across trials and animals at each stereotaxic location. Lighter colors correspond to a more consistent phase angle offsets, whereas darker colors correspond to more variance in phase angles across trials and animals. Under anesthesia, the variance in the phase relationship of channels outside of V1 increases compared to when animals are awake.

(C) Histogram of the phase angle difference of the most visually responsive 3-6Hz modes at two different locations within V1 (black and blue diamonds in A and B) across trials and animals in mice that are awake (left), or under isoflurane (middle) or ketamine (right).

(D) Histogram of phase 3-6Hz angle difference between V1 and PPA (black and red diamonds, respectively, in A and B) across trials and animals in mice that are awake (left), or under isoflurane (middle) or ketamine (right).

(E) The faction of electrodes that are significantly phase coherent with V1 (Raleigh test, Bonferroni corrected) within each animal, under each condition.

(F) The difference in the cosine similarity between the 3-6Hzspatial amplitude of the most visually responsive SVD mode between awake and isoflurane (purple) and awake and ketamine (green). The dashed black horizontal line denotes no change in the cosine distances of spatial modes. Note that when mice are awake, the spatial activation across electrodes is more similar from trial to trial than when animals are under anesthesia.
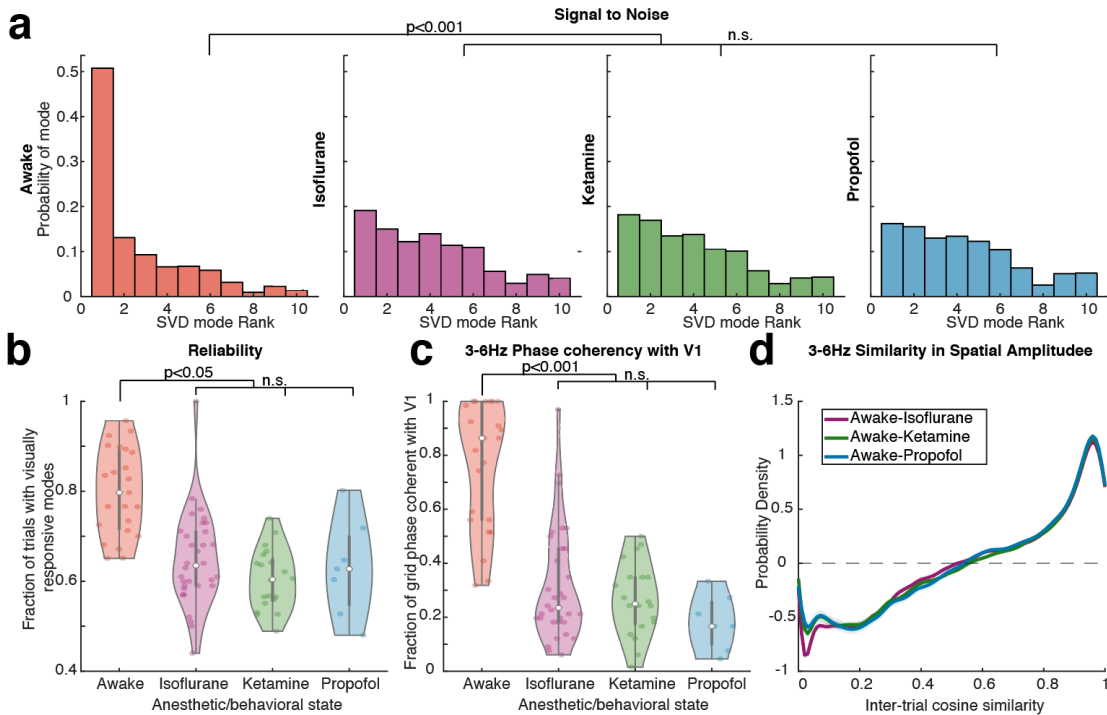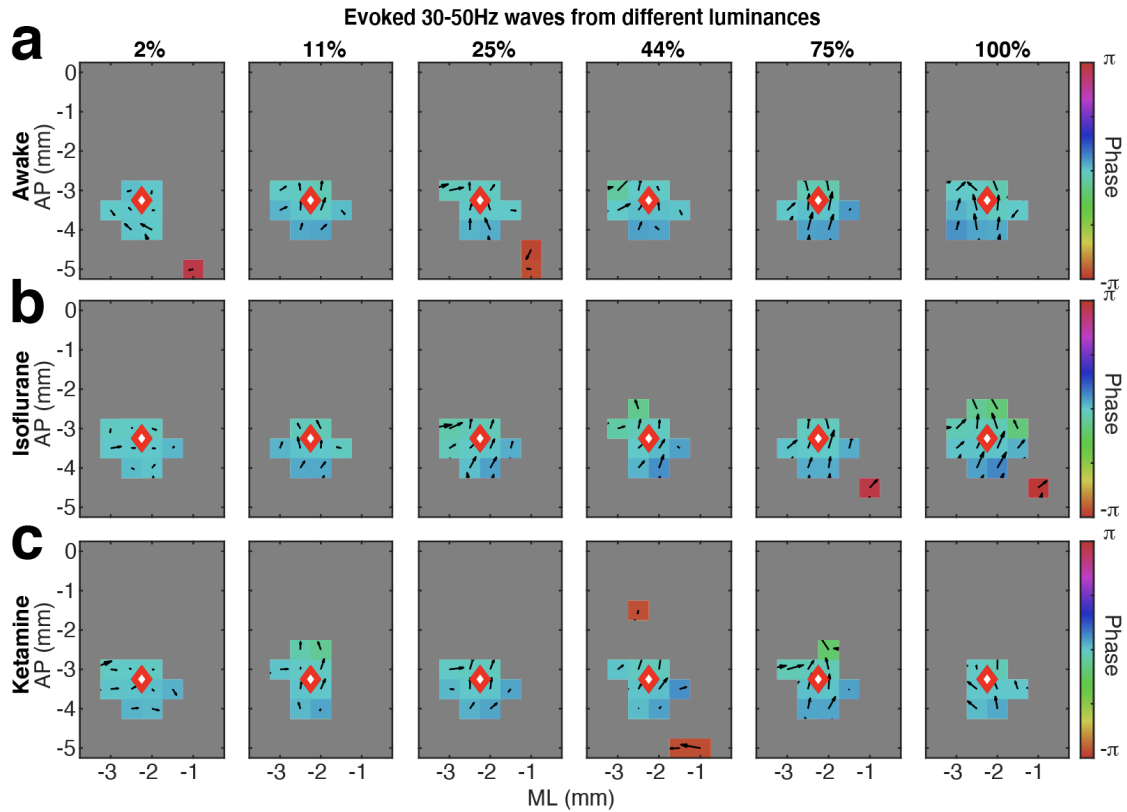
Figure 4.15: Visual stimuli elicit fast traveling waves that remain in V1 for low luminance stimuli in both awake and anesthetized animals

(A) Phase progression of the 30-50Hz wave as the screen luminance increases in awake mice.

(B) Phase progression of the 30-50Hz wave as the screen luminance increases in awake under isoflurane.

(C) Phase progression of the 30-50Hz wave as the screen luminance increases in mice under ketamine. Note that for lower luminance stimuli, the variance of phase angles between channels increase outside of V1 for animals that are awake or anesthetized.

* Within each diagram, gray locations did not meet Bonferroni corrected statistical significance (Raleigh test) across trials and animals.
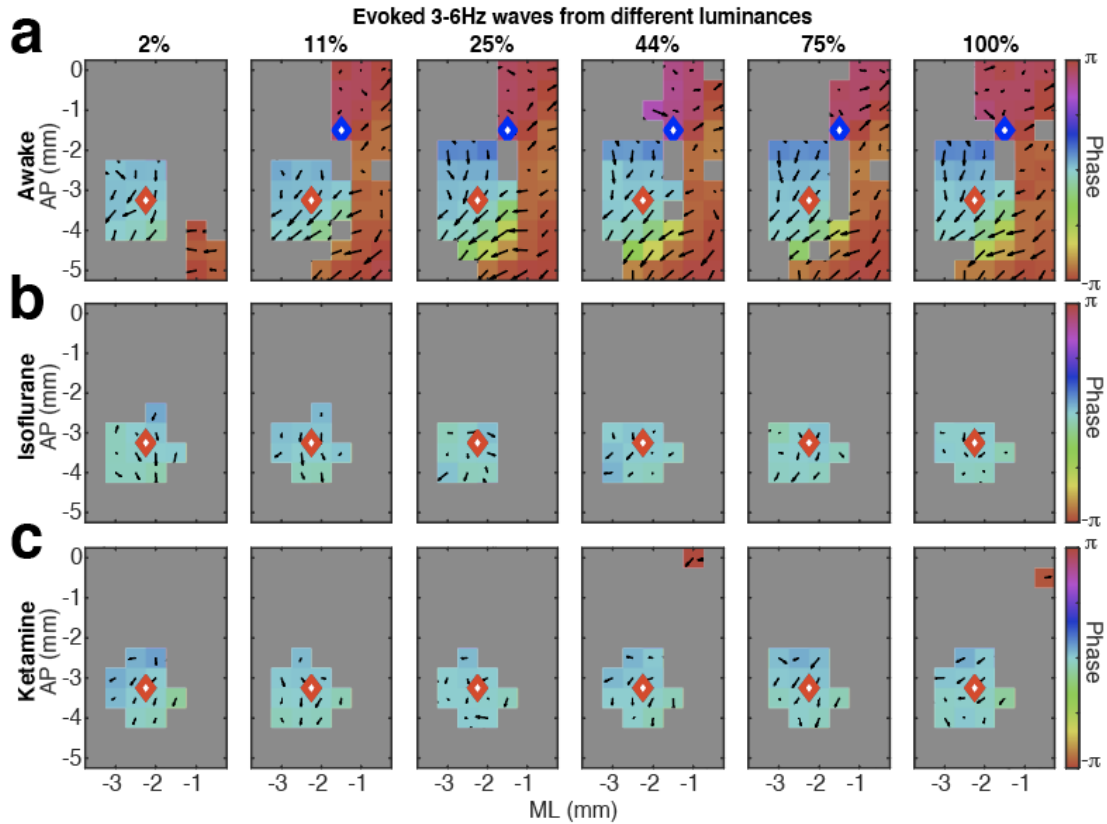
Figure 4.16: Slow frequency oscillations form a coherent wave over large areas of the cortical surface in awake mice, but when mice are under anesthesia, the slow wave is only present within V1

(A) Phase progression of the 3-6Hz wave as the screen luminance increases in awake mice. Note that when the screen luminance is at 2%, the slow wave is only detected around V1. However as stimulus intensity increase, the spatial extent of the slow wave also increases over the cortical surface

(B) Phase progression of the 3-6Hz wave as the screen luminance increases in awake under isoflurane. Note regardless of screen intensity, slow waves are only detected around V1.

(C) Phase progression of the 3-6Hz wave as the screen luminance increases in mice under ketamine. Similar to mice under isoflurane, slow waves are only detected around V1 regardless of screen intensity.

* Within each diagram, gray locations did not meet Bonferroni corrected statistical significance

(Raleigh test) across trials and animals.

CHAPTER 6- General Discussion

In summary, my thesis work demonstrates that in awake mice, simple visual stimuli on a single trial basis reliably evoke two traveling waves at two different temporal frequencies. The fast, 30-50Hz, evoked waves begin in V1 and propagate anterolaterally in a feedforward direction, and the slow, 3-6Hz, evoked waves begin more rostrally waves spread posteromedially in a feedback manner. The phase of the slow wave modulates the amplitude of the fast wave. Moreover, the spatial wavelength of both waves is on the order of the cerebral hemisphere. This suggests that these waves may be a neurophysiological process that coordinates neuronal activity evoked by visual stimuli across distant brain areas. In direct support of this notion, the phase of the slow wave also entrains the firing patterns of previously uncorrelated V1 and PPA neurons after stimulus onset, thereby generating a transient neural assembly across the visual hierarchy (Chapter 2).

We then turned to studying the effects of mechanistically distinct anesthetics on feedforward and feedback waves of electrical activity elicited by simple visual stimuli. While some effects of anesthetics depend strongly on the specific anesthetic agent, others proved to be universally observed regardless of drug identity. Agent specific effects mostly involve the fast feedforward oscillations. For instance, we show that in mice given equipotent doses of isoflurane and propofol, the intertrial phase coherence (ITPC) of visual evoked gamma oscillations in V1 is substantially lower under propofol as compared to isoflurane (Chapter 3). This is remarkable because spontaneous EEG characteristics is similar under both of these drugs. At lower concentrations, both propofol and isoflurane elicit slow oscillations in the delta range (1-4 Hz), reminiscent of those observed during natural sleep. With higher concentrations of either drug, burst suppression is reliably observed. In both research and clinical settings, the state of anesthesia is most commonly assessed using the power spectrum of the EEG. Indeed, much of the work addressing

mechanisms responsible for the generation of spontaneous slow oscillations as well as the functional consequences that slow oscillations have on sensory processing, largely ignores the specifics of anesthetic agents. Yet, our results suggest that given essentially identical spontaneous EEG characteristics, responses to sensory stimuli depend strongly on the identity of the anesthetic agent.

Finally, the strongest evidence for the potential contribution of feedback waves in orchestrating coordinated neural activity across distant cortical sites is that three mechanistically distinct general anesthetics commonly abolish the generation, signal to noise and spatial activation pattern of the visual evoked slow feedback wave. Remarkably, even with strong stimuli, under the influence of hypnotic levels of anesthesia, visual evoked feedback waves are comparable to those of the weakest stimulus presented to awake animals. Therefore, these results are consistent with the notion that visual evoked slow feedback waves may be necessary to coordinate activity among disparate cortical regions in order to transform visual stimuli into perception. Moreover, the universal suppression of feedback visual evoked waves by mechanistically distinct anesthetics makes it a promising candidate for a shared mechanism that leads to anesthetics induced loss of consciousness (Chapter 4).

Limitations and Future directions

Chronic preparation

Acute on chronic preparations are technically easier to perform and more financially feasible, especially while developing a new experimental paradigm, but they have some important drawbacks. For example, while we provide ample evidence that our mice are awake (including collecting low amplitude fast frequency EEG, observing spontaneous movement, and passive and active whisking), and we do allow for isoflurane washout, we cannot be certain that no residual anesthetic effect is present in our awake recordings. Additionally, even though we preformed the

craniotomy with local anesthetic scalp blocks and provided mice with both steroids and non-steroidal anti-inflammatory drugs (NSAIDs) to minimize the inflammation and pain, we cannot ensure that the effects that we are observing are not confounded by the acute effects of surgery, including potential dissipation of analgesia. In the future, it would be fruitful to repeat these experiments in a subset of mice that are chronically implanted with high density ECoG grids and allow animals to recover before recording visual evoked traveling waves during the waking and/or anesthetized states.

Behavioral task to probe visual perception

While we demonstrate that visual stimuli evoke two traveling waves with spatiotemporal properties that are consistent with large scale feedforward-feedback processes, we cannot definitively assess the behavioral roles of these waves. To dissect the function of visual evoked traveling waves in perception, future research must focus on generating a task in which animals report when they witness visual stimuli. In animals that are awake, one would ideally create a go/no-go task in which water restricted animals learn to lick when they see visual stimuli for a water reward.

However, task design becomes more complicated when attempting to probe perception in anesthetized animals. Here, I aimed to deliver hypnotic doses of anesthesia in order to ablate consciousness without inducing deep anesthetic states. At these doses, however, animals are projected to be responsive on a subset of trials (McKinstry-Wu et al., 2019). Since many anesthetic agents have sedative properties (Alkire and Miller, 2005; Lu et al., 2008a), mice may be less motivated to complete the task under anesthesia, even though they might well perceive visual stimuli. Thus, one would need to construct a paradigm in which researchers can measure both perception and motivation. Therefore, a two-alternative forced choice task might be a suitable option (Burgess et al., 2017). In this design, water restricted mice would report by licking

one of two lick-ports if they saw or did not see visual stimuli when a test cue is presented. Trials

in which mice do initiate licks, might therefore be interrupted as trials in which mice are not

motivated to complete the task. However, this task design would require mice to remember if they

saw visual stimuli at least until they received the cue stimulus. Since many anesthetic drugs are

also produce amnesia (Hao et al., 2020; Hemmings et al., 2019), interpretation of the results of

this task may also prove difficult.

Information content in feedforward and feedback waves

In this dissertation, I describe the visual evoked waves as feedforward and feedback

given their sites of initiation and propagation directions. However, I do not directly test whether

feedforward waves encode information about stimulus characteristics. In order to examination

this, one must provide animals with a series of parametrically changing visual stimuli and record

how the spatiotemporal properties of the feedforward wave change with stimulus parameters. I

also do not directly test if the feedback waves contain context cues or predictions. To investigate

this, one could present mice with a series of visual stimuli that changes unpredictably, such as an

oddball (Nourski et al., 2017), and record how response properties of the slow and fast waves

change with standard and oddball stimuli.

The integration of multiple stimuli

Our results indicate that a simple brief flash of light elicits a multiplexed travelling wave

that spreads over large areas of the cortical surface and long outlasts stimulus presentation.

Thus, the waves characterized in this work, may be thought of as an impulse response of a

system. How waves evoked by static natural scenes manifest within the brain remains unknown.

Natural images contain a multitude of stimulus attributes arranged in a complex spatial profile. It

is possible, for instance, disparate components of the input stimulus evoke oscillations that destructively interfere, and therefore, the waves elicited might be lower in amplitude or have a more complex spatiotemporal pattern.

While static natural scenes are an example of how multiple stimulus features can be presented at once, another fascinating question is how do evoked waves from stimuli presented in temporal succession interact? For example, Gao et al. illustrates that when the interstimulus interval is short, cortical waves evoked by the first visual stimulus suppress visual evoked waves from the second stimulus. Yet, with longer interstimulus intervals, the wave evoked from the first stimulus fuses with the wave evoked from the second, thereby generating a combined wave that propagates faster and farther than the waves elicited from either stimuli presented in isolation (Gao et al., 2012). However, these waves were identified by recording trial average VSD imaging over the visual cortex in rats, and does not examine whether similar phenomena are seen on a larger scale (Gao et al., 2012).

Further, it would be interesting to investigate if stimuli from other sensory modalities evoke a similar set of traveling waves. If so, how do cortical waves elicited from multimodal stimuli interact? Might the interference pattern generated by multimodal waves provide the neurophysiological substrate for multisensory integration? Much of the multisensory literature suggests that evoked firing rates from weak multimodal stimuli add supra-linearly, whereas of responses to strong stimuli add sub-linearly (Stein and Stanford, 2008; Stevenson et al., 2014). We might expect a similar inverse relationship between the strength of multimodal stimuli and amount of destructive interference among the waves they elicit. Moreover, the interference pattern of waves elicited from multimodal stimuli might not display the same behavior uniformly over the cortical surface. Association areas, such as the PPA, are known to receive projections from many cortical areas processing many sensory modalities (Hovde et al., 2019; Ursino et al., 2014). Therefore, deviations from linearity in the interference pattern may be more prominent in association areas.

Finally given evidence that anesthetic agents suppress cross modal responses within primary cortical areas (Raz et al., 2014; Sellers et al., 2015), and decrease network integration (Boly et al., 2012; Monti et al., 2013; Tagliazucchi and Laufs, 2014), one might expect that low doses of anesthetic drugs may specifically alter the interference pattern of waves induced by multimodal stimuli, and thus disrupt multisensory integration.

Conclusion

In this dissertation, I demonstrate that visual stimuli evoke two traveling waves, one in the feedforward direction, and the other in the feedback direction in awake mice. The spatial extent and modulation pattern of these waves make them attractive candidates for organizing cortical activity along the visual hierarchy. Moreover, large scale feedback waves are not reliably elicited in awake animals receiving weak visual stimuli or animals anesthetized with any of the three agents tested. Therefore, visual evoked feedback waves have the potential to denote or actually be a neurophysiological signature of processing that transforms a visual stimulus into a unified percept. In the future, by probing mouse behavior with visual tasks, and altering the pattern of stimuli delivered, we can better quantify the perceptual power of these waves. Moreover, by examining how these waves interact during states of endogenous and pharmacologically induced states of decreased arousal, we might be able to better understand how consciousness is formed and lost.

REFERENCES

Achard, S., Delon-Martin, C., Vértes, P. E., Renard, F., Schenck, M., Schneider, F., Heinrich, C., Kremer, S., and Bullmore, E. T. (2012). Hubs of brain functional networks are radically reorganized in comatose patients. *Proc. Natl. Acad. Sci. U. S. A.* 109, 20608–13. doi:10.1073/pnas.1208933109.

Adrian, E. D. and Matthews, B. H. C. (1934). The Interpretation of Potential Waves in the Cortex. *J. Physiol.*, 440–471.

Adrian, E. D. and Yamagiwa, K. (1960). The Origin of the Berger Rhythem. *Brain* 58.

Aggarwal, A., Brennan, C., Luo, J., Chung, H., Contreras, D., Kelz, M. B., and Proekt, A. (2021). Visual evoked feedforward-feedback travelling waves organize neural activity across the cortical. *bioRxiv* 3, 6.

Aggarwal, A., Brennan, C., Shortal, B., Contreras, D., Kelz, M. B., Proekt, A., and Rainer, G. (2019). Coherence of Visual-Evoked Gamma Oscillations Is Disrupted by Propofol but Preserved Under Equipotent Doses of Isoflurane. 13, 1–13. doi:10.3389/fnsys.2019.00019.

Akeju, O., Song, A. H., Hamilos, A. E., Pavone, K. J., Flores, F. J., Brown, E. N., and Purdon, P. L. (2016). Electroencephalogram signatures of ketamine anesthesia-induced unconsciousness. *Clin. Neurophysiol.* 127, 2414–2422. doi:10.1016/j.clinph.2016.03.005.

Alam, N. M., Altimus, C. M., Douglas, R. M., Hattar, S., and Prusky, G. T. (2015). Photoreceptor regulation of spatial visual behavior. *Investig. Ophthalmol. Vis. Sci.* 56, 1842–1849. doi:10.1167/iovs.14-15644.

Alamia, A. and VanRullen, R. (2018). Alpha oscillations and travelling waves: signatures of predictive coding? 1–26. doi:10.1101/464933.

Alkire, M. T., Haier, R. J., and Fallon, J. H. (2000). Toward a Unified Theory of Narcosis: Brain Imaging Evidence for a Thalamocortical Switch as the Neurophysiologic Basis of Anesthetic-Induced Unconsciousness. *Conscious. Cogn.* 9, 370–386. doi:10.1006/ccog.1999.0423.

Alkire, M. T., Hudetz, A. G., and Tononi, G. (2008). Consciousness and Anesthesia. *Science (80-.).* 322, 876–880. doi:10.1126/science.1149213.

Alkire, M. T. and Miller, J. (2005). General anesthesia and the neural correlates of consciousness. *Prog. Brain Res.* 150, 229–244. doi:10.1016/S0079-6123(05)50017-7.

Amzica, F. (2009). Basic physiology of burst-suppression. 50, 38–39. doi:10.1111/j.1528-1167.2009.02345.x.

Andermann, M. L., Kerlin, A. M., Roumis, D. K., Glickfeld, L. L., and Reid, R. C. (2011a). Functional specialization of mouse higher visual cortical areas. *Neuron* 72, 1025–1039. doi:10.1016/j.neuron.2011.11.013.

Andermann, M. L., Kerlin, A. M., Roumis, D. K., Glickfeld, L. L., and Reid, R. C. (2011b). Functional specialization of mouse higher visual cortical areas. *Neuron* 72, 1025–1039. doi:10.1016/j.neuron.2011.11.013.

Arena, A., Lamanna, J., Gemma, M., Ripamonti, M., Ravasio, G., Zimarino, V., De Vitis, A., Beretta, L., and Malgaroli, A. (2017). Linear transformation of the encoding mechanism for light intensity underlies the paradoxical enhancement of cortical visual responses by sevoflurane. *J. Physiol.* 595, 321–339. doi:10.1113/JP272215.

Arieli, A., Sterkin, A., Grinvald, A., and Aertsen, A. (1996). Dynamics of Ongoing Activity : Explanation of the Large Variability in Evoked Cortical Responses. *Science (80-.).*

Aston-Jones, G. and Cohen, J. D. (2005). AN INTEGRATIVE THEORY OF LOCUS COERULEUS-NOREPINEPHRINE FUNCTION: Adaptive Gain and Optimal Performance. *Annu. Rev. Neurosci.* 28, 403–450. doi:10.1146/annurev.neuro.28.061604.135709.

Bahramisharif, A., van Gerven, M. A. J., Aarnoutse, E. J., Mercier, M. R., Schwartz, T. H., Foxe, J. J., Ramsey, N. F., and Jensen, O. (2013). Propagating neocortical gamma bursts are coordinated by traveling alpha waves. *J. Neurosci.* 33, 18849–18854. doi:10.1523/JNEUROSCI.2455-13.2013.

Bai, D., Pennefather, P. S., MacDonald, J. F., and Orser, B. A. (1999). The General Anesthetic Propofol Slows Deactivation and Desensitization of GABA A Receptors. *J. Neurosci.* 19, 10635–10646. doi:10.1523/JNEUROSCI.19-24-10635.1999.

Banks, M. I. and Pearce, R. A. (1999). Dual actions of volatile anesthetics on GABAAIPSCs: Dissociation of blocking and prolonging effects. *Anesthesiology*. doi:10.1097/00000542-199901000-00018.

Bastos, A. M., Vezoli, J., Bosman, C. A., Schoffelen, J. M., Oostenveld, R., Dowdall, J. R., DeWeerd, P., Kennedy, H., and Fries, P. (2015). Visual areas exert feedforward and feedback influences through distinct frequency channels. *Neuron* 85, 390–401. doi:10.1016/j.neuron.2014.12.018.

Benucci, A., Frazor, R. A., and Carandini, M. (2007). Standing Waves and Traveling Waves Distinguish Two Circuits in Visual Cortex. *Neuron* 55, 103–117. doi:10.1016/j.neuron.2007.06.017.

Besserve, M., Lowe, S. C., Logothetis, N. K., Schölkopf, B., and Panzeri, S. (2015). Shifts of Gamma Phase across Primary Visual Cortical Sites Reflect Dynamic Stimulus-Modulated Information Transfer. *PLoS Biol.* 13, 1–29. doi:10.1371/journal.pbio.1002257.

Blain-Moraes, S., Lee, U., Ku, S., Noh, G., and Mashour, G. A. (2014). Electroencephalographic effects of ketamine on power, cross-frequency coupling, and connectivity in the alpha bandwidth. *Front. Syst. Neurosci.* 8, 114. doi:10.3389/fnsys.2014.00114.

Bollimunta, A., Chen, Y., Schroeder, C. E., and Ding, M. (2008). Neuronal mechanisms of cortical alpha oscillations in awake-behaving macaques. *J. Neurosci.* 28, 9976–9988. doi:10.1523/JNEUROSCI.2699-08.2008.

Bollimunta, A., Mo, J., Schroeder, C. E., and Ding, M. (2011). Neuronal mechanisms and attentional modulation of corticothalamic alpha oscillations. *J. Neurosci.* 31, 4935–4943. doi:10.1523/JNEUROSCI.5580-10.2011.

Boly, M., Garrido, M. I., Gosseries, O., Bruno, M.-A., Boveroux, P., Schnakers, C., Massimini, M., Litvak, V., Laureys, S., and Friston, K. (2011). Preserved Feedforward But Impaired Top-Down Processes in the Vegetative State. *Science (80-.).* 332, 177–190. doi:10.4159/harvard.9780674368446.c10.

Boly, M., Moran, R., Murphy, M., Boveroux, P., Bruno, M.-A., Noirhomme, Q., Ledoux1, D., Bonhomme, V., Jean-François, and Brichant4, Giulio Tononi3, Steven Laureys1, an K. F. (2012). Connectivity changes underlying spectral EEG changes during propofol-induced loss of consciousness Mélanie. *J. Neurosci.* 76, 211–220. doi:10.1007/s11103-011-9767-z.Plastid.

Bosman, C. A., Schoffelen, J. M., Brunet, N., Oostenveld, R., Bastos, A. M., Womelsdorf, T., Rubehn, B., Stieglitz, T., De Weerd, P., and Fries, P. (2012). Attentional Stimulus Selection through Selective Synchronization between Monkey Visual Areas. *Neuron* 75, 875–888. doi:10.1016/j.neuron.2012.06.037.

Bringuier, V., Chavane, F., Glaeser, L., and Frégnac, Y. (1999). Horizontal propagation of visual activity in the synaptic integration field of area 17 neurons. *Science (80-.).* 283, 695–699. doi:10.1126/science.283.5402.695.

Brown, E. N., Purdon, P. L., and Dort, C. J. Van (2012). General Anesthesia and Altered States of Arousal: A Systems Neuroscience Analysis. *Annu. Rev. Neurosci.* 34, 601–628. doi:10.1146/annurev-neuro-060909-153200.General.

Brumberg, J. C., Hamzei-Sichani, F., and Yuste, R. (2003). Morphological and physiological characterization of layer VI corticofugal neurons of mouse primary visual cortex. *J. Neurophysiol.* 89, 2854–2867. doi:10.1152/jn.01051.2002.

Buffalo, E. A., Fries, P., Landman, R., Buschman, T. J., and Desimone, R. (2011). Laminar differences in gamma and alpha coherence in the ventral stream. *Proc. Natl. Acad. Sci. U. S. A.* 108, 11262–11267. doi:10.1073/pnas.1011284108.

Burgess, C. P., Lak, A., Steinmetz, N. A., Zatka-haas, P., Bai Reddy, C., Jacobs, E. A. K. K., Linden, J. F., Paton, J. J., Ranson, A., Schröder, S., Soares, S., Wells, M. J., Wool, L. E., Harris, K. D., Carandini, M., Reddy, B., Jacobs, E. A. K. K., Linden, J. F., Paton, J. J., et al. (2017). High-Yield Methods for Accurate Two-Alternative Visual Psychophysics in Head-Fixed Mice. *Cell Rep.* 20, 2513–2524. doi:10.1016/j.celrep.2017.08.047.

Burkhalter, A. (1989). Intrinsic connections of rat primary visual cortex: Laminar organization of axonal projections. *J. Comp. Neurol.* 279, 171–186. doi:10.1002/cne.902790202.

Burkitt, G. R., Silberstein, R. B., Cadusch, P. J., and Wood, A. W. (2000). Steady-state visual evoked potentials and travelling waves. *Clin. Neurophysiol.* 111, 246–258. doi:10.1016/S1388-2457(99)00194-7.

Busse, L. (2018). The Mouse Visual System and Visual Perception. *Handb. Behav. Neurosci.* 27, 53–68. doi:10.1016/B978-0-12-812012-5.00004-5.

Buzsáki, G., Anastassiou, C. A., and Koch, C. (2012). The origin of extracellular fields and currents — EEG , ECoG , LFP and spikes. *Nat. Publ. Gr.* 13, 407–420. doi:10.1038/nrn3241.

Carandini, M., Shimaoka, D., Rossi, L. F., Sato, T. K., Benucci, A., and Knopfel, T. (2015). Imaging the Awake Visual Cortex with a Genetically Encoded Voltage Indicator. *J. Neurosci.* 35, 53–63. doi:10.1523/JNEUROSCI.0594-14.2015.

Cardin, J. A. (2016a). Snapshots of the Brain in Action: Local Circuit Operations through the Lens of γ Oscillations. *J. Neurosci.* 36, 10496–10504. doi:10.1523/JNEUROSCI.1021-16.2016.

Cardin, J. A. (2016b). Snapshots of the Brain in Action: Local Circuit Operations through the Lens

of γ Oscillations. *J. Neurosci.* 36, 10496–10504. doi:10.1523/JNEUROSCI.1021-16.2016.

Cardin, J. A., Carlén, M., Meletis, K., Knoblich, U., Zhang, F., Deisseroth, K., Tsai, L. H., and Moore, C. I. (2009). Driving fast-spiking cells induces gamma rhythm and controls sensory responses. *Nature* 459, 663–667. doi:10.1038/nature08002.

Casali, A. G., Gosseries, O., Rosanova, M., Boly, M., Sarasso, S., Casali, K. R., Casarotto, S., Bruno, M.-A., Laureys, S., Tononi, G., and Massimini, M. (2013). A Theoretically Based Index of Consciousness Independent of Sensory Processing and Behavior. *Sci. Transl. Med.* 5, 198ra105-198ra105. doi:10.1126/scitranslmed.3006294.

Chen, X., Shu, S., and Bayliss, D. A. (2009). HCN1 Channel Subunits Are a Molecular Substrate for Hypnotic Actions of Ketamine. *J. Neurosci.* 29, 600–609. doi:10.1523/JNEUROSCI.3481-08.2009.

Childers, D. G., Perry, N. W., Fischler, I. A., Boaz, T., and A, A. A. (1987). Event-related potentials: a critical review of methods for single-trial detection. *Crit. Reciews Biomed. Eng.* 14, 185–200.

Ching, S., Cimenser, A., Purdon, P. L., Brown, E. N., and Kopell, N. J. (2010). Thalamocortical model for a propofol-induced -rhythm associated with loss of consciousness. *Proc. Natl. Acad. Sci.* 107, 22665–22670. doi:10.1073/pnas.1017069108.

Churchland, M. M. and Abbott, L. F. (2012). Two layers of neural variability. *Nat. Neurosci.* 15, 1472–1474. doi:10.1038/nn.3247.

Churchland, M. M., Yu, B. M., Cunningham, J. P., Sugrue, L. P., Cohen, M. R., Corrado, G. S., Newsome, W. T., Clark, A. M., Hosseini, P., Scott, B. B., Bradley, D. C., Smith, M. A., Kohn, A., Movshon, J. A., Armstrong, K. M., Moore, T., Chang, S. W., Snyder, L. H., Lisberger, S. G., et al. (2010). Stimulus onset quenches neural variability: A widespread cortical phenomenon. *Nat. Neurosci.* 13, 369–378. doi:10.1038/nn.2501.

Cohen, Mike, X. (2014). *Analyzing Neural Time Series Data: Theory and Practice*. MIT Press.

Darrow, C. W. and Hicks, R. G. (1965). Interarea Electroencephalographic Phase Relationships Following Sensory and Ideational Stimuli. *Psychophysiology* 1, 337–346. doi:10.1111/j.1469-8986.1965.tb03266.x.

Davis, Z. W., Muller, L., Martinez-Trujillo, J., Sejnowski, T., and Reynolds, J. H. (2020). Spontaneous travelling cortical waves gate perception in behaving primates. *Nature* 587, 432–436. doi:10.1038/s41586-020-2802-y.

Del Cul, A., Baillet, S., and Dehaene, S. (2007). Brain dynamics underlying the nonlinear threshold for access to consciousness. *PLoS Biol.* 5, 2408–2423. doi:10.1371/journal.pbio.0050260.

Denman, D. J., Luviano, J. A., Ollerenshaw, D. R., Cross, S., Williams, D., Buice, M. A., Olsen, S. R., and Reid, R. C. (2018). Mouse color and wavelength-specific luminance contrast sensitivity are non- uniform across visual space. *Elife* 7, 1–16. doi:10.7554/eLife.31209.

Destexhe, A., Contreras, D., and Steriade, M. (1999). Spatiotemporal analysis of local field potentials and unit discharges in cat cerebral cortex during …. *J. Neurosci.* 19, 4595–4608. doi:10.1016/j.mri.2010.01.001.

Dougherty, K., Cox, M. A., Ninomiya, T., Leopold, D. A., and Maier, A. (2017). Ongoing alpha

activity in V1 regulates visually driven spiking responses. *Cereb. Cortex* 27, 1113–1124. doi:10.1093/cercor/bhv304.

Douglas, R. J. and Martin, K. A. C. (2004). Neuronal Circuits of the Neocortex. *Annu. Rev. Neurosci.* 27, 419–451. doi:10.1146/annurev.neuro.27.070203.144152.

Douglas, R. J. and Martin, K. A. C. (2007). Mapping the matrix: the ways of neocortex. *Neuron* 56, 226–238. doi:10.1016/j.neuron.2007.10.017.

Eckenhoff, M. F. (2002a). Multiple Specific Binding Targets for Inhaled Anesthetics in the Mammalian Brain. *J. Pharmacol. Exp. Ther.* 300, 172–179. doi:10.1124/jpet.300.1.172.

Eckenhoff, M. F. (2002b). Multiple Specific Binding Targets for Inhaled Anesthetics in the Mammalian Brain. *J. Pharmacol. Exp. Ther.* 300, 172–179. doi:10.1124/jpet.300.1.172.

Eckenhoff, M. F. and Eckenhoff, R. G. (1998). Quantitative autoradiography of halothane binding in rat brain. *J. Pharmacol. Exp. Ther.* 285, 371–6. Available at: http://jpet.aspetjournals.org/content/285/1/371.short%5Cnhttp://www.ncbi.nlm.nih.gov/pubmed/9536033.

Einstein, M. C., Polack, P.-O. O., Tran, D. T., and Golshani, P. (2017). Visually evoked 3-5 Hz membrane potential oscillations reduce the responsiveness of visual cortex neurons in awake behaving mice. *J. Neurosci.* 37, 5084–5098. doi:10.1523/JNEUROSCI.3868-16.2017.

Eldar, E., Cohen, J. D., and Niv, Y. (2013). The effects of neural gain on attention and learning. *Nat. Neurosci.* 16, 1146–1153. doi:10.1038/nn.3428.

Engel, A. K., Fries, P., and Singer, W. (2001). DYNAMIC PREDICTIONS : OSCILLATIONS AND SYNCHRONY IN TOP – DOWN PROCESSING. *Nat. Rev. Neurosci.* 2, 704–716. doi:10.1038/35094565.

Ermentrout, G. B. and Kleinfeld, D. (2001). Traveling electrical waves in cortex: Insights from phase dynamics and speculation on a computational role. *Neuron* 29, 33–44. doi:10.1016/S0896-6273(01)00178-7.

Feldmeyer, D., Lübke, J., and Sakmann, B. (2006). Efficacy and connectivity of intracolumnar pairs of layer 2/3 pyramidal cells in the barrel cortex of juvenile rats. *J. Physiol.* 575, 583–602. doi:10.1113/jphysiol.2006.105106.

Feldmeyer, D., Lübke, J., Silver, R. A., and Sakmann, B. (2002). Synaptic connections between layer 4 spiny neurone-layer 2/3 pyramidal cell pairs in juvenile rat barrel cortex: Physiology and anatomy of interlaminar signalling within a cortical column. *J. Physiol.* 538, 803–822. doi:10.1113/jphysiol.2001.012959.

Felleman, D. J. and Van Essen, D. C. (1991). Distributed hierarchical processing in the primate cerebral cortex. *Cereb. Cortex* 1, 1–47. doi:10.1093/cercor/1.1.1-a.

Ferezou, I., Bolea, S., and Petersen, C. C. H. (2006). Visualizing the Cortical Representation of Whisker Touch: Voltage-Sensitive Dye Imaging in Freely Moving Mice. *Neuron* 50, 617–629. doi:10.1016/j.neuron.2006.03.043.

Ferrarelli, F., Massimini, M., Sarasso, S., Casali, A., Riedner, B. A., Angelini, G., Tononi, G., and Pearce, R. A. (2010). Breakdown in cortical effective connectivity during midazolam-induced loss of consciousness. *Proc Natl Acad Sci U S A* 107, 2681–2686.

doi:10.1073/pnas.0913008107.

Ferron, J.-F. J., Kroeger, D., Chever, O., and Amzica, F. (2009a). Cortical Inhibition during Burst Suppression Induced with Isoflurane Anesthesia. *J. Neurosci.* 29, 9850–9860. doi:10.1523/JNEUROSCI.5176-08.2009.

Ferron, J.-F., Kroeger, D., Chever, O., and Amzica, F. (2009b). Cortical Inhibition during Burst Suppression Induced with Isoflurane Anesthesia. *J. Neurosci.* 29, 9850–9860. doi:10.1523/JNEUROSCI.5176-08.2009.

Fisher, N, I. (1995). Statistical Analysis of Circular Data. *Cambridge Univ. Press*. Available at: https://www.google.com/books/edition/Statistical_Analysis_of_Circular_Data/wGPj3EoFdJwC?hl=en&gbpv=0 [Accessed July 31, 2021].

Franklin, Keith, B., J. and Paxinos, G. (2007). *The Mouse Brain In Stereotaxic Coordinates, Third Edition*. Third. Academic Press.

Franks, N. P. (2008). General anaesthesia: From molecular targets to neuronal pathways of sleep and arousal. *Nat. Rev. Neurosci.* 9, 370–386. doi:10.1038/nrn2372.

Freeman, J. A. and Nicholson, C. (1974). Experimental Optimization of Current Source-Density Technique for Anuran Cerebellum. *J. Neurophysiol.*, 369–382. doi:10.3109/00016486809122149.

Friedman, E. B., Sun, Y., Moore, J. T., Hung, H. T., Meng, Q. C., Perera, P., Joiner, W. J., Thomas, S. A., Eckenhoff, R. G., Sehgal, A., and Kelz, M. B. (2010). A conserved behavioral state barrier impedes transitions between anesthetic-induced unconsciousness and wakefulness: Evidence for neural inertia. *PLoS One* 5. doi:10.1371/journal.pone.0011903.

Fries, P., Neuenschwander, S., Engel, A. K., Goebel, R., and Singer, W. (2001). Rapid feature selective neuronal synchronization through correlated latency shifting. *Nat. Neurosci.* 4, 194–200. doi:10.1038/84032.

Friston, K. (2008). Hierarchical models in the brain. *PLoS Comput. Biol.* 4. doi:10.1371/journal.pcbi.1000211.

Friston, K. and Buzsáki, G. (2016). The Functional Anatomy of Time: What and When in the Brain. *Trends Cogn. Sci.* 20, 500–511. doi:10.1016/j.tics.2016.05.001.

Fu, Y., Tucciarone, J. M., Espinosa, J. S., Sheng, N., Darcy, D. P., Nicoll, R. A., Huang, Z. J., and Stryker, M. P. (2014). A cortical circuit for gain control by behavioral state. *Cell* 156, 1139–1152. doi:10.1016/j.cell.2014.01.050.

Gabriel, A. and Eckhorn, R. (2003). A multi-channel correlation method detects traveling γ-waves in monkey visual cortex. *J. Neurosci. Methods* 131, 171–184. doi:10.1016/j.jneumeth.2003.08.008.

Ganguly, S., Panetta, J. C., Roberts, J. K., and Schuetz, E. G. (2018). Ketamine pharmacokinetics and pharmacodynamics are altered by P-glycoprotein and breast cancer resistance protein efflux transporters in mice. *Drug Metab. Dispos.* 46, 1014–1022. doi:10.1124/dmd.117.078360.

Gao, X., Xu, W., Wang, Z., Takagaki, K., Li, B., and Wu, J. Y. (2012). Interactions between two propagating waves in rat visual cortex. *Neuroscience* 216, 57–69.

doi:10.1016/j.neuroscience.2012.04.062.

Garcia, P. S., Kolesky, S. E., and Jenkins, A. (2010). General Anesthetic Actions on GABA A Receptors. 2–9.

Garrett, M. E., Nauhaus, I., Marshel, J. H., and Callaway, E. M. (2014). Topography and Areal Organization of Mouse Visual Cortex. *J. Neurosci.* 34, 12587–12600. doi:10.1523/JNEUROSCI.1124-14.2014.

Gibbs, F., Gibbs, E., Lennox, W. (1937). Effect On The Electro-Encephalogram Of Certain Drugs Which Influence Nervous Activity. *Arch. Intern. Med* 60, 154–166. doi:10.1136/bmjspcare-2016-001226.

Gilzenrat, M. S., Nieuwenhuis, S., Jepma, M., and Cohen, J. D. (2010). Pupil diameter tracks changes in control state predicted by the adaptive gain theory of locus coeruleus function. *Cogn. Affect. Behav. Neurosci.* 10, 252–269. doi:10.3758/CABN.10.2.252.

Girard, P., Hupé, J. M., and Bullier, J. (2001). Feedforward and feedback connections between areas V1 and V2 of the monkey have similar rapid conduction velocities. *J. Neurophysiol.* 85, 1328–1331. doi:10.1152/jn.2001.85.3.1328.

Glickfeld, L. L., Andermann, M. L., Bonin, V., and Reid, R. C. (2013). Cortico-cortical projections in mouse visual cortex are functionally target specific. *Nat. Neurosci.* 16, 219–226. doi:10.1038/nn.3300.

Goldman, S., Vivian, W. E., Chien, C. K., and Bowes, H. N. (1948). Travelling Waves in the Brain. *Science (80-.).* 24, 720–723.

Grinvald, A., Lieke, E. E., Frostig, R. D., and Hildesheim, R. (1994). Cortical point-spread function and long-range lateral interactions revealed by real-time optical imaging of macaque monkey primary visual cortex. *J. Neurosci.* 14, 2545–2568. doi:10.1523/jneurosci.14-05-02545.1994.

Hales, T. G. and Lambert, J. J. (1991). The actions of propofol on inhibitory amino acid receptors of bovine adrenomedullary chromaffin cells and rodent central neurones. *Br. J. Pharmacol.* 104, 619–628. doi:10.1111/j.1476-5381.1991.tb12479.x.

Hall, A. C., Lieb, W. R., and Franks, N. P. (1994). Stereoselective and non-stereoselective actions of isoflurane on the GABAA receptor. *Br. J. Pharmacol.* 112, 906–910.

Hangya, B., Tihanyi, B. T., Entz, L., Fabó, D., Eross, L., Wittner, L., Jakus, R., Varga, V., Freund, T. F., and Ulbert, I. (2011). Complex propagation patterns characterize human cortical activity during slow-wave sleep. *J. Neurosci.* 31, 8770–8779. doi:10.1523/JNEUROSCI.1498-11.2011.

Hao, X., Ou, M., Zhang, D., Zhao, W., Yang, Y., Liu, J., Yang, H., Zhu, T., Li, Y., and Zhou, C. (2020). The Effects of General Anesthetics on Synaptic Transmission. *Curr. Neuropharmacol.* 18, 936–965. doi:10.2174/1570159x18666200227125854.

Hemmings, H. C., Riegelhaupt, P. M., Kelz, M. B., Solt, K., Eckenhoff, R. G., Orser, B. A., and Goldstein, P. A. (2019). Towards a Comprehensive Understanding of Anesthetic Mechanisms of Action: A Decade of Discovery. *Trends Pharmacol. Sci.* 40, 464–481. doi:10.1016/j.tips.2019.05.001.

Herring, B. E., Xie, Z., Marks, J., and Fox, A. P. (2009). Isoflurane Inhibits the Neurotransmitter

Release Machinery. *https://doi.org/10.1152/jn.00252.2009* 102, 1265–1273. doi:10.1152/JN.00252.2009.

Hovde, K., Gianatti, M., Witter, M. P., and Whitlock, J. R. (2019). Architecture and organization of mouse posterior parietal cortex relative to extrastriate areas. *Eur. J. Neurosci.* 49, 1313–1329. doi:10.1111/ejn.14280.

Hubel, D. H. and Wiesel, T. N. (1962). Receptive fields, binocular interaction and functional architecture in the cat's visual cortex. *J. Physiol.* 160, 106-154.2. doi:10.1523/JNEUROSCI.1991-09.2009.

Hudetz, A. G. (2009). Feedback suppression in anesthesia. Is it reversible? *Conscious. Cogn.* 18, 1079–1081. doi:10.1016/j.concog.2009.08.004.

Hudetz, A. G. and Imas, O. A. (2007). Burst activation of the cerebral cortex by flash stimuli during isoflurane anesthesia in rats. *Anesthesiology* 107, 983–991. doi:10.1097/01.anes.0000291471.80659.55.

Hudetz, A. G., Vizuete, J. A., and Imas, O. A. (2009). Desflurane selectively suppresses long-latency cortical neuronal response to flash in the rat. *Anesthesiology* 111, 231–9. doi:10.1097/ALN.0b013e3181ab671e.

Hudson, A. E., Calderon, D. P., Pfaff, D. W., and Proekt, A. (2014). Supporting Information: Recovery of consciousness is mediated by a network of discrete metastable activity states. *Proc. Natl. Acad. Sci.* 111, 1–9. doi:10.1073/pnas.1408296111.

Hughes, J. R. (1995). The Phenomenon of Travelling Waves: A Review. *Clin. EEG Neurosci.* 26, 1–6. doi:10.1177/155005949502600103.

Imas, O. A., Ropella, K. M., Ward, B. D., Wood, J. D., and Hudetz, A. G. (2005a). Volatile anesthetics disrupt frontal-posterior recurrent information transfer at gamma frequencies in rat. *Neurosci. Lett.* 387, 145–150. doi:10.1016/j.neulet.2005.06.018.

Imas, O. A., Ropella, K. M., Ward, B. D., Wood, J. D., and Hudetz, A. G. (2005b). Volatile anesthetics enhance flash-induced gamma oscillations in rat visual cortex. *Anesthesiology* 102, 937–947. doi:10.1097/00000542-200505000-00012.

Ito, J., Roy, S., Liu, Y., Cao, Y., Fletcher, M., Lu, L., Boughter, J. D., Grün, S., and Heck, D. H. (2014). Whisker barrel cortex delta oscillations and gamma power in the awake mouse are linked to respiration. *Nat. Commun.* 5, 1–10. doi:10.1038/ncomms4572.

Jeong, S. O., Ko, T. W., and Moon, H. T. (2002). Time-Delayed Spatial Patterns in a Two-Dimensional Array of Coupled Oscillators. *Phys. Rev. Lett.* 89, 1–4. doi:10.1103/PhysRevLett.89.154104.

Jones, E. G. (1985). *The Thalamus.* 1st ed. Boston, MA: Springer US doi:10.1007/978-1-4615-1749-8.

Jones, M. V. and Harrison, N. L. (1993). Effects of volatile anesthetics on the kinetics of inhibitory postsynaptic currents in cultured rat hippocampal neurons. *J. Neurophysiol.* 70, 1339–1349. doi:10.1152/jn.1993.70.4.1339.

Jordan, D., Ilg, R., Riedl, V., Schorer, A., Grimberg, S., Neufang, S., Omerovic, A., Berger, S., Untergehrer, G., Preibisch, C., Schulz, E., Schuster, T., Schröter, M., Spoormaker, V., Zimmer, C., Hemmer, B., Wohlschläger, A., Kochs, E. F., and Schneider, G. (2013).

Simultaneous Electroencephalographic and Functional Magnetic Resonance Imaging Indicate Impaired Cortical Top–Down Processing in Association with Anesthetic-induced Unconsciousness. *Anesthesiology* 119, 1031–1042. doi:10.1097/ALN.0b013e3182a7ca92.

Jurd, R., Arras, M., Lambert, S., Drexler, B., Siegwart, R., Crestani, F., Zaugg, M., Vogt, K. E., Ledermann, B., Antkowiak, B., and Rudolph, U. (2003). General anesthetic actions in vivo strongly attenuated by a point mutation in the GABA A receptor β3 subunit. *FASEB J.* 17, 250–252. doi:10.1096/fj.02-0611fje.

Kelz, M. B. and Mashour, G. A. (2019). The Biology of General Anesthesia from Paramecium to Primate. *Curr. Biol.* 29, R1199–R1210. doi:10.1016/j.cub.2019.09.071.

Kim, M., Mashour, G. A., Moraes, S., Vanini, G., Tarnal, V., Janke, E., Hudetz, A. G., and Lee, U. (2016). Functional and Topological Conditions for Explosive Synchronization Develop in Human Brain Networks with the Onset of Anesthetic-Induced Unconsciousness. *Front. Comput. Neurosci.* 10, 1–15. doi:10.3389/fncom.2016.00001.

King, J.-R. and Wyart, V. (2021). The Human Brain Encodes a Chronicle of Visual Events at each Instant of Time thanks to the Multiplexing of Traveling Waves. *J. Neurosci.*, JN-RM-2098-20. doi:10.1523/jneurosci.2098-20.2021.

Kisley, M. a and Gerstein, G. L. (1999). Trial-to-trial variability and state-dependent modulation of auditory-evoked responses in cortex. *J. Neurosci.* 19, 10451–10460.

Kopell, N., Ermentrout, G. B., Whittington, M. A., and Traub, R. D. (2000). Gamma rhythms and beta rhythms have different synchronization properties. *Proc. Natl. Acad. Sci.* 97, 1867–1872. doi:10.1073/pnas.97.4.1867.

Krasowski, M. D., Koltchine, V. V, Rick, C. E., Ye, Q., Finn, S. E., and Harrison, N. L. (1998a). Propofol and other intravenous anesthetics have sites of action on the gamma-aminobutyric acid type A receptor distinct from that for isoflurane. *Mol. Pharmacol.* 53, 530–8. doi:10.1124/mol.53.3.530.

Krasowski, M. D., Koltchine, V. V, Rick, C. E., Ye, Q., Finn, S. E., and Harrison, N. L. (1998b). Propofol and other intravenous anesthetics have sites of action on the gamma-aminobutyric acid type A receptor distinct from that for isoflurane. *Mol. Pharmacol.* 53, 530–8. doi:10.1124/mol.53.3.530.

Krieger, P., Kuner, T., and Sakmann, B. (2007). Synaptic connections between layer 5B pyramidal neurons in mouse somatosensory cortex are independent of apical dendrite bundling. *J. Neurosci.* 27, 11473–11482. doi:10.1523/JNEUROSCI.1182-07.2007.

Kroeger, D. and Amzica, F. (2007). Hypersensitivity of the Anesthesia-Induced Comatose Brain. *J. Neurosci.* 27, 10597–10607. doi:10.1523/JNEUROSCI.3440-07.2007.

Ku, S. W., Lee, U. C., Noh, G. J., Jun, I. G., and Mashour, G. A. (2011). Preferential inhibition of frontal-to-parietal feedback connectivity is a neurophysiologic correlate of general anesthesia in surgical patients. *PLoS One* 6, 1–9. doi:10.1371/journal.pone.0025155.

Kumbhani, R. D., Nolt, M. J., and Palmer, L. A. (2007). Precision, Reliability, and Information-Theoretic Analysis of Visual Thalamocortical Neurons. *J. Neurophysiol.* 98, 2647–2663. doi:10.1152/jn.00900.2006.

Lee, UnCheol and Mashour, G. A. (2018). Role of Network Science in the Study of Anesthetic State Transitions. *Anesthesiology* 129, 1029–1044. doi:10.1097/ALN.0000000000002228.

Lee, A. M., Hoy, J. L., Bonci, A., Wilbrecht, L., Stryker, M. P., and Niell, C. M. (2014). Identification of a brainstem circuit regulating visual cortical state in parallel with locomotion. *Neuron* 83, 455–466. doi:10.1016/j.neuron.2014.06.031.

Lee, U., Kim, S., Noh, G. J., Choi, B. M., Hwang, E., and Mashour, G. A. (2009). The directionality and functional organization of frontoparietal connectivity during consciousness and anesthesia in humans. *Conscious. Cogn.* 18, 1069–1078. doi:10.1016/j.concog.2009.04.004.

Lee, U., Ku, S., Noh, G., Baek, S., Choi, B., and Mashour, G. A. (2013a). Disruption of Frontal–Parietal Communication by Ketamine, Propofol, and Sevofluran. *Anesthesiology* 118, 1264–1275.

Lee, U., Ku, S., Noh, G., Baek, S., Choi, B., and Mashour, G. A. (2013b). Disruption of Frontal–Parietal Communication by Ketamine, Propofol, and Sevoflurane. *Anesthesiology* 118, 1264–1275.

Lein, E. S., Hawrylycz, M. J., Ao, N., Ayres, M., Bensinger, A., Bernard, A., Boe, A. F., Boguski, M. S., Brockway, K. S., Byrnes, E. J., Chen, L., Chen, L., Chen, T. M., Chin, M. C., Chong, J., Crook, B. E., Czaplinska, A., Dang, C. N., Datta, S., et al. (2007a). Genome-wide atlas of gene expression in the adult mouse brain. *Nature* 445, 168–176. doi:10.1038/nature05453.

Lein, E. S., Hawrylycz, M. J., Ao, N., Ayres, M., Bensinger, A., Bernard, A., Boe, A. F., Boguski, M. S., Brockway, K. S., Byrnes, E. J., Chen, L., Chen, L., Chen, T. M., Chin, M. C., Chong, J., Crook, B. E., Czaplinska, A., Dang, C. N., Datta, S., et al. (2007b). Genome-wide atlas of gene expression in the adult mouse brain. *Nature* 445, 168–176. doi:10.1038/nature05453.

Leslie, K., Chan, M. T. V., Myles, P. S., Forbes, A., and McCulloch, T. J. (2010). Posttraumatic stress disorder in aware patients from the B-aware trial. *Anesth. Analg.* 110, 823–828. doi:10.1213/ANE.0b013e3181b8b6ca.

Leung, L. S., Luo, T., Ma, J., and Herrick, I. (2014). Brain areas that influence general anesthesia. *Prog. Neurobiol.* 122, 24–44. doi:10.1016/J.PNEUROBIO.2014.08.001.

Li, K. Y., Guan, Y.-Z., Krnjevic´, K., Krnjevic´, K., and Ye, J. H. (2009). Propofol Facilitates Glutamatergic Transmission to Neurons of the Ventrolateral Preoptic Nucleus. Available at: http://pubs.asahq.org/anesthesiology/article-pdf/111/6/1271/249369/0000542-200912000-00022.pdf.

Liberati, D., Bertolini, L., and Colombo, D. C. (1991). Parametric method for the detection of inter- and intrasweep variability in VEP processing. *Med. Biol. Eng. Comput.* 29, 159–166. doi:10.1007/BF02447102.

Liu, X., Lauer, K. K., Ward, B. D., Rao, S. M., Li, S.-J., and Hudetz, A. G. (2012). Propofol Disrupts Functional Interactions between Sensory and High-Order Processing of Auditory Verbal Memory Xiaolin. *Hum. Brain Mapp.* 33, 2487–2497. doi:10.1007/s11103-011-9767-z.Plastid.

LJ, V., PS, G., H, H., and MI, B. (2019). Understanding the Effects of General Anesthetics on Cortical Network Activity Using Ex Vivo Preparations. *Anesthesiology* 130, 1049–1063. doi:10.1097/ALN.0000000000002554.

Lobo, I. A. and Harris, R. A. (2005). Sites of Alcohol and Volatile Anesthetic Action on Glycine Receptors. *Int. Rev. Neurobiol.* 65, 53–87. doi:10.1016/S0074-7742(04)65003-3.

Lu, J., Nelson, L. E., Franks, N., Maze, M., Chamberlin, N. L., and Saper, C. B. (2008a). Role of endogenous sleep-wake and analgesic systems in anesthesia. *J. Comp. Neurol.* 508, 648–662. doi:10.1002/cne.21685.

Lu, J., Nelson, L. E., Franks, N., Maze, M., Chamberlin, N. L., and Saper, C. B. (2008b). Role of endogenous sleep-wake and analgesic systems in anesthesia. *J. Comp. Neurol.* 508, 648–662. doi:10.1002/cne.21685.

Lyamzin, D. and Benucci, A. (2019). The mouse posterior parietal cortex: Anatomy and functions. *Neurosci. Res.* 140, 14–22. doi:10.1016/j.neures.2018.10.008.

Lydic Ralph, P. D. and Baghdoyan Helen A., P. D. (2005). Sleep, Anesthesiology, and the Neurobiology of Arousal State Control. *Anesthesiology* 103, 1268–1295. Available at: http://dx.doi.org/0000542-200512000-00024.

Mak-McCully, R. A., Rosen, B. Q., Rolland, M., Régis, J., Bartolomei, F., Rey, M., Chauvel, P., Cash, S. S., and Halgren, E. (2015). Distribution, amplitude, incidence, co-occurrence, and propagation of human K-complexes in focal transcortical recordings. *eNeuro* 2, 1–26. doi:10.1523/ENEURO.0028-15.2015.

Maksimow, A., Särkelä, M., Långsjö, J. W., Salmi, E., Kaisti, K. K., Yli-Hankala, A., Hinkka-Yli-Salomäki, S., Scheinin, H., and Jääskeläinen, S. K. (2006). Increase in high frequency EEG activity explains the poor performance of EEG spectral entropy monitor during S-ketamine anesthesia. *Clin. Neurophysiol.* 117, 1660–1668. doi:10.1016/j.clinph.2006.05.011.

Markov, N. T., Vezoli, J., Chameau, P., Falchier, A., Quilodran, R., Huissoud, C., Lamy, C., Misery, P., Giroud, P., Ullman, S., Barone, P., Dehay, C., Knoblauch, K., and Kennedy, H. (2014). Anatomy of hierarchy: Feedforward and feedback pathways in macaque visual cortex. *J. Comp. Neurol.* 522, 225–259. doi:10.1002/cne.23458.

Marshel, J. H., Garrett, M. E., Nauhaus, I., and Callaway, E. M. (2011a). Functional specialization of seven mouse visual cortical areas. *Neuron* 72, 1040–1054. doi:10.1016/j.neuron.2011.12.004.

Marshel, J. H., Garrett, M. E., Nauhaus, I., and Callaway, E. M. (2011b). Functional specialization of seven mouse visual cortical areas. *Neuron* 72, 1040–1054. doi:10.1016/j.neuron.2011.12.004.

Mashour, G. A. (2006). Integrating the science of consciousness and anesthesia. *Anesth. Analg.* 10Mashour, 975–982. doi:10.1213/01.ane.0000232442.69757.4a.

Mashour, G. A. (2014). Top-down mechanisms of anesthetic-induced unconsciousness. *Front. Syst. Neurosci.* 8, 1–10. doi:10.3389/fnsys.2014.00115.

Mashour, G. A. and Hudetz, A. G. (2017). Bottom-Up and Top-Down Mechanisms of General Anesthetics Modulate Different Dimensions of Consciousness. *Front. Neural Circuits* 11, 44. doi:10.3389/fncir.2017.00044.

Mashour, G. A., Orser, B. A., and Avidan, M. S. (2011). Intraoperative Awareness: From Neurobiology to Clinical Practice. *Anesthesiology* 114, 1218–1233. doi:10.1097/ALN.0b013e31820fc9b6.

Mashour, G. a., Shanks, A., Tremper, K. K., Kheterpal, S., Turner, C. R., Ramachandran, S. K., Picton, P., Schueller, C., Morris, M., Vandervest, J. C., Lin, N., and Avidan, M. S. (2012). Prevention of Intraoperative Awareness with Explicit Recall in an Unselected Surgical

Population. *Anesthesiology* 117, 717–725. doi:10.1097/ALN.0b013e31826904a6.

Massimini, M., Ferrarelli, F., Huber, R., Esser, S. K., Singh, H., and Tononi, G. (2005). Neuroscience: Breakdown of cortical effective connectivity during sleep. *Science (80-.).* 309, 2228–2232. doi:10.1126/science.1117256.

McKinstry-Wu, A. R., Wasilczuk, A. Z., Harrison, B. A., Bedell, V. M., Sridharan, M. J., Breig, J. J., Pack, M., Kelz, M. B., and Proekt, A. (2019). Analysis of stochastic fluctuations in responsiveness is a critical step toward personalized anesthesia. *Elife* 8, 1–25. doi:10.7554/eLife.50143.

Mejias, J. F., Murray, J. D., Kennedy, H., and Wang, X. J. (2016). Feedforward and feedback frequency-dependent interactions in a large-scale laminar network of the primate cortex. *Sci. Adv.* 2. doi:10.1126/sciadv.1601335.

Michalareas, G., Vezoli, J., van Pelt, S., Schoffelen, J. M., Kennedy, H., and Fries, P. (2016). Alpha-Beta and Gamma Rhythms Subserve Feedback and Feedforward Influences among Human Visual Cortical Areas. *Neuron* 89, 384–397. doi:10.1016/j.neuron.2015.12.018.

Miu, P. and Puil, E. (1989). Isoflurane-induced impairment of synaptic transmission in hippocampal neurons. *Exp.Brain Res.*

Monti, M. M., Lutkenhoff, E. S., Rubinov, M., Boveroux, P., Vanhaudenhuyse, A., Gosseries, O., Bruno, M. A., Noirhomme, Q., Boly, M., and Laureys, S. (2013). Dynamic Change of Global and Local Information Processing in Propofol-Induced Loss and Recovery of Consciousness. *PLoS Comput. Biol.* 9. doi:10.1371/journal.pcbi.1003271.

Moore, J. T., Chen, J., Han, B., Meng, Q. C., Veasey, S. C., Beck, S. G., and Kelz, M. B. (2012). Direct activation of sleep-promoting VLPO neurons by volatile anesthetics contributes to anesthetic hypnosis. *Curr. Biol.* 22, 2008–16. doi:10.1016/j.cub.2012.08.042.

Mountcastle, V. B. (the J. H. U. S. of M. (1957). Modality and Topographic Properties Neurons of Cat's Somatic Sensory Cortex. *J. Physiol.* doi:10.1152/jn.1957.20.4.408.

Muller, L., Chavane, F., Reynolds, J., and Sejnowski, T. J. (2018). Cortical travelling waves: Mechanisms and computational principles. *Nat. Rev. Neurosci.* 19, 255–268. doi:10.1038/nrn.2018.20.

Muller, L., Reynaud, A., Chavane, F., and Destexhe, A. (2014). The stimulus-evoked population response in visual cortex of awake monkey is a propagating wave. *Nat. Commun.* 5. doi:10.1038/ncomms4675.

Nagele, P., Mendel, J. B., Placzek, W. J., Scott, B. A., d'Avignon, D. A., and Crowder, C. M. (2005). Volatile Anesthetics Bind Rat Synaptic Snare Proteins. *Anesthesiology* 103, 768–778. doi:10.1097/00000542-200510000-00015.

Nauhaus, I., Busse, L., Carandini, M., and Ringach, D. L. (2009). Stimulus contrast modulates functional connectivity in visual cortex. 12, 70–76. doi:10.1038/nn.2232.

Nauhaus, I., Busse, L., Ringach, D. L., and Carandini, M. (2012). Robustness of traveling waves in ongoing activity of visual cortex. *J. Neurosci.* 32, 3088–3094. doi:10.1523/JNEUROSCI.5827-11.2012.

Nelson, L. E., Guo, T. Z., Lu, J., Saper, C. B., Franks, N. P., and Maze, M. (2002). The sedative component of anesthesia is mediated by GABAa receptors is an endogenous sleep

pathway. *Nature* 5, 979–989.

Nestvogel, D. B. and Mccormick, D. A. (2021). Visual Thalamocortical Mechanisms of Waking State Dependent Activity and Alpha Oscillations. *bioRxiv*, 1–40. Available at: https://doi.org/10.1101/2021.04.14.439865.

Niell, C. M. and Stryker, M. P. (2008). Highly Selective Receptive Fields in Mouse Visual Cortex. *J. Neurosci.* 28, 7520–7536. doi:10.1523/JNEUROSCI.0623-08.2008.

Niell, C. M. and Stryker, M. P. (2010). Modulation of Visual Responses by Behavioral State in Mouse Visual Cortex. *Neuron* 65, 472–479. doi:10.1016/j.neuron.2010.01.033.

Noda, T. and Takahashi, H. (2015). Anesthetic effects of isoflurane on the tonotopic map and neuronal population activity in the rat auditory cortex. *Eur. J. Neurosci.* 42, 2298–2311. doi:10.1111/ejn.13007.

Nourski, K. V., Banks, M. I., Steinschneider, M., Rhone, A. E., Kawasaki, H., Mueller, R. N., Todd, M. M., and Howard, M. A. (2017). Electrocorticographic delineation of human auditory cortical fields based on effects of propofol anesthesia. *Neuroimage* 152, 78–93. doi:10.1016/j.neuroimage.2017.02.061.

Olshausen, B. A. and Field, D. J. (2005). *How close are we to understanding V1?*. doi:10.1162/0899766054026639.

Osborn, I. and Sebeo, J. (2010). "Scalp block" during craniotomy: A classic technique revisited. *J. Neurosurg. Anesthesiol.* 22, 187–194. doi:10.1097/ANA.0b013e3181d48846.

Pachitariu, M., Steinmetz, N., Kadir, S., Carandini, M., and Harris, K. (2016). Fast and accurate spike sorting of high-channel count probes with KiloSort. *Adv. Neural Inf. Process. Syst.*, 4455–4463.

Pack, C. C., Berezovskii, V. K., and Born, R. T. (2001). Dynamic properties of neurons in cortical area MT in alert and anaesthetized macaque monkeys. *Nature* 414, 905–908. doi:10.1038/414905a.

Pearce, R. A. (1996). Volatile anaesthetic enhancement of paired-pulse depression investigated in the rat hippocampus in vitro. *J. Physiol.* doi:10.1113/jphysiol.1996.sp021349.

Peirson, S. N., Brown, L. A., Pothecary, C. A., Benson, L. A., and Fisk, A. S. (2018). Light and the laboratory mouse. *J. Neurosci. Methods* 300, 26–36. doi:10.1016/j.jneumeth.2017.04.007.

Pinto, L., Goard, M. J., Estandian, D., Xu, M., Kwan, A. C., Lee, S. H., Harrison, T. C., Feng, G., and Dan, Y. (2013). Fast modulation of visual perception by basal forebrain cholinergic neurons. *Nat. Neurosci.* 16, 1857–1863. doi:10.1038/nn.3552.

Platholi, J. and Hemmings Jr, H. C. (2021). Effects of general anesthetics on synaptic transmission and plasticity. *Curr. Neuropharmacol.* 19. doi:10.2174/1570159X19666210803105232.

Polack, P.-O. and Contreras, D. (2012). Long-Range Parallel Processing and Local Recurrent Activity in the Visual Cortex of the Mouse. *J. Neurosci.* 32, 11120–11131. doi:10.1523/JNEUROSCI.6304-11.2012.

Polack, P.-O. O., Friedman, J., and Golshani, P. (2013). Cellular mechanisms of brain state-dependent gain modulation in visual cortex. *Nat. Neurosci.* 16, 1331–1339.

doi:10.1038/nn.3464.Cellular.

Posner, M. I., Snyder, C. R. R., and Davidson, B. J. (2018). Attention and the detection of signals. *Hum. Percept. Institutional Perform. Reform Aust.* 109, 43–57. doi:10.4324/9781351156288-10.

Prasad, J. A., Carroll, B. J., and Sherman, S. M. (2020). Layer 5 Corticofugal Projections from diverse cortical areas: Variations on a pattern of thalamic and extrathalamic targets. *J. Neurosci.* 40, 5785–5796. doi:10.1523/JNEUROSCI.0529-20.2020.

Purdon, P. L., Pierce, E. T., Mukamel, E. A., Prerau, M. J., Walsh, J. L., Foon, K., Wong, K., Salazar-gomez, A. F., Harrell, P. G., Sampson, A. L., Cimenser, A., and Ching, S. (2013). Electroencephalogram signatures of loss and recovery of consciousness from propofol. doi:10.1073/pnas.1221180110.

Purves, D., Augustine, G. J., Fitzpatrick, D., Hall, W., Anthony-Samuel, L., NcNamara, J. O., and Williams, S. M. (2004). *Neuroscience.* 3rd ed. , eds. D. Purves, G. J. Augustine, D. Fitzpatrick, W. Hall, L. Anthony-Samuel, J. O. NcNamara, et al. Sunderland, Massachusetts U.S.A. doi:10.1016/B978-0-12-801238-3.62132-3.

Ranft, A., Kurz, J., Deuringer, M., Haseneder, R., Dodt, H. U., Zieglgänsberger, W., Kochs, E., Eder, M., and Hapfelmeier, G. (2004). Isoflurane modulates glutamatergic and GABAergic neurotransmission in the amygdala. *Eur. J. Neurosci.* doi:10.1111/j.1460-9568.2004.03603.x.

Raz, A., Grady, S. M., Krause, B. M., Uhlrich, D. J., Manning, K. A., and Banks, M. (2014). Preferential effect of isoflurane on top-down vs . bottom-up pathways in sensory cortex. *Front. Syst. Neurosci.* 8, 1–22. doi:10.3389/fnsys.2014.00191.

Reference Atlas :: Allen Brain Atlas: Mouse Brain Available at: https://mouse.brain-map.org/static/atlas [Accessed July 31, 2021].

Reinhold, K., Lien, A. D., and Scanziani, M. (2015a). Distinct recurrent versus afferent dynamics in cortical visual processing. *Nat. Neurosci.* 18, 1789–1797. doi:10.1038/nn.4153.

Reinhold, K., Lien, A. D., and Scanziani, M. (2015b). Distinct recurrent versus afferent dynamics in cortical visual processing. *Nat. Neurosci.* 18, 1789–1797. doi:10.1038/nn.4153.

Reinhold, K., Lien, A. D., and Scanziani, M. (2015c). Supplement Distinct recurrent versus afferent dynamics in cortical visual processing. *Nat. Neurosci.* 18, 1789–1797. doi:10.1038/nn.4153.

Robinson, D. H. and Toledo, A. H. (2012). Historical Development of Modern Anesthesia. *J. Investig. Surg.* 25, 141–149. doi:10.3109/08941939.2012.690328.

Rosanova, M., Gosseries, O., Casarotto, S., Boly, M., Casali, A. G., Bruno, M. A., Mariotti, M., Boveroux, P., Tononi, G., Laureys, S., and Massimini, M. (2012). Recovery of cortical effective connectivity and recovery of consciousness in vegetative patients. *Brain* 135, 1308–1320. doi:10.1093/brain/awr340.

Russell, I. F. (1989). Conscious awareness during general anaesthesia: relevance of autonomic signs and isolated arm movements as guides to depth of anaesthesia. *Baillieres. Clin. Anaesthesiol.* 3, 511–532. doi:10.1016/S0950-3501(89)80016-9.

Saleem, A. B., Lien, A. D., Krumin, M., Haider, B., Rosón, M. R., Ayaz, A., Reinhold, K., Busse,

L., Carandini, M., Harris, K. D., and Carandini, M. (2017). Subcortical Source and Modulation of the Narrowband Gamma Oscillation in Mouse Visual Cortex. *Neuron* 93, 315–322. doi:10.1016/j.neuron.2016.12.028.

Sanders, R. (2016). Incidence of Connected Consciousness after Tracheal Intubation. *Anesthesiology*. doi:10.1097/ALN.0000000000001479.

Sanders, R. D., Tononi, G., Laureys, S., and Sleigh, J. W. (2012). Unresponsiveness ≠ Unconsciousness. *Anesthesiology* 116, 946–959. doi:10.1097/ALN.0b013e318249d0a7.

Sato, T. K., Nauhaus, I., and Carandini, M. (2012). Traveling Waves in Visual Cortex. *Neuron* 75, 218–229. doi:10.1016/j.neuron.2012.06.029.

Scharf, M. T. and Kelz, M. B. (2013). Sleep and Anesthesia Interactions: A Pharmacological Appraisal. *Curr. Anesthesiol. Rep.* 3, 1–9. doi:10.1007/s40140-012-0007-0.

Schneider Gerhard, M. D., Hollweck Regina, M. S., Ningler Michael, M. S., Stockmanns Gudrun, P. D., and Kochs Eberhard F., M. D. (2005). Detection of Consciousness by Electroencephalogram and Auditory Evoked Potentials. *Anesthesiology* 103, 934–943. Available at: http://dx.doi.org/.

Sellers, K. K., Bennett, D. V., Hutt, A., Williams, J. H., and Fröhlich, F. (2015). Awake vs. anesthetized: layer-specific sensory processing in visual cortex and functional connectivity between cortical areas. *J. Neurophysiol.* 113, 3798–3815. doi:10.1152/jn.00923.2014.

Sellers, K. K., Bennett, D. V, Hutt, A., and Fröhlich, F. (2013). Anesthesia differentially modulates spontaneous network dynamics by cortical area and layer. *J. Neurophysiol.* 110, 2739–51. doi:10.1152/jn.00404.2013.

Senzai, Y., Fernandez-Ruiz, A., and Buzsáki, G. (2019). Layer-Specific Physiological Features and Interlaminar Interactions in the Primary Visual Cortex of the Mouse. *Neuron* 101, 500-513.e5. doi:10.1016/j.neuron.2018.12.009.

Shortal, B. P., Reitz, S. L., Aggarwal, A., Meng, Q. C., McKinstry-Wu, A. R., Kelz, M. B., and Proekt, A. (2018). Development and validation of brain target controlled infusion of propofol in mice. *PLoS One* 13, 1–14. doi:10.1371/journal.pone.0194949.

Shushruth, S. (2013). Exploring the Neural Basis of Consciousness through Anesthesia. *J. Neurosci.* 33, 1757–1758. doi:10.1523/JNEUROSCI.5215-12.2013.

Sohal, V. S. (2016). How Close Are We to Understanding What (if Anything) γ Oscillations Do in Cortical Circuits? *J. Neurosci.* 36, 10489–10495. doi:10.1523/JNEUROSCI.0990-16.2016.

Sohal, V. S., Zhang, F., Yizhar, O., and Deisseroth, K. (2009). Parvalbumin neurons and gamma rhythms enhance cortical circuit performance. *Nature* 459, 698–702. doi:10.1038/nature07991.

Solovey, G., Alonso, L. M., Yanagawa, T., Fujii, N., Magnasco, M. O., Cecchi, G. A., and Proekt, A. (2015). Loss of Consciousness Is Associated with Stabilization of Cortical Activity. *J. Neurosci.* 35, 10866–10877. doi:10.1523/JNEUROSCI.4895-14.2015.

Sonner, J. M., Werner, D. F., Elsen, F. P., Xing, Y., Liao, M., Harris, R. A., Harrison, N. L., Fanselow, M. S., Eger, E. I., and Homanics, G. E. (2007). Effect of isoflurane and other potent inhaled anesthetics on minimum alveolar concentration, learning, and the righting reflex in mice engineered to express α1 γ-aminobutyric acid type A receptors unresponsive

to isoflurane. *Anesthesiology* 106, 107–113. doi:10.1097/00000542-200701000-00019.

Speed, A., Del Rosario, J., Burgess, C. P., and Haider, B. (2019). Cortical State Fluctuations across Layers of V1 during Visual Spatial Perception. *Cell Rep.* 26, 2868-2874.e3. doi:10.1016/j.celrep.2019.02.045.

Stein, B. E. and Stanford, T. R. (2008). Multisensory integration: current issues from the perspective of the single neuron. *Nat. Rev. Neurosci.* 9, 255–66. doi:10.1038/nrn2331.

Steriade, M. and Timofeev, I. (2003). Review Neuronal Plasticity in Thalamocortical Networks during Sleep and Waking Oscillations present in the background electrical activity during the brain-activated states of waking and REM sleep, are also thought to enhance temporal coherence of re. *Neuron* 37, 563–576. doi:10.1016/S0896-6273(03)00065-5.

Stevenson, R. A., Ghose, D., Fister, J. K., Sarko, D. K., Altieri, N. A., Nidiffer, A. R., Kurela, L. A. R., Siemann, J. K., James, T. W., and Wallace, M. T. (2014). Identifying and Quantifying Multisensory Integration: A Tutorial Review. *Brain Topogr.* 27, 707–730. doi:10.1007/s10548-014-0365-7.

Storchi, R., Bedford, R. A., Martial, F. P., Allen, A. E., Wynne, J., Montemurro, M. A., Petersen, R. S., and Lucas, R. J. (2017). Modulation of Fast Narrowband Oscillations in the Mouse Retina and dLGN According to Background Light Intensity. *Neuron* 93, 299–307. doi:10.1016/j.neuron.2016.12.027.

Tagliazucchi, E. and Laufs, H. (2014). Decoding Wakefulness Levels from Typical fMRI Resting-State Data Reveals Reliable Drifts between Wakefulness and Sleep. *Neuron* 82, 695–708. doi:10.1016/j.neuron.2014.03.020.

Tang, P. and Eckenhoff, R. (2018). Recent progress on the molecular pharmacology of propofol. *F1000Research* 7, 123. doi:10.12688/f1000research.12502.1.

The Thalamus (1985). *The Thalamus*. doi:10.1007/978-1-4615-1749-8.

Thengone, D., Gagnidze, K., Pfaff, D., and Proekt, A. (2016). Phase-amplitude coupling in spontaneous mouse behavior. *PLoS One* 11, e0162262. doi:10.1371/journal.pone.0162262.

Tiesinga, P., Whitmer, D., Sejnowski, T. J., Fellous, J. M., and Schreiber, S. (2003). A new correlation-based measure of spike timing reliability. *Neurocomputing* 52–54, 925–931. doi:10.1016/s0925-2312(02)00838-x.

Torrence, C. and Compo, G. P. (1998). A Practical Guide to Wavelet Analysis. *Bull. Am. Meteorol. Soc.* 79, 61–78. doi:10.1175/1520-0477(1998)079<0061:APGTWA>2.0.CO;2.

Tort, A. B. L. L., Komorowski, R., Eichenbaum, H., and Kopell, N. (2010). Measuring phase-amplitude coupling between neuronal oscillations of different frequencies. *J. Neurophysiol.* 104, 1195–1210. doi:10.1152/jn.00106.2010.

Townsend, R. G., Solomon, S. S., Chen, S. C., Pietersen, A. N. J., Martin, P. R., Solomon, S. G., and Gong, P. (2015a). Emergence of complex wave patterns in primate cerebral cortex. *J. Neurosci.* 35, 4662–4667. doi:10.1523/JNEUROSCI.4509-14.2015.

Townsend, R. G., Solomon, S. S. G., Chen, S. C., Pietersen, A. N. J., Martin, P. R., Solomon, S. S. G., and Gong, P. (2015b). Emergence of complex wave patterns in primate cerebral cortex. *J. Neurosci.* 35, 4662–4667. doi:10.1523/JNEUROSCI.4509-14.2015.

Townsend, X. R. G., Solomon, X. S. G. S. S., Martin, X. P. R., Solomon, X. S. G. S. S., and Gong, X. P. (2017a). Visual Motion Discrimination by Propagating Patterns in Primate Cerebral Cortex. 37, 10074–10084. doi:10.1523/JNEUROSCI.1538-17.2017.

Townsend, X. R. G., Solomon, X. S. S., Martin, X. P. R., Solomon, X. S. G., and Gong, X. P. (2017b). Visual Motion Discrimination by Propagating Patterns in Primate Cerebral Cortex. 37, 10074–10084. doi:10.1523/JNEUROSCI.1538-17.2017.

Traub, R. D., Contreras, D., Cunningham, M. O., Murray, H., Fiona, E. N., Roopun, A., Bibbig, A., Wilent, W. B., Higley, M. J., Whittington, A., Traub, R. D., Contreras, D., Cunningham, M. O., Murray, H., Lebeau, F. E. N., Roopun, A., Bibbig, A., Wilent, W. B., Higley, M. J., et al. (2016a). Single-Column Thalamocortical Network Model Exhibiting Gamma Oscillations , Sleep Spindles , and Epileptogenic Bursts Single-Column Thalamocortical Network Model Exhibiting Gamma Oscillations , Sleep Spindles , and Epileptogenic Bursts. 2194–2232. doi:10.1152/jn.00983.2004.

Traub, R. D., Contreras, D., Cunningham, M. O., Murray, H., Fiona, E. N., Roopun, A., Bibbig, A., Wilent, W. B., Higley, M. J., Whittington, A., Traub, R. D., Contreras, D., Cunningham, M. O., Murray, H., Lebeau, F. E. N., Roopun, A., Bibbig, A., Wilent, W. B., Higley, M. J., et al. (2016b). Single-Column Thalamocortical Network Model Exhibiting Gamma Oscillations , Sleep Spindles , and Epileptogenic Bursts Single-Column Thalamocortical Network Model Exhibiting Gamma Oscillations , Sleep Spindles , and Epileptogenic Bursts. 2194–2232. doi:10.1152/jn.00983.2004.

Traub, R. D., Whittington, M. A., Stanford, I. M., and Jefferys, J. G. R. (1996). A mechanism for generation of long-range synchronous fast oscillations in the cortex. *Nature* 383, 621–224. doi:10.1038/383621a0.

Ursino, M., Cuppini, C., and Magosso, E. (2014). Neurocomputational approaches to modelling multisensory integration in the brain: A review. *Neural Networks* 60, 141–165. doi:10.1016/j.neunet.2014.08.003.

Vaknin, G., DiScenna, P. G., and Teyler, T. J. (1988). A method for calculating current source density (CSD) analysis without resorting to recording sites outside the sampling volume. *J. Neurosci. Methods* 24, 131–135. doi:10.1016/0165-0270(88)90056-8.

van Ede, F., van Pelt, S., Fries, P., and Maris, E. (2015). Both ongoing alpha and visually induced gamma oscillations show reliable diversity in their across-site phase-relations. *J. Neurophysiol.* 113, 1556–1563. doi:10.1152/jn.00788.2014.

Van Kerkoerle, T., Self, M. W., Dagnino, B., Gariel-Mathis, M. A., Poort, J., Van Der Togt, C., and Roelfsema, P. R. (2014). Alpha and gamma oscillations characterize feedback and feedforward processing in monkey visual cortex. *Proc. Natl. Acad. Sci. U. S. A.* 111, 14332–14341. doi:10.1073/pnas.1402773111.

Vazey, E. M. and Aston-Jones, G. (2014). Designer receptor manipulations reveal a role of the locus coeruleus noradrenergic system in isoflurane general anesthesia. *Proc. Natl. Acad. Sci.* 111, 3859–3864. doi:10.1073/PNAS.1310025111.

Vecchia, D., Beltramo, R., Vallone, F., Chéreau, R., Forli, A., Molano-Mazón, M., Bawa, T., Binini, N., Moretti, C., Holtmaat, A., Panzeri, S., and Fellin, T. (2020). Temporal Sharpening of Sensory Responses by Layer V in the Mouse Primary Somatosensory Cortex. *Curr. Biol.* 30, 1589-1599.e10. doi:10.1016/j.cub.2020.02.004.

Vesuna, S., Kauvar, I. V., Richman, E., Gore, F., Oskotsky, T., Sava-Segal, C., Luo, L., Malenka,

R. C., Henderson, J. M., Nuyujukian, P., Parvizi, J., and Deisseroth, K. (2020). Deep posteromedial cortical rhythm in dissociation. *Nature* 586, 87–94. doi:10.1038/s41586-020-2731-9.

Vinck, M., Batista-Brito, R., Knoblich, U., and Cardin, J. A. (2015). Arousal and Locomotion Make Distinct Contributions to Cortical Activity Patterns and Visual Encoding. *Neuron* 86, 740–754. doi:10.1016/j.neuron.2015.03.028.

Vinck, M., Lima, B., Womelsdorf, T., Oostenveld, R., Singer, W., Neuenschwander, S., and Fries, P. (2010). Gamma-phase shifting in awake monkey visual cortex. *J. Neurosci.* 30, 1250–1257. doi:10.1523/JNEUROSCI.1623-09.2010.

Wang and Buzsáki, G. (1996). Gamma oscillation by synaptic inhibition in a hippocampal interneuronal network model. *J. Neurosci.* 16, 6402–6413. doi:citeulike-article-id:134404.

Wang, Q., Gao, E., and Burkhalter, A. (2011). Gateways of ventral and dorsal streams in mouse visual cortex. *J. Neurosci.* 31, 1905–1918. doi:10.1523/JNEUROSCI.3488-10.2011.

Wang, X. (2009). Propofol and isoflurane enhancement of tonic gamma-aminobutyric acid type a current in cardiac vagal neurons in the nucleus ambiguus. *Anesth. Analg.* 108, 142–148. doi:10.1213/ane.0b013e31818d8b79.

Waxman, S. G. and Bennett, M. V. L. (1972). Relative Conduction Velocitiees of Small Mylinated and Non-myelinated Fibres in the Central Nervous system. *Nat. new Biol.* 238, 217–219.

Weiser, B. P., Hall, M. A., Weinbren, N. L., Woll, K. A., Dailey, W. P., Eckenhoff, M. F., and Eckenhoff, R. G. (2015). Macroscopic and macromolecular specificity of alkylphenol anesthetics for neuronal substrates. *Sci. Rep.* 5, 1–6. doi:10.1038/srep09695.

Welle, C. G. and Contreras, D. (2015). Sensory-driven and spontaneous gamma oscillations engage distinct cortical circuitry. *J. Neurophysiol.* 115, jn.00137.2015. doi:10.1152/jn.00137.2015.

Wester, J. C. and Contreras, D. (2012). Columnar interactions determine horizontal propagation of recurrent network activity in neocortex. *J. Neurosci.* 32, 5454–71. doi:10.1523/JNEUROSCI.5006-11.2012.

White, N. S. and Alkire, M. T. (2003). Impaired thalamocortical connectivity in humans during general-anesthetic-induced unconsciousness. *Neuroimage* 19, 402–411. doi:10.1016/S1053-8119(03)00103-4.

Whittington, M. A., Traub, R. D., Kopell, N., Ermentrout, B., and Buhl, E. H. (2000). Inhibition-based rhythms: Experimental and mathematical observations on network dynamics. *Int. J. Psychophysiol.* 38, 315–336. doi:10.1016/S0167-8760(00)00173-2.

Wilson, H. R. and Cowan, J. D. (1972). Excitatory and Inhibitory Interactions in Localized Populations of Model Neurons. *Biophys. J.* 12, 1–24. doi:10.1016/S0006-3495(72)86068-5.

Womelsdorf, T., Fries, P., Mitra, P. P., and Desimone, R. (2006). Gamma-band synchronization in visual cortex predicts speed of change detection. *Nature* 439, 733–736. doi:10.1038/nature04258.

Womelsdorf, T., Lima, B., Vinck, M., Oostenveld, R., Singer, W., Neuenschwander, S., and Fries, P. (2012). Orientation selectivity and noise correlation in awake monkey area V1 are modulated by the gamma cycle. *Proc. Natl. Acad. Sci.* 109, 4302–4307.

doi:10.1073/pnas.1114223109.

Wu, J., Huang, X., and Zhang, C. (2008). Propagating waves of activity in the neocortex: what they are, what they do. *Neuroscientist* 14, 487–502. doi:10.1177/1073858408317066.

Wysocki, G. and Stiles, W. (1982). *Color Science: Concepts and Methods, Quantitiative Data and Formulea*. Hoboken, United States: John Wiley and Sons.

Xu, W., Huang, X., Takagaki, K., and Wu, J. young (2007a). Compression and reflection of visually evoked cortical waves. *Neuron* 55, 119–129. doi:10.1016/j.neuron.2007.06.016.

Xu, W., Huang, X., Takagaki, K., and Wu, J. young (2007b). Compression and Reflection of Visually Evoked Cortical Waves. *Neuron* 55, 119–129. doi:10.1016/j.neuron.2007.06.016.

Yamamura, T., Harada, K., Okamura, A., and Kemmotsu, O. (1990). Is the Site of Action of Ketamine Anesthesia the N-Methyl-D-Aspartate Receptor? *Anesthesiology* 72, 704–710. doi:10.1097/00000542-199004000-00021.

Yanagisawa, M., Sun, Y., Kelz, M. B., Thornton, M., Moore, J. T., Chen, J., Veasey, S. C., Funato, H., Dixon, S., and Cheng Meng, Q. (2008). An essential role for orexins in emergence from general anesthesia. *Proc. Natl. Acad. Sci.* 105, 1309–1314. doi:10.1073/pnas.0707146105.

Yip, G. M. S., Chen, Z. W., Edge, C. J., Smith, E. H., Dickinson, R., Hohenester, E., Townsend, R. R., Fuchs, K., Sieghart, W., Evers, A. S., and Franks, N. P. (2013). A propofol binding site on mammalian GABA A receptors identified by photolabeling. *Nat. Chem. Biol.* 9, 715–720. doi:10.1038/nchembio.1340.

Zanos, T. P., Mineault, P. J., Nasiotis, K. T., Guitton, D., and Pack, C. C. (2015). A Sensorimotor Role for Traveling Waves in Primate Visual Cortex. *Neuron* 85, 615–627. doi:10.1016/j.neuron.2014.12.043.

Zhou, C., Douglas, J. E., Kumar, N. N., Ph, D., Shu, S., Bayliss, D. A., Ph, D., Chen, X., and Ph, D. (2018). Forebrain HCN1 Channels Contribute to Hypnotic Actions of Ketamine. 785–795.

Zingg, B., Hintiryan, H., Gou, L., Song, M. Y., Bay, M., Bienkowski, M. S., Foster, N. N., Yamashita, S., Bowman, I., Toga, A. W., and Dong, H. W. (2014). Neural networks of the mouse neocortex. *Cell* 156, 1096–1111. doi:10.1016/j.cell.2014.02.023.